VT-Forschungsbericht 2020-03

Numerical Simulation of Autoignition under Gas Turbine Operating Conditions

Dipl.-Ing. Juliane Prause

Deutsches Zentrum für Luft- und Raumfahrt
Institut für Verbrennungstechnik
Stuttgart

DLR Deutsches Zentrum für Luft- und Raumfahrt

Herausgeber

Deutsches Zentrum
für Luft- und Raumfahrt

Institut für
Verbrennungstechnik

Pfaffenwaldring 38-40
70569 Stuttgart

Telefon
Telefax

(0 7 11) 68 62 - 3 08
(0 7 11) 68 62 - 5 78

D93, Stuttgart

Numerical Simulation of Autoignition under Gas Turbine Operating Conditions

A thesis accepted by the Faculty of Aerospace Engineering and Geodesy of the University of Stuttgart in partial fulfillment of the requirements for the degree of Doctor of Engineering Sciences (Dr.-Ing.)

by

Dipl.-Ing. Juliane Prause

born in Berlin

Main referee:	Prof. Dr.-Ing. Manfred Aigner
Co-referee:	Prof. Dr.-Ing. Hans-Jörg Bauer
Date of defence:	23/04/2019

Institute of Combustion Technology for Aerospace Engineering
University of Stuttgart

2020

Vorwort

Die vorliegende Promotion entstand während meiner Tätigkeit als wissenschaftliche Mitarbeiterin am DLR-Institut für Verbrennungstechnik. An dieser Stelle möchte ich mich bei all denen bedanken, die mich auf diesem Weg begleitet haben.
Allen voran danke ich meinem Doktorvater Prof. Dr. Manfred Aigner für das spannende Dissertationsthema, die Betreuung der Arbeit sowie für die besonderen Entwicklungsmöglichkeiten im Rahmen der Begleitforschung zur Energiewende im Verkehr. Prof. Dr. Hans-Jörg Bauer vom Institut für Thermische Strömungsmaschinen des KIT danke ich für die Übernahme des Mitberichts, die gründliche Prüfung der Arbeit, aber auch für die interessanten Vorlesungen im Rahmen meines Studiums in Karlsruhe, durch die ich meine Leidenschaft für Gasturbinen und für die Verbrennungstechnik entdeckt habe. Prof. Dr. Stephan Staudacher danke ich für die Übernahme des Prüfungsvorsitzes. Diese Arbeit enstand im Rahmen einer DLR/Alstom-Forschungspatenschaft. Der Alstom AG (jetzt General Electric GmbH) und insbesondere Dr. Khawar Syed danke ich für die fachliche und finanzielle Unterstützung.
Ganz besonderer Dank gilt meinem Betreuer und Abteilungsleiter der Simulation Dr. Berthold Noll. Mit seinem umfangreichen Wissen und seiner Erfahrung hat er diese Arbeit maßgebglich mitgeprägt. Zudem bin ich ihm auch sehr dankbar für den gewährten wissenschaftlichen Freiraum, der es mir ermöglicht hat eigene Schwerpunkte in der Arbeit zu setzen. Auch meinen Kollegen vom Institut möchte ich sehr herzlich für die tolle Zusammenarbeit danken: Dr. Julia Fleck, Dr. Christoph Arndt, Dr. Bastian Rauch, Dr. Michael Severin, Dr. Thorsten Methling und vielen weiteren, die ich leider nicht alle namentlich hier aufzählen kann. Der intensive fachliche Austausch - insbesondere über die verschiedenen Abteilungen hinweg - hat entscheidend zum Erfolg, aber auch zur Freude an der Arbeit beigetragen.
Schließlich möchte ich mich noch bei meiner gesamten Familie für Ihre Unterstützung bedanken. Liebe Eltern, durch euch habe ich gelernt, an meine Träume zu glauben und für diese zu kämpfen. Mein lieber Birger, dir danke ich von ganzem Herzen für deine Liebe und Aufmerksamkeit sowie für deine Gelduld und Unterstützung bei der Promotion. Und schlussendlich danke ich meinen Kindern, die mir mit Ihrer unermesslichen Lebensfreude so viel Glück ins Leben bringen.

Juliane Prause im Dezember 2019

Contents

List of Symbols

Latin symbols

A	Pre-exponential constant	$(\mathrm{l/mol})^{\mathrm{n\text{-}1}}/\mathrm{s}$
$\tilde{a}$	Strain rate	$1/\mathrm{s}$
c	Number concentration	-
c_p	Specific heat capacity for constant pressure	$\mathrm{J/K}$
D	Diffusivity	$\mathrm{m^2/s}$
D	Diameter	m
Da	Damköhler number	-
E_a	Activation energy	$\mathrm{J/mol}$
f	Frequency	$1/\mathrm{s}$
h	Specific enthalpy	$\mathrm{J/kg}$
J	Jet-to-crossflow momentum flux ratio	-
j	Mass diffusion flux	$\mathrm{kg/(m^2\,s)}$
k	Reaction rate	$1/\mathrm{s}$
k	Rate coefficients for chemical reactions	$\mathrm{m^3/(mol\,s)}$
k	Turbulent kinetic energy	$\mathrm{m^2/s^2}$
M	Molar mass	$\mathrm{kg/mol}$
Ma	Mach number	-
$\dot{m}$	Mass flow rate	$\mathrm{kg/s}$
n	Number of free valences	-
p	Pressure	Pa
Pr	Prandtl number	-
q	Specific enthalpy flux	$\mathrm{J/(m^2\,s)}$

R	Universal gas constant	$\mathrm{J/(mol\,K)}$
R	Jet-to-crossflow velocity ratio	-
Re	Reynolds number	-
St	Strouhal number	-
Sc	Schmidt number	-
T	Temperature	K
t	Time	s
u, v, w	Velocity	m/s
u_τ	Friction velocity	m/s
X	Mole fraction	-
x	Coordinate in streamwise direction, Length	m
x_i	Coordinate in direction i	m
x^+	Dimensionless wall units	-
Y	Mass fraction	-
y	Coordinate in wall-normal direction	m
Z	Mixture fraction	-
z	Coordinate in spanwise direction	m

Greek symbols

α	Species	-
β	Temperature exponent	-
Θ	Dimensionless temperature	-
λ	Eigenvalue of the chemical source term	1/s
λ	Thermal conductivity	$\mathrm{W/(m\,K)}$
μ	Dynamic viscosity	$\mathrm{kg/(m\,s)}$
ν	Kinematic viscosity	$\mathrm{m^2/s}$
ν	Stoichiometric coefficient	-
ρ	Density	$\mathrm{kg/m^3}$
τ_{ij}	Viscous stress tensor	$\mathrm{N/m^2}$
τ_w	Wall shear stress	Pa

χ	Scalar dissipation rate	1/s
ω	Chemical source term	$\mathrm{kg/(m^3\,s)}$

Subscripts

avg	Averaged
rms	Root-mean-squared
c	Chemical scale
cf	Crossflow
co	Crossover
exp	Explosive
HG	Hot gas generator
hg	Hot gas
ign	Ignition
jet	Jet flow
mix	Mixture
mr	Most reactive
MS	Mixing section
res	Residence
res	Resolved
r	Reaction
sgs	Subgrid scale
st	Stoichiometric
tot	Total
t	Turbulent scale

Abbreviations

APDF	Assumed Probability Density Function
CFD	Computational Fluid Dynamics
CFL	Courant-Friedrich-Lewy
CMC	Conditional Moment Closure
DNS	Direct Numerical Simulation

EDC	Eddy Dissipation Concept
FLOX™	FLameless OXidiation (Combustion Systems)
FRC	Finite Rate Chemistry
LES	Large-Eddy Simulation
MILD	Moderate or Intense Low oxygen Dilution (Combustion System)
PDF	Probability Density Function
PIV	Particle Image Velocimetry
RANS	Reynolds-Averaged Navier-Stokes
SAS	Scale-Adaptive Simulation
URANS	Unsteady Reynolds-Averaged Navier-Stokes

Operators

$[\cdot]$	Concentration
Δ	Difference
∂	Partial differential

Kurzfassung

Die vorliegende Arbeit hat das Ziel die Leistungsfähigkeit der numerischen Modellierung von Selbstzündvorgängen bei realitätsnahen Gasturbinenbedingungen zu bestimmen und mögliche Optimierungspotentiale für die Simulation zu identifizieren. Im Fokus steht die Verbrennung von wasserstoffhaltigem Brennstoff in der zweiten Brennkammerstufe einer Gasturbine mit sequentieller Verbrennung. In diesem System ist die zuverlässige Vorhersage von Selbstzündung von zentraler Bedeutung, um eine hohe Betriebssicherheit zu gewährleisten und die Schadstoffemissionen gering zu halten. Die Auslegung neuer und optimierter Brennkammersysteme kann mit Hilfe numerischer Berechnungsverfahren erfolgen. Um die Simulationsvorhersagen zu bewerten und eine zielführende Entwicklungsstrategie für die Brennkammerauslegung abzuleiten, ist es notwendig die Qualität der Simulationsergebnisse abschätzen zu können. Die Simulationsqualität kann anhand von Validierungsstudien ermittelt werden, in denen die Simulationsergebnisse mit geeigneten experimentellen Referenzdaten verglichen werden. In den letzten 15 Jahren wurden zahlreiche Studien zur Validierung von Selbstzündsimulationen veröffentlicht. Die meisten dieser Studien wurden an einer generischen Freistrahlströmung bei atmosphärischem Druck durchgeführt. Für Selbstzündsimulationen unter Gasturbinen-typischen Bedingungen wie erhöhten Drücken und komplexen Strömungsgeometrien liegen bislang jedoch keine detaillierten Validierungen vor.

Um diese Forschungslücke zu schließen, wird in dieser Arbeit die Zuverlässigkeit moderner Simulationsverfahren unter realitätsnahen Gasturbinenbedingungen analysiert. Darüber hinaus wird untersucht, inwiefern die unter vereinfachten Laborbedingungen (atmosphärischer Druck, geringe Turbulenz und einfache Strömungsgeometrie) erzielten Ergebnissen zuverlässig auf reale Betriebsbedingungen übertragen werden können. Die Validierung konzentriert sich auf die Brennstoff-Vormischung in zweistufigen Gasturbinen mit Zwischenerhitzung bei einem Druck von 15 bar. Der Brennstoff wird quer zum heißen Oxidatorstrom bei Temperaturen von über 1000 K und Reynolds-Zahlen von bis zu 10^6 eingedüst. Bei diesen Bedingungen werden sehr hohe Anforderungen an die Simulation und Messtechnik gestellt. Zudem erschwert die enge Kopplung verschiedener Teilmodelle für die Turbulenz, Chemie und Turbulenz-Chemie-Interaktion die Identifizierung spezifischer Modelldefizite. Aus diesem Grund wird in der vorliegenden Arbeit die Methodik der Validierungshierarchie nach Ober-

kampf angewandt. In Ergänzung zum anwendungsnahen Hochdruck-Brennkammerexperiment wurden ausgewählte Subsysteme definiert und validiert, um gezielte Informationen zu spezifischen Teilmodellen zu erhalten.
Der Vergleich der numerischen Simulation mit dem Hochdruckexperiment zeigt, dass die auftretenden Verbrennungsphänomene, wie die Entstehung der Zündkerne, Flammenausbreitung und Flammenstabilisierung sehr gut wiedergegeben werden können. Im quantitativen Vergleich treten jedoch signifikante Unterschiede auf, die vor allem auf den hohen Umgebungsdruck und die komplexe Strömungsgeometrie zurückzuführen sind. Es hat sich gezeigt, dass die unter Laborbedingungen erzielte Genauigkeit nicht direkt auf reale Betriebsbedingungen übertragen werden kann. Obwohl die Zündung von Wasserstoff bei niedrigem Druck sehr gut bestimmt werden kann, sind die Unsicherheiten bei Gasturbinen-relevantem Druck verhältnismäßig hoch. Eine weitere Herausforderung ergibt sich aus der anwendungsnahen Strömungskonfiguration. Im Gegensatz zur Freistrahlströmung tritt in der hier untersuchten Querstrahleinströmung ein Rückströmgebiet auf. Einzelne Flammenkerne, die in der Nähe dieser Rezirkulationszone entstehen, können sich dort stabilisieren und in Form einer stationären Flamme verankern. Um dieses sicherheitsrelevante Phänomen korrekt zu modellieren, muss die gesamte räumliche Verteilung potenzieller Zündkerne exakt wiedergegeben werden. In dieser Arbeit wurden zwei verschiedene Ursachen für die Zündkernvariation identifiziert: Einerseits haben Temperaturfluktuationen im heißen Oxidatorstrom einen direkten Einfluss auf die Zündverzugzeit. Da die Selbstzündung sehr Temperatur-sensitiv ist, bewirken selbst kleine Temperaturschwankungen eine große Streuung der Zündorte. Andererseits hat auch die Turbulenz einen großen Einfluss auf die Zündkernvariation, welche vor allem durch großskalige turbulente Strukturen verursacht wird.
Erstmals wurden numerische Simulationen von Selbstzündungsvorgängen unter anwendungsnahen Gasturbinen-spezifischen Bedingungen mit geeigneten experimentellen Referenzdaten validiert. Es hat sich gezeigt, dass die Ergebnisse aus vereinfachten Selbstzündexperimenten bei atmospherischen Druck nicht direkt auf reale technische Betriebsbedingungen übertragbar sind, da die Anforderungen an die Modellierung sehr unterschiedlich sind. Unter Anwendung einer systemspezifischen Validierungshierarchie war es zudem möglich, die Ursache der Modellierungsunsicherheiten zu identifizieren und im Detail zu untersuchen. Aufbauend auf den gewonnenen Erkenntnissen wird im Ergebnis ein Leitfaden für die Simulation von Selbstzündvorgängen zur Auslegung neuer Brennkammerkonzepte bereitgestellt.

Summary

This work aims to determine the performance of the numerical modelling of autoignition processes under realistic gas turbine operating conditions and to identify promising optimization potential for the simulation. The focus is on the combustion of hydrogen-containing fuel in the second combustion chamber of a sequential gas turbine. In this system, the reliable prediction of autoignition is of central importance to ensure a high level of operational safety and to keep pollutant emissions low. New and optimized combustion chamber systems can be designed using numerical simulation methods. In order to evaluate the numerical predictions and derive a target-oriented development strategy for the combustion chamber design, it is necessary to assess the quality of the simulation results. The quality can be determined by means of validation studies in which simulation results are compared with suitable experimental reference data. Over the last 15 years, many studies on the validation of autoignition simulations have been published. The majority of these studies were performed on a generic free jet flow at atmospheric pressure. Until now, however, no detailed validations have been available for autoignition simulations under gas turbine typical conditions such as increased pressure and complex flow geometry.

In order to close this gap in research, the reliability of modern simulation methods under realistic gas turbine conditions is analyzed in this work. In addition, to what extent the results, which were obtained under simplified laboratory conditions (atmospheric pressure, low turbulence and simple flow geometry), can be reliably transferred to real operating conditions is investigated. The validation study focuses on the fuel premix section of staged gas turbines at a pressure of 15 bar. The fuel is injected transversely into the hot oxidizer at temperatures of more than 1000 K and Reynolds numbers of up to 10^6. Under these conditions the demands on simulation and measurement technology are very high. Furthermore, the close coupling of different submodels for turbulence, chemistry and turbulence-chemistry interaction makes it difficult to identify specific model deficits. For this reason, the methodology of the validation hierarchy according to Oberkampf is applied in this work. In addition to the application-oriented high-pressure experiment, selected subsystems were defined and validated in order to obtain information on specific submodels.

The comparison of the numerical simulation with the high-pressure experiments shows that

the combustion phenomena, such as the formation of the ignition kernels, flame propagation and flame stabilization, can be reproduced very well. In the quantitative comparison, however, significant differences occur, which are mainly due to the high pressure and the complex flow geometry. It has been shown that the accuracy and modeling quality achieved under laboratory conditions cannot be directly transferred to real operating conditions. Although the ignition of hydrogen at low pressure can be determined very well, the uncertainties at gas-turbine-relevant pressure are relatively high. A further challenge results from the application-oriented flow configuration. In contrast to the free jet flow, a backflow occurs in the jet-in-crossflow configuration investigated here. Individual ignition kernels that form near this recirculation zone can stabilize there and anchor in the form of a steady flame. In order to model this safety-relevant phenomenon correctly, the entire spatial distribution of potential ignition kernels must be accurately reproduced. In this work two different causes for the variation of the ignition location were identified: On the one hand, temperature fluctuations in the hot oxidizer have a direct influence on the ignition delay time. Since autoignition is very temperature-sensitive, even small temperature fluctuations cause a broad spread of the ignition locations. On the other hand, turbulence also has a significant influence on the ignition variation, which is mainly caused by large-scale turbulent structures.
For the first time, numerical simulations of autoignition processes under application-oriented gas turbine operating conditions were validated with suitable experimental reference data. It has been shown that the results from simplified autoignition experiments at atmospheric pressure cannot be directly transferred to real engine operating conditions, as the requirements for modeling differ significantly. Using a system-specific validation hierarchy, it was also possible to systematically identify the cause of the modeling uncertainties and to investigate them in detail. Based on the knowledge gained, a guideline for the simulation of autoignition processes for the design of new combustion chamber concepts is provided and the most promising optimization potential for the numerical prediction are deduced.

1 Introduction

1.1 Motivation

The spontaneous self-ignition of hot combustible mixtures is of great significance in many technical applications for transport and power generation. In automotive diesel engines the autoignition of fuel allows higher compression ratios and therefore enables higher efficiencies compared to spark-ignition engines [171]. In stationary gas turbine combustion, the preliminary mixing of fuel and oxidizer provides very homogeneous combustion with small mixture and temperature variations, which allows for very low NO_x emissions [93, 161]. However, a good understanding of autoignition is required to avoid premature ignition or flashback in the mixing duct, which can lead to critical damage of combustor components. Although, lean premixing is nowadays a standard in stationary gas turbines, it has not been possible to implement the technology in aero-engines. As stated by Bauer [13], the impeding factors are mainly a high pressure ratio and the very short ignition delay times of kerosene compared to natural gas. Furthermore, novel combustion concepts such as FLameless OXidation (FLOX) [173, 158] and Moderate or Intense Low oxygen Dilution (MILD) [24] rely on the partial recirculation of hot combustion gases. It seems likely that autoignition also plays an important role in the flame stabilization process in these systems.

For all these applications, a profound understanding and control of the underlying physical and chemical processes is required. Autoignition in turbulent flows is characterized by short time scales, comprehensive chemistry and a high sensitivity to boundary conditions, such as temperature, gas composition, residence time and turbulence intensity.

Numerical simulation is an essential tool in the design process of novel and optimized combustors. Especially with respect to complex experiments and extensive design studies, the complementary application of numerical simulations can considerably reduce the cost and time for development. This, however, requires a fast and inexpensive simulation tool with high credibility.

1.2 State-of-the-Art of Autoignition Simulation

Numerical Modeling

The numerical modeling of non-premixed combustion in turbulent flows is based on the combination of three different submodels for chemistry, turbulence and turbulence-chemistry interaction (TCI). The chemical reaction rates are described by reaction mechanisms and have a complex dependency on composition, temperature and pressure as well as empirical parameters. The turbulent motion of the flow is defined by conservation equations for mass, momentum and energy. However, the full resolution of all turbulent scales is very expensive and at present a direct computation for technical applications within reasonable cost and time is not feasible. Therefore, turbulence is described statistically, either entirely by Reynolds-averaged Navier-Stokes (RANS) methods or partially by Large-Eddy Simulation (LES). In LES only the small turbulent structures are modeled while the large turbulent structures are directly resolved. Finally, the TCI submodel accounts for the impact of unresolved turbulent fluctuations of temperature and composition on the averaged chemical source term. The TCI model depends on the output of the previous two submodels and is in itself a key element for the reliability of the numerical autoignition simulation.

Validation under Simplified Conditions

The credibility of a numerical model is gained through model validation by comparing the numerical simulation results with appropriate experimental data.
In recent years, the numerical simulation of autoignition in turbulent flows has been extensively investigated for generic test cases at atmospheric pressure and reduced Reynolds numbers [19, 28, 30, 124, 130, 109, 123]. In numerous publications, satisfactory qualitative agreement with experimental data could be obtained. Quantitatively, however, the ignition location could only be predicted within an accuracy of about 50 %. The limiting uncertainty sources were mainly attributed to experimental uncertainties in inflow temperature and uncertainties in the chemical reaction mechanisms. The majority of these studies were conducted for a simple jet-in-hot-coflow configuration at atmospheric pressure and low turbulence intensities.
However, automotive combustion engines and gas turbine combustors are characterized by complex geometries, high levels of turbulence and high pressure above 15 bar [13, 143, 67]. The credibility of the models gained under simplified physical conditions cannot be directly transferred to engine operating conditions. For instance, at high pressure different chemical pathways prevail [95, 169, 174] and the characteristics of turbulence-chemistry interaction can vary significantly with the turbulence properties of the flow [102, 101, 167].

Validation under Engine Operating Conditions

Although there are numerous studies on generic autoignition test cases, only very few autoignition studies have been conducted under application-oriented operating conditions at elevated pressure and high velocities. With both measurements and numerical simulation, it is much more challenging to achieve satisfying quantitative results under application-oriented high pressure conditions compared to generic, atmospheric test conditions.

Engine-relevant conditions are characterized by high velocities, temperatures and pressure, which make measurements by intrusive probes difficult [160]. But laser diagnostic measurements are also challenging. At high pressure, optical accessibility is limited by the pressure windows. These windows are also prone to degradation by high thermal loads. Thus, several laser-based diagnostic methods cannot be applied under high pressure conditions [153]. Furthermore, pressure-related effects, such as pressure broadening [110, 153], fluorescence quenching [110, 153] and beam steering caused by refractive index gradients [110, 160] reduce the quality of the results.

Also the numerical simulation of engineering application has to face challenging difficulties. For many technical applications, Reynolds-averaged Navier-Stokes (RANS) models provide satisfactory results at adequate cost [23]. However, in engineering flows, which are characterized by complex flow structures such as flow separation, recirculation and large-scale anisotropic vortices, RANS methods are less reliable [23, 53]. In such cases, Large-Eddy Simulations (LES) provide more accurate results. But the number of grid points required for wall-resolved LES is proportional to $N \sim Re_{L_x}^{13/7}$ [25, 27]. Since the flows in industrial combustion applications are typically highly turbulent, the high computational effort makes LES unfeasible for these applications [55]. Furthermore, in many application-oriented systems, it is difficult to specify the boundary conditions at the inlet of the computational domain with sufficient accuracy. Typical examples are the turbulence properties, such as turbulence intensity, length scale and boundary layer thickness at the inlet boundary as well as the precise specification of inlet species concentrations and temperature profiles [23].

In the following paragraph, relevant publications on application-oriented autoignition studies are presented. A detailed experimental and numerical study under diesel engine conditions has recently been published by Wright et al. [171]. They studied the autoignition of n-heptane spray in a constant volume combustion chamber at a pressure of 80 bar and 776 K air temperature. The pressure trace is used as a reference quantity for the validation. Although, there is a good agreement in the rate of pressure increase and total pressure rise, there are large differences in the ignition delay times. Through a sensitivity study, Wright et al. identified strong sensitivities to chemical mechanisms and the initial temperature.

Cano Wolff et al. [21, 20] and Heeg et al. [71, 68] investigated autoignition with respect to

LPP combustion in aero-engines. They experimentally analyzed the ignition process of fuel droplets in turbulent flow at elevated pressure (6 - 9 bar and 750 - 1100 K). Besides detailed images of the ignition process, they also present quantitative data for the ignition delay time of n-heptane, diesel and jet A-1. Unfortunately, no 3D-CFD studies have been conducted for this comprehensive test case.

An autoignition study under realistic engine conditions with respect to lean-premixed gas turbine applications has been conducted by Fleck et al. [42]. They experimentally investigated autoignition characteristics for the reheat system of the Alstom sequential gas turbine GT24 and GT26 [80] at a pressure up to 15 bar and temperatures above 1000 K. Hydrogen-rich fuel was injected in a jet-in-crossflow configuration. The ignition and flame stabilization process was investigated by the detection of the luminescence signal. Numerical simulations were conducted by Ivanova et al. [77] and the flame stabilization could be successfully reproduced. However, quantitatively, significant deviations to experimental data occurred. In a subsequent numerical investigation Prause et al. [151] conducted an extensive sensitivity study, which revealed that these deviations can partly be related to the measurement uncertainties of the hot gas temperature. Furthermore, relevant sensitivities were identified with respect to chemical reaction mechanisms and TCI modeling.

This study shows that in test cases under realistic engine conditions, numerical inaccuracies can be in the same order as experimental uncertainties, which might originate from measurement technique as well as uncertainties in the experimental setup. Therefore, it can be difficult to state whether any discrepancies are due to modeling deficiencies or due to experimental uncertainties. Furthermore, complex interdependencies between different submodels make it very complicated to relate potential model inaccuracies to specific submodel deficiencies. However, to prove the model credibility for industrial application as well as for efficient model optimization it is important to assess the specific submodel capabilities for the numerical prediction of turbulent autoignition.

1.3 Objectives and Methodology

The objective of this thesis is the quantitative assessment of the predictive capability of autoignition modeling methods under gas turbine operating conditions. The test case by Fleck et al. is used as a reference for the validation of the numerical simulation. The simulations are conducted with the DLR in-house code THETA. The Scale-Adaptive Simulation (SAS) turbulence model by Menter and Egorov [116] is combined with direct detailed finite rate chemistry. The TCI-closure of the averaged chemical source term is modeled by a multivariate assumed joint probability-density functions (APDF) approach, adopted by Gerlinger [56, 57].

To gain supplemental information of the submodel capabilities under engine operating conditions, the validation hierarchy approach [133] is applied. Additional deliberately-selected generic lab-scale test cases are analyzed, which resemble the technical system in specific characteristic properties. This allows for a better-suited model selection and effective submodel development. Diverse submodels for turbulence and chemical kinetics are applied and compared with respect to cost and capability. Furthermore, a detailed uncertainty quantification is conducted under gas turbine operating conditions. The most critical parameters in the prediction are revealed and suggestions for effective model improvement are presented. Finally, a best practice approach is provided for the numerical simulation of hydrogen autoignition in a sequential gas turbine.

The thesis is structured as follows. The fundamentals of hydrogen autoignition and the physical interaction of the chemical reaction with turbulent transport are discussed in chapter 2. In the subsequent chapter 3, the numerical methods and the applied models are described. A review of validation methodologies and its application in the gas turbine reheat system are provided in chapter 4. Finally, the results of diverse simulations and validation studies for simplified and technically relevant conditions are presented in chapters 5 and 6.

2 Fundamentals of Autoignition

The fundamental principles of autoignition are described in this chapter. First the autoignition process is analyzed for homogeneous systems with a focus on hydrogen/oxygen mixtures under gas turbine relevant conditions. These mixtures can ignite by different pathways, which depend mainly on temperature and pressure. The subsequent study of 1- and 2-dimensional non-premixed flows reveals that variations in the mixture fraction field and reaction rates lead to localized ignition at a most-reactive mixture fraction. Also transport processes of pre-ignition radicals and heat can play an important role in systems with large mixture fraction gradients. In the last two sections, ignition in 3-dimensional turbulent jet flames is reviewed. Ignition characteristics and modeling capabilities are studied in a straight jet and a jet-in-crossflow configuration, which is relevant for gas turbine applications.

2.1 Homogeneous Systems

In many technical devices combustion is initiated by an external ignition source, such as a spark ignitor. The subsequent combustion process is sustained by transport of heat and radicals from burned products to the fuel-oxidizer mixture. In such flames the burning rate is mainly controlled by thermodynamic quantities rather than chemical kinetics and the reaction zone is characterized by high gradients of temperature and radical concentration. A different mechanism prevails for autoigniting systems. Some specific gas mixtures are able to self-ignite under suitable conditions without any external addition of a local energy source. Radicals are formed within the mixture itself. The rate of generation is controlled by chemical kinetics and varies therefore widely for different fuels. Autoignition is characterized by an exponential increase in reaction rate. The increase in reaction rate can occur through thermal explosion or radical chain reactions at isothermal conditions. Usually autoignition is a mixture of the two mechanisms [139]. In the present section 2.1, the autoignition process is described for systems, which are spatially homogeneous in pressure, temperature and composition.

Thermal Explosion

The phenomenon of autoignition has first been explained by van't Hoff [166] in 1884 and was further refined and mathematically formulated by Semenov, Todes and Frank-Kamenentsky

[157] after 1927. They found that autoignition occurs suddenly at a specific, so-called "ignition temperature". Van't Hoff states that the ignition phenomena is an effect of the temperature dependency of the chemical reaction rates. Ignition takes place in combustible mixtures, which undergo exothermal chemical reactions. The amount of heat loss defines the further evolution of the system. If the chemical heat release exceeds the heat loss of the system, the temperature of the combustible mixture rises. This in turn leads to an increase of the chemical reaction rates whereby even more heat is released and the temperature increases exponentially. In the opposite case, when the heat loss is larger than its production, there is only slow reaction. The temperature drops until a constant value is reached. However, there is still the possibility of ignition by radical chain reaction [169, 95].

Radical Chain Reaction

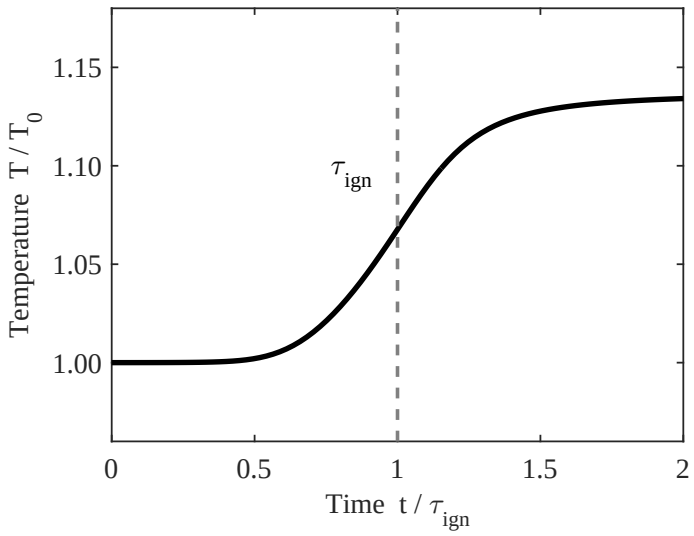

Figure 2.1.1: Temperature evolution of an igniting hydrogen mixture: The temperature stays almost constant for about 0.5 τ_{ign} before it rises significantly

A typical temperature evolution of a radical chain ignition process is shown in figure 2.1.1. The temperature stays almost constant for a considerable time (here for about 0.5 τ_{ign}) before a sudden increase leads to full chemical conversion. The time period before ignition is called the ignition delay time τ_{ign}. During this induction time, a radical pool is build up slowly until sufficient radicals are accumulated to initiate a significant transformation of the reactants. In this case the ignition delay time is controlled by the build-up of radicals instead of thermal heat release. The fundamentals of radical chain reaction were developed for a large extent by Semenov [157], who obtained the Nobel Price for his work in 1956. In the following, the radical chain process is demonstrated on the basis of the hydrogen/oxygen reaction system,

which is of special interest in the present work.

For intermediate pressure and temperature, the autoignition process can be reduced to the following reaction system [169].

$$\mathrm{H_2 + O_2 \rightarrow \dot{H} + HO_2} \qquad \text{chain initiation} \qquad \text{(I)}$$

$$\mathrm{\dot{H} + O_2 \rightarrow \dot{O}H + \ddot{O}} \qquad \text{chain branching} \qquad \text{(II)}$$

$$\mathrm{\ddot{O} + H_2 \rightarrow \dot{O}H + \dot{H}} \qquad \text{chain propagation} \qquad \text{(III)}$$

$$\mathrm{\dot{O}H + H_2 \rightarrow H_2O + \dot{H}} \qquad \text{chain propagation} \qquad \text{(IV)}$$

$$\mathrm{\dot{H} + O_2 + M \rightarrow HO_2 + M} \qquad \text{chain termination} \qquad \text{(V)}$$

The flammability of mixtures depends on the amount of free reactive radicals or rather the number of free valences (denoted by dots in the reaction equations). The number of free valences can be increased by chain branching reactions, such as reaction II. Chain propagation reactions, III and IV, redistribute the free valences, but do not increase their number. Finally, chain termination reactions, such as reaction V, reduce the number of free valences.

$$\frac{\mathrm{d[H]}}{\mathrm{d}t} = k_\mathrm{I}[\mathrm{H_2}][\mathrm{O_2}] - k_\mathrm{II}[\mathrm{H}][\mathrm{O_2}] + k_\mathrm{III}[\mathrm{O}][\mathrm{H_2}] + k_\mathrm{VI}[\mathrm{OH}][\mathrm{H_2}] - k_\mathrm{V}[\mathrm{H}][\mathrm{O_2}][\mathrm{M}] \qquad (2.1.1)$$

$$\frac{\mathrm{d[O]}}{\mathrm{d}t} = k_\mathrm{II}[\mathrm{H}][\mathrm{O_2}] - k_\mathrm{III}[\mathrm{O}][\mathrm{H_2}] \qquad (2.1.2)$$

$$\frac{\mathrm{d[OH]}}{\mathrm{d}t} = k_\mathrm{II}[\mathrm{H}][\mathrm{O_2}] + k_\mathrm{III}[\mathrm{O}][\mathrm{H_2}] - k_\mathrm{VI}[\mathrm{OH}][\mathrm{H_2}] \qquad (2.1.3)$$

$$\frac{\mathrm{d}[n]}{\mathrm{d}t} = \frac{[\mathrm{H}] + 2[\mathrm{O}] + [\mathrm{OH}]}{\mathrm{d}t} \qquad (2.1.4)$$

$$\frac{\mathrm{d}[n]}{\mathrm{d}t} = k_\mathrm{I}[\mathrm{H_2}][\mathrm{O_2}] + 2k_\mathrm{II}[\mathrm{H}][\mathrm{O_2}] - k_\mathrm{V}[\mathrm{H}][\mathrm{O_2}][\mathrm{M}] \qquad (2.1.5)$$

The production rates of the three radicals $\ddot{\mathrm{O}}$, $\dot{\mathrm{H}}$ and $\dot{\mathrm{O}}\mathrm{H}$ are given by the sum of their respective reaction rates in equations 2.1.1 - 2.1.3. The rate of the free valences $\mathrm{d}[n]/\mathrm{d}t$ can be derived by multiplying the production rates with the number of the free valences (factor 1 for $\dot{\mathrm{H}}$ and $\dot{\mathrm{O}}\mathrm{H}$ and 2 for $\ddot{\mathrm{O}}$). The final production rate of free valences for the whole system (eq. 2.1.4) equates to the sum of the three rates, which are given by equations 2.1.1 - 2.1.3. The first term in equation 2.1.5 is the rate for chain initiation. Since the concentrations of

the major species are almost constant prior to explosion, this term can be taken as constant during the induction period. The build up of the free valences is determined by the balance of the second and third term. If the chain branching term $2k_{\mathrm{II}}$ is larger than the chain termination $k_{\mathrm{V}}[\mathrm{M}]$ the number of free valences increases exponentially. However, if the chain termination V dominates the chain branching II, ignition cannot proceed through this path. Therefore, a characteristic crossover condition is given by relation 2.1.6.

$$2k_{\mathrm{II}} = k_{\mathrm{V}}[\mathrm{M}] \tag{2.1.6}$$

$$k = AT^{\beta}\exp\left(-\frac{E_{\mathrm{a}}}{RT}\right) \tag{2.1.7}$$

$$[\mathrm{M}] = \frac{p}{RT}\left[1 + (1 - t_{\mathrm{b,H2O}})\, X_{\mathrm{H2O}} + (1 - t_{\mathrm{b,H2}}) X_{\mathrm{H2}}\right] \tag{2.1.8}$$

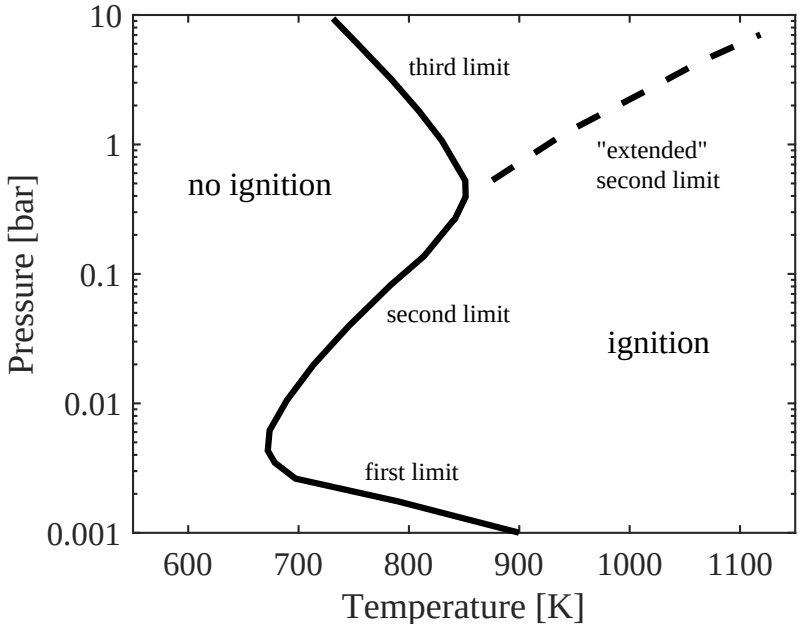

Figure 2.1.2: Ignition limits of stoichiometric H_2/O_2 mixtures; data from Lewis and Elbe [95] and Yetter et al. [174]

The reaction rates k and the third body concentration [M] can be determined from equations 2.1.7 and 2.1.8. The parameters A, β, E_{a} and $t_{\mathrm{b},\alpha}$ are reaction constants, which are given by chemical kinetic mechanisms. R is the universal gas constant. It is obvious, that the ignition condition in equation 2.1.6 depends mainly on temperature and pressure and to a small extent on the composition. The crossover condition is visualized in figure 2.1.2 as "second ignition limit". In addition to this ignition path, there are two other ignition processes in the hydrogen/oxygen reaction system. At a low pressure, ignition is restrained by diffusion and

destruction of radicals at the vessel walls. But this path is not of relevance for the conditions, which are investigated in this work. The third, high pressure ignition limit, however, is very important.
At elevated pressure and low temperature, reaction V is preferred over reaction II. In this case there is sufficient time to accumulate the intermediate species HO_2 through slow reaction V. Further transformation to hydrogen peroxide H_2O_2 is possible by supplemental reactions VI and VII.

$$HO_2 + HO_2 \rightarrow H_2O_2 + O_2 \qquad \text{conversion of } HO_2 \text{ to } H_2O_2 \qquad \text{(VI)}$$

$$H_2 + HO_2 \rightarrow \dot{H} + H_2O_2 \qquad \text{conversion of } HO_2 \text{ to } H_2O_2 \qquad \text{(VII)}$$

$$H_2O_2 + M \rightarrow \dot{O}H + \dot{O}H + M \qquad \text{chain branching} \qquad \text{(VIII)}$$

Finally, at a large concentration of HO_2 and H_2O_2, thermal explosion emerges through the decomposition of H_2O_2 in reaction VIII accompanied with large heat release. This reaction path forms the third explosion limit.
The solid line in figure 2.1.2 represents the steady-state ignition limits. However, the constraint for the second explosion limit also applies for transient considerations. It is called the "extended second limit" (dashed line). Strictly speaking it is not an ignition limit, but it separates the two reaction pathways. At a specific, elevated pressure, a so called crossover temperature T_{co} can be derived from equations 2.1.6 to 2.1.8. If the temperature of the ignitable system is below this crossover temperature, the system will ignite through the reaction path of the third limit. At temperatures above crossover, the reaction path of the second limit with H-atom build-up prevails.

2.2 Non-premixed Laminar Counterflow

In non-premixed systems, a set of different mixture states is present, which can range from pure oxidizer to pure fuel. Furthermore, non-premixed flows are also subject to diffusive transport processes. The consequences for the ignition process are discussed in this section.
A very revealing study for the influence of mass transport and strain on hydrogen ignition was conducted by Kreutz and Law [91]. They numerically investigated counterflowing jets of diluted H_2 in N_2 versus heated air for a large range of temperatures, pressures and strain rates. Their findings were later also verified in experimental studies by Fotache et al. [47]. Kreutz and Law analyzed the steady-state properties of the counterflow configuration. The temperature of the hot air was increased stepwise to identify the ignition limits for specific pressures and strain rates.

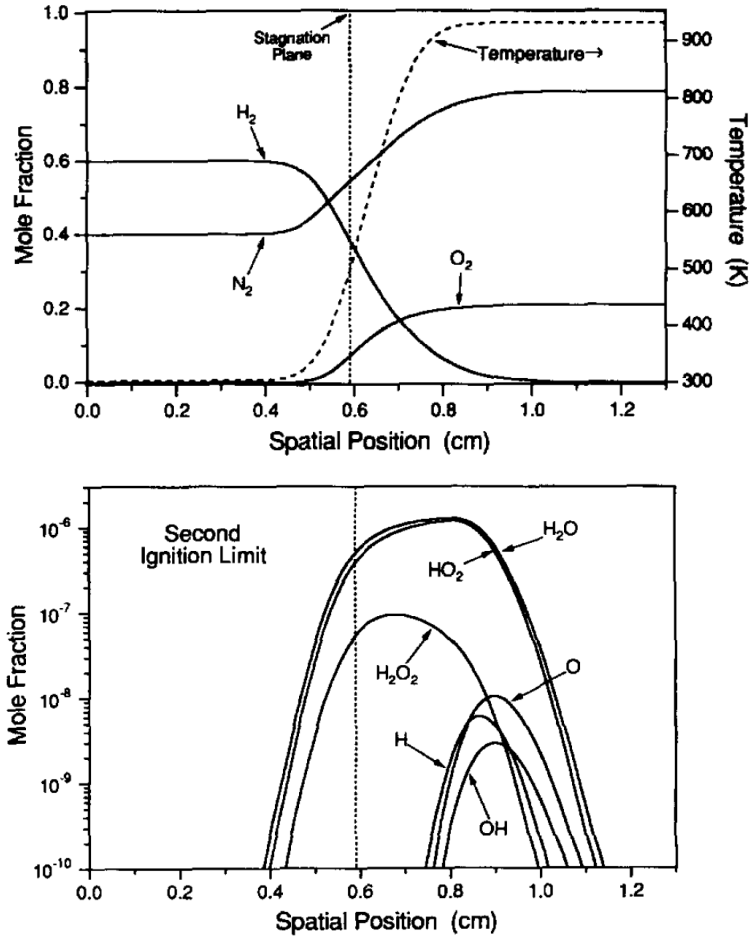

Figure 2.2.1: Species concentration profiles at the second ignition limit ($p = 1\,\text{bar}$, $T = 930.7\,\text{K}$, $\tilde{a} = 100\ /\text{s}$ and $X_{\text{H2}} = 0.06$), figures reprinted from Kreutz and Law [91] with permission from Elsevier

Figure 2.2.1 shows the state of the system just before ignition at the second ignition limit for a pressure of 1 bar and a pressure-weighted strain rate of $\tilde{a} = 100\ /\text{s}$.

The most significant variation of major species and temperature (top figure) lies between a spatial position of 0.4 and 1.0 cm. At this condition (before ignition) the educt species are purely mixed and there is no considerable conversion by reaction. The radical build-up (lower figure) evolves in form of a localized kernel, which is identified by the peak of the radical concentrations (O, H, OH). It is located at high temperature (99 % of the maximum value) and low hydrogen concentration (4 % of maximum). Furthermore, it is obvious that the concentrations of the small radicals O, OH and H peak at a different location and their profiles are more narrow compared to the larger radical species HO_2 and H_2O_2. This indicates, that the larger radicals are more affected by mass transport out of the actual highly reactive kernel (at 0.9 cm). Kreutz and Law demonstrated that the small reactive radical species,

which have very high reaction rates, are produced and consumed so fast that mass transport does not influence their profiles significantly. Whereas the larger species, HO_2 and H_2O_2 are more stable and less reactive. They are called "sink species". Their reaction rates are in the order of mass transport processes. Thereby, HO_2 and H_2O_2 molecules, which are produced within the ignition kernel, are affected by mass transport and are partly removed from the kernel center.

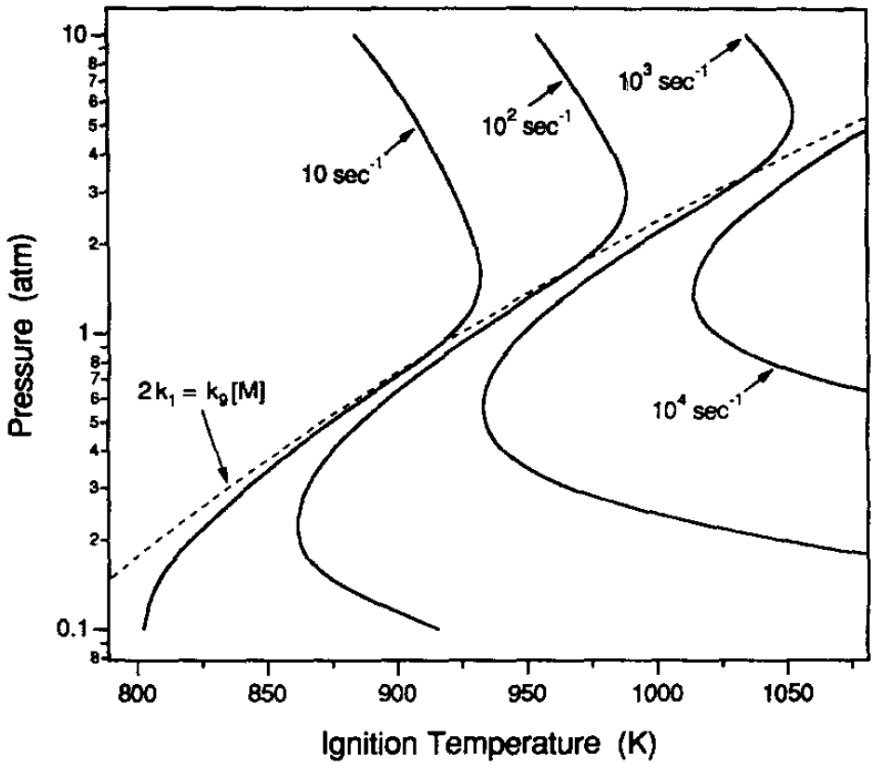

Figure 2.2.2: Ignition limits at different density-weighted strain rates $\tilde{a}$, figure reprinted from Kreutz and Law [91] with permission from Elsevier

In the counterflow configuration, the diffusive mass transport is directly related to the strain rate. The impact of varying strain rates on the ignition limits is shown in figure 2.2.2. Kreutz and Law found that the ignition process in the second limit, which depends mainly on the build-up of H-radicals, is little affected by strain. Whereas in the third limit, the ignition line is shifted considerably with increasing strain. This arises from the fact that the slow and less reactive species HO_2 and H_2O_2 play an important role in the ignition process of the third limit.

In summary, this study shows that the interaction between mass transport and chemical reaction varies significantly with the reaction path. Hence, the influence of pressure must be attentively considered in validation studies for turbulent autoignition.

2.3 Turbulent Mixing Layer

In turbulent flows, there is also a large variation of strain rates in addition to divers mixture states. Mastorakos et al. [105] identified two interesting phenomena of turbulent autoignition. They conducted 2D direct numerical simulations (DNS) of turbulent shearless mixing layers of hydrogen and hot air. A turbulent isotropic field was applied to the system to investigate the effect of turbulent mixing on the evolution of ignition. The first interesting finding is that ignition always occurs at a specific most-reactive mixture fraction Z_{mr}, which can be assessed by simple preliminary studies of homogeneous systems. The dimensionless mixture fraction Z is defined such, that it is 0 in the oxidizer flow and 1 in the fuel flow. The mixture fraction with the lowest autoignition delay time is the most reactive mixture fraction Z_{mr}.

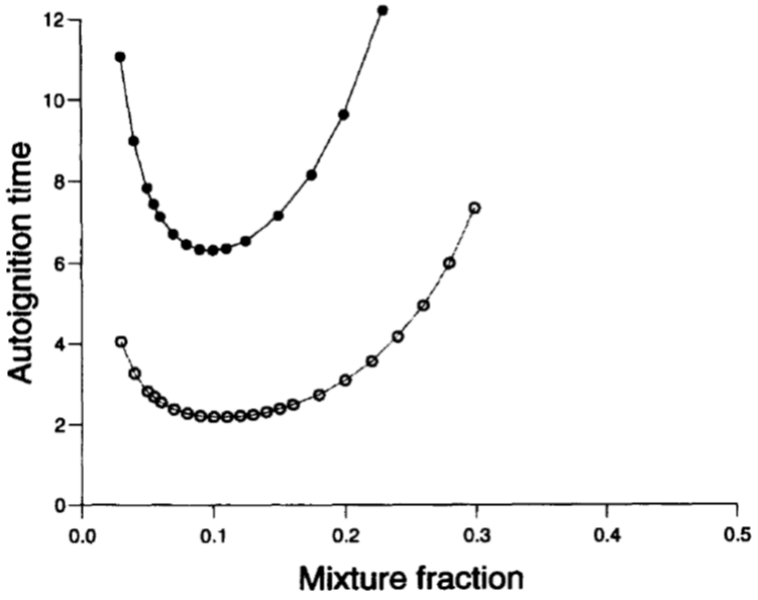

Figure 2.3.1: Calculation of ignition delay (non-dimensional) in homogeneous H_2/air mixtures for 1000 K (top) and 1100 K (bottom), figure reprinted from Mastorakos et al. [105] with permission from Elsevier

In Figure 2.3.1 homogeneous ignition delay time calculations are presented for a broad range of mixture fractions. The ignition delay times were non-dimensionalised by an "acoustic time" of $t_{\mathrm{ref}} = 1.259 \cdot 10^{-5}$ s [105]. In this test case, the most-reactive mixture fraction is located for the two air temperatures 1000 K (top graph) and 1100 K (bottom graph) at $Z_{\mathrm{mr}} \approx 0.1$. In hydrogen mixtures the most reactive mixture fraction is usually very lean, since the build-up of hydrogen radicals increases exponentially with temperature and only linear with the H_2 concentration (eq. 2.1.7).

The second finding of Mastorakos' study is that not all locations along Z_{mr} ignite at the same time, but in form of separated kernels. The first kernels appear at locations with low scalar dissipation rate χ.

$$\chi = D \left(\frac{\mathrm{d}Z}{\mathrm{d}x_i} \right)^2 \tag{2.3.1}$$

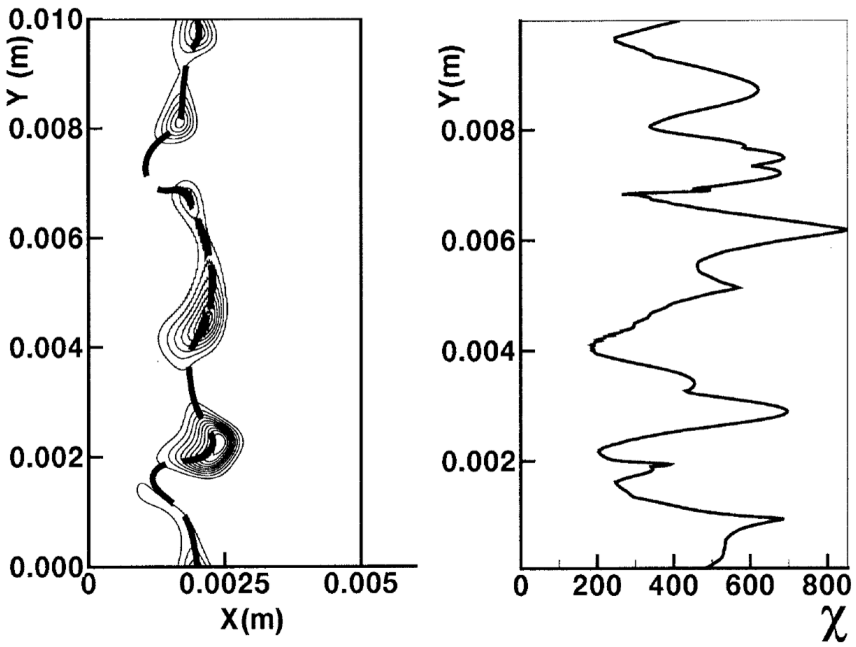

Figure 2.3.2: Ignition kernels, visualized by the local heat release (left) arise at locations with low scalar dissipation (right), figures reproduced from Hilbert and Thevenin [70] with permission from Cambridge University Press

This has been visualized very clearly by Hilbert and Thevenin [70] who repeated the 2D-DNS by Mastorakos. The results are presented in figure 2.3.2. The ignition locations are visualized in the left image by the instantaneous heat release. The thick dashed line represents the isoline of the most reactive mixture fraction. The right image shows the scalar dissipation rate χ along Z_{mr}. It is apparent that the location of ignition coincides with regions of low scalar dissipation. The scalar dissipation rate is proportional to the squared mixture fraction gradient (equation 2.3.1) and this in turn is directly related to the conduction and diffusion of chemically produced heat and radicals. For larger gradients, more heat and radicals are transported out of the reaction zone, whereby ignition can be delayed or even inhibited. The phenomena, which were identified in this 2D-DNS with reduced chemistry, were confirmed by several other DNS results with detailed chemistry [74, 70, 38] and 3-dimensional flows [162].

2.4 Turbulent Jet-in-Hot-Coflow

This section deals with the application of autoignition in technically relevant configurations. Appart from sequential gas turbines, the injection of fuel jets in hot oxidizer flows is also relevant for scramjet combustion and novel low pollution combustion systems, such as FLameless OXidiation (FLOX™) [173] and Moderate or Intense Low oxygen Dilution (MILD) [24].

2.4.1 Characteristics

Flow Characteristics

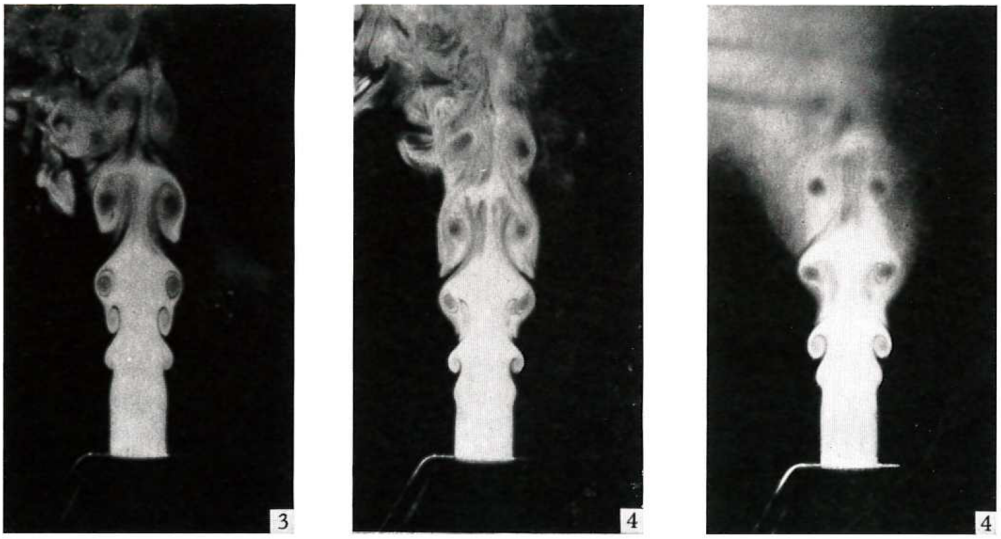

Figure 2.4.1: Several instantaneous pictures of vortical structures in a jet-in-coflow, figures reproduced from Becker and Massaro [15] with permission from Cambridge University Press

First, the flow structure of non-reacting turbulent jet flows is reviewed. A very illustrative description of the mixing process can be found in the publication by List [98]. He showed that the spreading of turbulent jets originates from large-scale structures, which are generated at the jet boundaries. When the jet leaves the pipe orifice, a shear layer develops at the interface between the jet and the ambiance. With increasing distance, the shear layer becomes unstable and grows rapidly. Ring vortices are formed, which carry jet fluid into the ambient fluid and vice versa. These large-scale structures are of coherent nature and a characteristic vortex frequency f can be determined, which depends on the pipe diameter D_{jet} and the pipe bulk velocity $\overline{u}_{\text{jet}}$. A characteristic Strouhal number St exists, which is in the range 0.3 - 0.5 [98].

$$St = f \frac{D_{\text{jet}}}{\overline{u}_{\text{jet}}} \tag{2.4.1}$$

While these ring vortices are transported downstream, they grow in size. The vortex rotation causes a secondary circumferential instability, which leads to break up [178, 155, 98] of the large-scale structures (figure 2.4.1). Subsequently, the smaller eddies dissolve into even smaller turbulent vortices [142]. Through this vortex decay by turbulence cascade, turbulent mixing proceeds at increasingly smaller scales.

Flame Characteristics of Autoignited Jets

A prominent experiment for the study of autoignition in turbulent flows has been set up by Cabra et al. in Berkeley in 2002. They investigated lifted flames in turbulent jets of hydrogen [19] and methane [18], which are injected into a hot vitiated coflow. In the following years, a broad range of different parameters has been studied for the jet-in-hot-coflow configuration by research groups in Adelaide [28, 109, 108], Cambridge [106, 102, 103], Delft [136, 137, 112] and Stuttgart [111, 9]. In all these experiments, the flames were initiated by autoignition. There is also a large number of numerical studies for these test cases. The simulations provide valuable information, such as high spatial and temporal resolution and simultaneous data of mixture fractions, temperature and intermediate species concentrations. Recently, also 3D DNS of jets-in-hot-coflow were presented [176, 85], which allow a very detailed and accurate insight into the processes of autoignition in turbulent jets.
Three different flame regimes with specific characteristics were observed in the experimental and numerical work. These are described in the following.

1. In the majority of these investigations (e.g. [19, 28, 109, 103, 106, 103, 136, 9]), a **steady lifted flame** evolved in the jet flow and stabilized a few pipe diameters downstream of the fuel nozzle. However, the instantaneous lift-off height was fluctuating significantly in most of these test cases. In some experiments the lift-off height fluctuations are in the order of up to 20 % of the averaged height [64]. LES computations [129] revealed, that separate ignition kernels are formed below the flame base and are transported downstream, where they eventually merge with the coherent flame base. The final formation of coherent flame structures (in contrast to a pure conglomeration of kernels as in 2.) can probably be related to a dissipative reduction of jet turbulence with increasing height. Hence the larger the distance from the nozzle, the smaller is the turbulent interference of the chemical ignition process. In all these test cases, the coflow turbulence is very weak compared to the initial jet turbulence. In the test cases with hydrogen fuel, which are of special interest in the present research study, autoignition proceeds through the chemical pathway above crossover (sec. 2.1: $T > T_{\mathrm{co}} \approx 920\,\mathrm{K}$ at 1 bar), where H-atom build-up determines the ignition delay time. For this reaction path, the impact of turbulence is also comparable small (sec. 2.2).

2. Markides and Mastorakos [102, 101] experimentally investigated the ignition process in test cases with strong coflow turbulence (produced by a turbulence grid) and reduced coflow temperature. In these configurations they identified a further regime, where no coherent flame structure exists. Ignition kernels are produced permanently a few diameters downstream of the inlet plane. Instead of forming a stable flame, these kernels were quenched after a short downstream travel. This ignition phenomenon is called **random spots regime**. Their hydrogen case was operated under conditions around the crossover temperature (sec. 2.1). At higher temperatures the regime switched to a steady lifted flame. However, there are only very few studies on this regime.

3. Furthermore, Markides and Mastorakos described a third combustion regime at low coflow and low jet velocities. When the local velocities at the ignition location are lower than the flame speed, the autoignition event is followed by intermediate **flashback and a jet diffusion flame** is formed at the fuel nozzle.

Indicators for Stabilization Mechanism of Lifted Flames

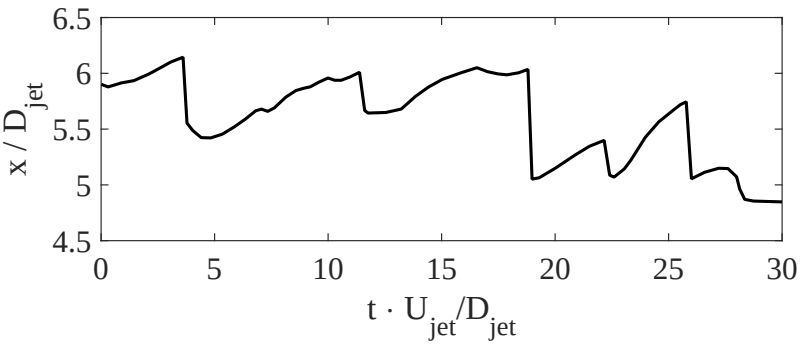

Figure 2.4.2: Temporal evolution of lift-off height from 3D-DNS by Yoo et al. [175]

Unfortunately, there are only very few studies on the latter two regimes. But extensive research was conducted on the lifted flame regime and very interesting characteristics of turbulent autoignition could be revealed by combined experimental and numerical work. Therefore, this section is focused on the lifted flame regime. During the first experiments by Cabra et al. [19, 18] it was unknown whether the lifted flame is stabilized by autoignition or flame propagation. With the help of numerical simulation, it was found that auotignition is the prevailing stabilization mechanism. The indicators, which can be applied to differ between autoignition and flame propagation are described in the following.

1. A very straightforward method is the **temporal tracking of the most upstream flame location** [129, 175]. A saw-tooth shape (as presented in figure 2.4.2) supports the

assumption that the flame is stabilized by consecutive autoignition events. In this case, a kernel occurs some distance upstream of the coherent flame front and travels slowly downstream until it merges with the flame base. Afterwards a new independent kernel is formed upstream again and a similar loop is repeated. When the most upstream flame location (which correlates with the lift-off height) is recorded versus time, the graph shows a saw-tooth shape with a sudden drop in lift-off height, followed by a steady increase. In contrast, downstream flame propagation would result in a steady decrease of lift-off height.

2. Gordon et al. [64] analyzed the **balance between convective and diffusive transport with chemical reaction** for the Cabra test cases. They found that the reaction budget is balanced by convection, which is taken as indicator for autoignition. Whereas a diffusive-reactive balance would be characteristic for premixed flames.

3. An other indicator for stabilization by autoignition is the **relative location of certain radical species with respect to the flame zone**. For the hydrogen flames the build up of HO_2 prior to H, O and OH indicates the occurrence of autoignition. In the methane flame, autoignition is the responsible stabilization mechanisms if a radical pool of precursor species, such as CH_3, CH_2O, HO_2 and H_2O_2 is located upstream of the flame region.

4. A **chemical explosive mode analysis** in combination with a transport Damköhler number Da_c has been developed and applied by Lu et al. [99] and Yoo et al. [175]. Large local positive eigenvalues of the Jacobian matrix of the chemical source terms indicate highly explosive mixtures. To account for diffusive losses, the chemical explosive modes are weighted with the scalar dissipation rate (equation 2.3.1) $Da_c = \lambda_{exp}/\chi$. Probable ignition locations are indicated by $Da_c \gg 1$.

2.4.2 Numerical Modeling

Numerous simulation studies were conducted for the jet-in-hot-coflow. RANS and LES turbulence modeling was applied in combination with many different combustion models, such as the Eddy Dissipation Concept (EDC) [19, 123], Transported Probability Density Functions (TPDF) [19, 18, 63, 64, 41, 104, 124, 79] and Assumed Probability Density Functions (APDF) [30], Laminar Flamelet [31, 37, 72, 73] and Conditional Moment Closure (CMC) [128, 163]. The comparison with experimental data showed, that the majority of simulations could capture the steady lifted flames reasonably well. However, in many cases there was a considerable deviation in the averaged flame lift-off height, which was often in the range

of 100 %. This discrepancy can be attributed to specific experimental as well as modeling uncertainties, which are summarized below.

1. **The lift-off height is very sensitive to the coflow temperature.** For example in the Berkeley hydrogen test case, 1 % temperature variation, which is about 10 K, leads to a doubling of the lift-off height. However, the expected error from thermocouple measurements is in the order of 30 K [19]. This uncertainty is also visible in the large deviation of comparative experimental results for this test case. The lift-off heights measured by Wu et al. [172] and Gordon et al. [63] under the same conditions differ by a factor of 6. Therefore, instead of comparing the absolute value of the lift-off height, some authors [130, 123] prefer to validate their simulations only with the general trend of lift-off height with coflow temperature.

2. Furthermore, it was found that uncertianties in **the composition of the hot coflow**, such as oxygen, water, hydrogen and hydroxyl concentrations, **can also affect the prediction of the lift-off height** [124, 28, 109, 61]. The quantitative sensitivities depend strongly on the specific configuration. But in general, the impact of composition inaccuracies is smaller compared to temperature uncertainties [124].

3. **The accuracy of the numerical simulations is very dependent on the kinetic mechanisms.** The variation of different kinetic mechanisms for the Berkeley hydrogen flame [19] led to a shift in lift-off height between 30 % and 60 % [104, 22, 30, 163].

Finally, most experimental reference data is focused on the average lift-off height. However, as described above, there is actually a large temporal variation in the lift-off height and only very limited information is published on lift-off height distributions and other statistical quantities.
But in the gas turbine application, which is the main focus of the present work, the most upstream ignition location is of utmost significance. In a jet-in-crossflow, a kernel, which occurs very far upstream can interact with the recirculation zone and initiate flame anchoring. More details of this phenomenon are provided in section 2.5 and chapter 6.

2.5 Turbulent Jet-in-Hot-Crossflow

Whereas much research has been done on autoignition in free jets-in-hot-coflow, autoignition in jets-in-hot-crossflow has been scarcely investigated. Although the jet-in-crossflow configuration is more complex compared to free jets, it is often employed in energy and propulsion systems due to its superior mixing properties in the near-field.

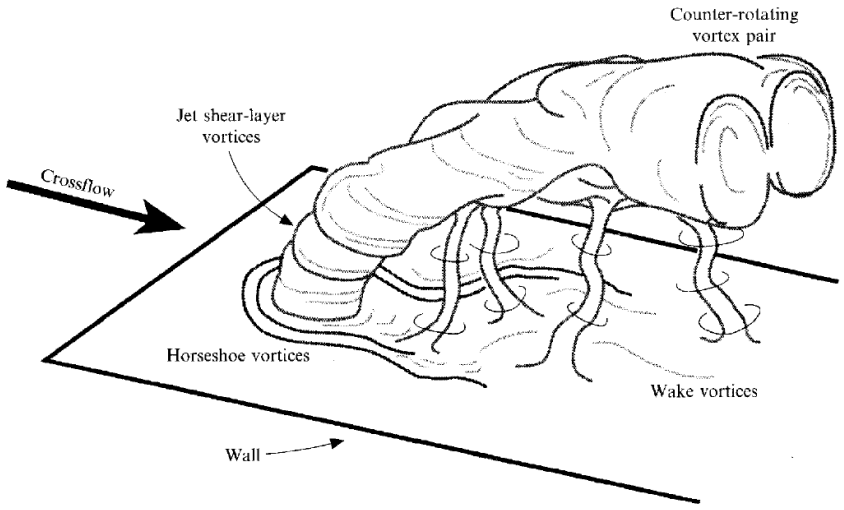

Figure 2.5.1: Vortical structures in a jet-in-crossflow, figure reproduced from Fric and Roshko [50] with permission from Cambridge University Press

2.5.1 Characteristics

Flow Characteristics

A jet with velocity u_{jet} and density ρ_{jet} is injected perpendicular into a crossflow with velocity u_{cf} and density ρ_{cf}. In this work only round jets are considered. Jets-in-crossflow can be characterized by the momentum flux ratio J.

$$J = \frac{\rho_{\text{jet}} u_{\text{jet}}^2}{\rho_{\text{cf}} u_{\text{cf}}^2} \tag{2.5.1}$$

For constant density flows, the velocity ratio R is often used.

$$R = \frac{u_{\text{jet}}}{u_{\text{cf}}} \tag{2.5.2}$$

In this work only test cases with low momentum ratios in the range of $J = 1\text{-}4$ ($R = 1\text{-}2$) are considered. In these cases, the jet is bent strongly by the crossflow. In the wake, the jet is lifted from the wall and crossflow fluid is mixed in.

The jet-in-crossflow consists of a complex vortex system. The major vortex structures are presented in figure 2.5.1. A recent review can be found in Karagozian [81]. The most prominent vortex structure is the counter-rotating vortex pair. It is produced by the bending of the jet and is most relevant for enhancing the mixing process. This flow structure, as well as the horseshoe vortices, which form around the base of the jet, are of steady-state nature.

The jet shear layer and wake vortices have a periodic character [81]. The jet shear layer vortices are produced in the transition from the pipe to the jet flow by a similar principle as in the straight jet-in-coflow. Kelso et al. [84] found that the shear layer is produced by a Kelvin-Helmholtz-like instability at low Reynolds numbers below 500 - 1500. At higher Reynolds numbers, the shear layer roll-up occurs close to or even within the pipe exit. Under these conditions the shear layer roll-up is periodic and of larger scale. Finally, vertical upright vortices evolve periodically in the wake on the leeward side of the jet. These wake vortices carry fluid from the boundary layer into the jet and it is assumed that they are initiated within the wall boundary layer. The frequency of these wake vortical structures can be about 10 times smaller compared to the shear layer vortices [66, 12].

Flame Characteristics of Autoignited Jets

Only few publications address the issue of autoignition in jets-in-crossflow. However, two different flame regimes were considered so far.

1. **Steady lifted flames** were observed in a couple of experiments. The majority of these studies were performed with methane [159, 54, 87] and one study also included hydrogen admixtures at high temperatures, which were above the crossover (sec. 2.1) and hence in the second explosion limit [165]. In all studies, autoignition and subsequent lifted flame stabilization were located clearly separated from the jet nozzle. High-speed measurements revealed that individual ignition kernels are formed upstream of the flame front. Furthermore, it was observed that combustion takes place in very thin flame fronts with sharp OH gradients [159, 87]. At lower jet momentum ratio and higher coflow temperature, the flame stabilized closer to the nozzle. At very short ignition times compared to the flow residence time, the flame even anchored circumferencially around the orifice [165, 87].

2. Fleck et al. [42, 44, 45] conducted experiments with pure hydrogen and also mixtures of natural gas and hydrogen at crossflow temperatures between $T_{\mathrm{cf}} = 1100$ - $1200\,\mathrm{K}$, jet velocities in the order of $u_{\mathrm{jet}} = 100\,\mathrm{m/s}$ and pressures up to $15\,\mathrm{bar}$. The hydrogen test case at $15\,\mathrm{bar}$ resembles the relevant gas turbine conditions, which are of interest for the present work. Therefore, this experiment is chosen as high pressure subsystem reference data and is presented in further detail in chapter 6. Under these test conditions, ignition proceeds along the reaction path below the crossover temperature (sections 2.1 and 5.1), where the build-up of HO_2 and H_2O_2 determine the ignition delay time (third ignition limit). In this test case, ignition occurred in form of separated ignition kernels. Under the relevant test conditions, the ignition kernels allways occurred after an axial distance of about 5 pipe diameters. The majority of these kernels were transported

with the main flow out of the channel. Insofar, this is similar to the **random spots regime**, which was observed by Markides and Mastorakos for the jet-in-coflow [102]. But in contrast to the jet-in-coflow configuration, the jet-in-crossflow has a region of low velocity on the leeward side of the bent jet. Random ignition kernels, which occurred very close to this region at about $x/D = 5$, interacted with the low velocity field and **initiated upstream flame propagation and subsequent flame anchoring in the low velocity region** on the leeward side of the jet nozzle.

A similar characteristic behaviour was observed in the 3D-DNS of Abdilghanie et al. [1]. They investigated a nitrogen-diluted hydrogen jet at intermediate temperatures $T_{\text{jet}} = 850\,\text{K}$ and $T_{\text{cf}} = 930, 950\,\text{K}$. At the beginning of the simulations, spatially-isolated ignition kernels were observed, which were convected out of the computational domain. Subsequent ignition events, which occurred further upstream lead to flame anchoring at the leeward side of the jet.

Flame Characteristics of Externally Ignited Jets

The study of ignition phenomena under gas turbine conditions in chapter 6 is not solely focused on autoignition, but considers also subsequent flame propagation and flame stabilization processes. To gain a better understanding of flame stabilization in jets-in-crossflow, an additional literature review on forced ignition is provided in this section.

A test case, which was also conducted with hydrogen/ nitrogen fuel and at elevated crossflow temperatures ($T_{\text{cf}} = 750\,\text{K}$) has been investigated experimentally by Steinberg et al. [164] and through direct numerical simulations (DNS) by Grout et al. [88, 65, 66, 121]. The characteristic features of the stabilized flame are similar to the experiment by Fleck et al. [42]. A stable flame root anchors in the low velocity region on the leeward side of the jet at about 2 diameters axial distance from the jet inlet.

Another very interesting experiment was conducted by Micka and Driscoll [120] under RAMJET-conditions ($T_{\text{cf}} \approx 1400\,\text{K}$ and $u_{\text{cf}} \approx 468\text{-}487\,\text{m/s}$ ($Ma = 0.6$)). Two fuel compositions, pure hydrogen and a hydrogen/ethylene mixture, were applied with jet velocities of 432 m/s and 1198 m/s ($Ma = 1$). The jet-crossflow mixture was ignited by a spark about 2 diameters downstream of the injection. In the hydrogen case, the flame shape and anchoring are comparable to the results of Grout et al. [66] and Steinberg et al. [164]. But the ethylene-hydrogen mixture exhibits a different characteristic. The flame base, which is visible by high OH* and CH* concentrations, is located at a very large axial distance of about 15 diameters. However, the region upstream of the flame base is marked by a high concentration of formaldehyde, which is a precursor of autoignition. Therefore, the authors assume, that pre-reactions affect the flame speed of the lifted flame. They call this regime an **autoignition-assisted flame**.

2.5.2 Numerical Modeling

There are very few studies on the numerical modeling of autoignition in jets-in-hot-crossflow. Prathap et al. [144] and Galeazzo et al. [54] simulated a lifted methane flame at elevated pressure up to 8 bar. They found that the turbulent mixing cannot be accurately predicted with RANS simulations. The application of LES produced much better results. Furthermore, they compared two different combustion models, namely a combination of the eddy dissipation and finite rate chemistry models (EDM/FRC) and a presumed joint PDF model (JPDF) in combination with a mixture fraction and progress variable approach. While no satisfying result could be obtained with the EDM/FRC model, a good qualitative agreement with experimental measurements was achieved with the JPDF model.
A detailed numerical study on reacting and non-reacting jets-in-crossflow was performed by Ivanova et al. [77, 75]. They also conducted URANS (unsteady Reynolds-averaged Navier-Stokes) and SAS (Scale-Adaptive Simulation) computations of the high pressure experiment by Fleck et al. [46]. The focus of this investigation was on the reproduction of the flame anchoring in the low velocity region on the leeward side of the jet nozzle. The anchoring of the stable flame could be predicted well with the SAS model, while the URANS model gave significant discrepancies against the experimental results.

3 Numerical Methods

The numerical combustion simulation is based on the finite volume approach, where the fluid domain is subdivided into a large number of discrete computational cells. For each cell, transport equations for mass (eq. 3.1.1 and 3.1.4), momentum (eq. 3.1.2) and energy (eq. 3.1.8) are solved [132]. Moreover, additional modeling approaches are required for an efficient simulation of turbulent fluctuations, chemical source terms and the interaction of turbulence and chemical reaction.

3.1 Governing Equations

It is assumed that the flows in all considered test cases are dynamically incompressible [57, 26]. This applies for low Mach number flows, where the change in density, which is caused by pressure variations is insignificant. However, density changes due to a change in temperature or concentration are considered [57]. Furthermore, the Einstein summation convention is applied.

Balance of mass The continuity equation is given in Einstein summation convention [132]. The numerators i indicate the spatial directions (j and k accordingly).

$$\frac{\partial \rho}{\partial t} + \frac{\partial \left(\rho u_i\right)}{\partial x_i} = 0 \tag{3.1.1}$$

Balance of momentum

$$\frac{\partial \left(\rho u_i\right)}{\partial t} + \frac{\partial \left(\rho u_i u_j\right)}{\partial x_i} = -\frac{\partial p}{\partial x_i} + \frac{\partial \tau_{ij}}{\partial x_i} \tag{3.1.2}$$

These three equations apply for non-constant density flows without gravitation and external forces [132]. For a Newtonian fluid the 3-dimensional viscous stress tensor τ_{ij} can be described by Stokes' law.

$$\tau_{ij} = \mu \left[\left(\frac{\partial u_i}{\partial x_j} + \frac{\partial u_j}{\partial x_i} \right) - \frac{2}{3} \delta_{ij} \frac{\partial u_k}{\partial x_k} \right] \tag{3.1.3}$$

The dynamic viscosity μ is a temperature dependent property of the fluid. The Kronecker symbol δ_{ij} is 1 for same indices $i = j$ and is 0 otherwise.

Balance of species mass fractions

$$\frac{\partial(\rho Y_\alpha)}{\partial t} + \frac{\partial(\rho u_i Y_\alpha)}{\partial x_i} = \frac{\partial j_{\alpha i}}{\partial x_i} + \omega_\alpha \tag{3.1.4}$$

In this equation the effects of thermal and pressure diffusion are neglected [132]. For a system with N_s species, only N_s - 1 mass fractions are determined by the species mass balance. The last species, in general an inert one, is solved by the sum over all species mass fractions.

$$\sum_{\alpha=1}^{N_\mathrm{s}} Y_\alpha = 1 \tag{3.1.5}$$

The modeling of the chemical source term ω_α is described in section 3.2.1. The diffusion flux $j_{\alpha i}$ can be described by Fick's laws of diffusion with the species mass diffusion coefficient D_α.

$$j_{\alpha i} = \rho D_\alpha \frac{\partial Y_\alpha}{\partial x_i} \tag{3.1.6}$$

The diffusion coefficient D_α can be expressed as function of the dynamic viscosity and a Schmidt number Sc.

$$D_\alpha = \frac{\mu}{\rho Sc} \tag{3.1.7}$$

Conservation of enthalpy

$$\frac{\partial(\rho h)}{\partial t} + \frac{\partial(\rho u_i h)}{\partial x_i} = \frac{\partial q_i}{\partial x_i} \tag{3.1.8}$$

In this balance heat radiation, potential and kinetic energy as well as work by viscous stresses are not considered [57]. The enthalpy flux q_i is composed of the heat flux by temperature gradients (Fourier's law of heat conduction) and the enthalpy flux by species mass diffusion.

$$q_i = \lambda \frac{\partial T}{\partial x_i} - \sum_{\alpha=1}^{N_\mathrm{s}} h_\alpha j_{\alpha i} \tag{3.1.9}$$

Equation 3.1.9 can be transformed in terms of enthalpy gradients with the spatial differential of the enthalpy [57].

$$\frac{\partial h}{\partial x_i} = c_\mathrm{p} \frac{\partial T}{\partial x_i} + \sum_{\alpha=1}^{N_\mathrm{s}} h_\alpha \frac{\partial Y_\alpha}{\partial x_i} \tag{3.1.10}$$

$$q_i = \frac{\lambda}{c_\mathrm{p}} \frac{\partial h}{\partial x_i} - \sum_{\alpha=1}^{N_\mathrm{s}} h_\alpha \rho D_\alpha \frac{\partial Y_\alpha}{\partial x_i} + \sum_{\alpha=1}^{N_\mathrm{s}} h_\alpha \frac{\lambda}{c_\mathrm{p}} \frac{\partial Y_\alpha}{\partial x_i} \tag{3.1.11}$$

The heat conductivity can be expressed by the viscosity and a constant Prandtl number $\lambda/c_\mathrm{p} = \mu/Pr$. Considering equation 3.1.7, the enthalpy flux term can be simplified as follows [57, 41].

$$q_i = \frac{\mu}{Pr} \frac{\partial h}{\partial x_i} - \left(\frac{\mu}{Pr} - \frac{\mu}{Sc} \right) \sum_{\alpha=1}^{N_\mathrm{s}} h_\alpha \frac{\partial Y_\alpha}{\partial x_i} \tag{3.1.12}$$

For equal Prandtl and Schmidt numbers $Pr = Sc$ the energy flux can be written as

$$q_i = \frac{\mu}{Pr} \frac{\partial h}{\partial x_i}. \tag{3.1.13}$$

Additional Relations For ideal gases the enthaply h_α and the specific heat capacity $c_{\mathrm{p},\alpha}$ depend only on temperature. They can be provided by temperature dependent polynomial fits [107, 30, 41]. The mixture properties are given by the mass-weighted sum of the specific properties.

$$h = \sum_{\alpha=1}^{N_\mathrm{s}} Y_\alpha h_\alpha \qquad \text{and} \qquad c_\mathrm{p} = \sum_{\alpha=1}^{N_\mathrm{s}} Y_\alpha c_{\mathrm{p},\alpha} \tag{3.1.14}$$

Furthermore, the conservation equations the thermal equation of state is needed to relate the thermodynamic quantities. Ideal gas is assumed in this work.

$$\frac{p}{\rho} = \frac{RT}{M}. \tag{3.1.15}$$

$$M = \left(\sum_{\alpha=1}^{N_\mathrm{s}} \frac{Y_\alpha}{M_\alpha} \right)^{-1} \tag{3.1.16}$$

3.2 Computational Models

A number of different computational models is required for an efficient numerical simulation of turbulent autoignition. Following three submodels are applied in this work and described in detail in this section.

1. Modeling of Chemical Reaction
2. Modeling of Turbulent Mixing
3. Modeling of Turbulence-Chemistry Interaction (TCI)

Furthermore, a residence time model according to Ghirelli and Leckner [59] is implemented, which provides additional insight into the flow dynamics.

3.2.1 Modeling of Chemical Reaction Rate

A modeling approach is required for the determination of the chemical source term ω_α in equation 3.1.4. The chemical reactions of N_s species can be expressed in the following general form [30, 92].

$$\sum_{\alpha=1}^{N_\mathrm{s}} \nu'_{\alpha r} \left(\frac{\rho Y_\alpha}{M_\alpha}\right) + \mathrm{TH} \rightleftharpoons \sum_{\alpha=1}^{N_\mathrm{s}} \nu''_{\alpha r} \left(\frac{\rho Y_\alpha}{M_\alpha}\right) + \mathrm{TH} \tag{3.2.1}$$

The exponents $\nu'_{\alpha r}$ and $\nu''_{\alpha r}$ are the stoichiometric coefficients of species α and reaction r. The rate of such an reaction ω_r is given by the rate coefficients $k_{\mathrm{f},r}$ and $k_{\mathrm{b},r}$ of the forward and backward reaction.

$$\omega_r = k_{\mathrm{f},r} \prod_{\alpha=1}^{N_\mathrm{s}+1} \left(\frac{\rho Y_\alpha}{M_\alpha}\right)^{\nu'_{\alpha r}} - k_{\mathrm{b},r} \prod_{\alpha=1}^{N_\mathrm{s}+1} \left(\frac{\rho Y_\alpha}{M_\alpha}\right)^{\nu''_{\alpha r}} \tag{3.2.2}$$

Some reactions require inert "third bodies", which absorb or add vibrational energy but do not take directly part in the reaction. This effect is considered by the virtual reactant TH in relation 3.2.1. Its concentration $[\,\mathrm{TH}\,]$ is given by the sum of all species concentrations times their collision efficiency t_b [30, 92].

In equation 3.2.2 the virtual reactant is considered as an artificial gas component $N_\mathrm{s}+1$ with the concentration

$$[\mathrm{TH}] = \sum_{\alpha=1}^{N_\mathrm{s}} \left(\frac{\rho Y_\alpha}{M_\alpha}\right) t_{\mathrm{b},\alpha}. \tag{3.2.3}$$

The reaction rate coefficients for the forward reactions are given by the Arrhenius expression [169, 57].

$$k = A T^\beta exp\left(-\frac{E_\mathrm{a}}{RT}\right) \tag{3.2.4}$$

The three rate coefficients, the pre-exponential constant A, the temperature exponent β and the activation energy E_a are provided by chemical reaction mechanisms. It should be emphasized here, that these coefficients are empirical values and can introduce significant uncertainties as shown in sections 5.1 and 6.2.5.

The constants for the backward reaction k_b are usually not given in mechanisms. They are determined from the chemical equilibrium. The equilibrium constant K_C is given by

$$K_{\mathrm{C}} = \frac{k_{\mathrm{f}}}{k_{\mathrm{b}}} = \left(\frac{p}{RT}\right)^{\Delta\nu} exp\left(-\sum_{\alpha=1}^{N_{\mathrm{s}}+1}\left(\nu''_{\alpha}-\nu'_{\alpha}\right)\left(H^{0}_{\alpha}-TS^{0}_{\alpha}\right)\right). \tag{3.2.5}$$

Molar enthalpy and molar entropy at standard pressure are given by polynomial fits as function of temperature. The exponent $\Delta\nu$ is defined as

$$\Delta\nu = \sum_{\alpha=1}^{N_{\mathrm{s}}}\nu''_{\alpha} - \sum_{\alpha=1}^{N_{\mathrm{s}}}\nu'_{\alpha}. \tag{3.2.6}$$

Finally the chemical source term ω_{α} of a species α is derived as sum over all N_{r} reactions in the mechanism [30, 57].

$$\omega_{\alpha} = M_{\alpha}\sum_{r=1}^{N_{\mathrm{r}}}\left(\nu''_{\alpha r}-\nu'_{\alpha r}\right)\omega_{r} \tag{3.2.7}$$

3.2.2 Modeling of Turbulent Mixing

The above given conservation equations are accurate and suffice to describe a turbulent flow. The method, where these equations are solved directly is called "Direct Numerical Simulation (DNS)". However, the spatial and temporal scales of turbulent flows span a wide range. A relation of the largest to the smallest scales can be expressed by the Reynolds number.

$$Re = \frac{\rho u L}{\mu} \tag{3.2.8}$$

The Reynolds number Re depends on the dimension of the flow geometry L (e.g. pipe diameter) and the mean flow velocity u. When the Reynolds number increases, the smallest scales decrease and a higher grid resolution is required to resolve the turbulent flow completely. Turbulent flows in gas turbine engines are characterized by high Reynolds numbers. The resolution and therewith the number of volumes, which would be required to capture the smallest scales exceeds the current computational capacities. Therefore a direct simulation of technically relevant flows for gas turbine applications is not feasible. In the following paragraphs, different methods are described to calculate turbulent flows on coarser meshes with a smaller amount of computational volumes. The most prevalent method for the simulation of technically-relevant applications is the Reynolds-averaged Navier-Stokes (RANS) simulation. It is based on the statistical averaging of the conservation equations. A more accurate but also more expensive method is the Large-Eddy Simulation (LES). The largest turbulent structures are directly resolved and smaller scales are modeled similar to the RANS approach. Due to its expenditure, LES can only be applied to semi-technical flows at low

to intermediate Reynolds numbers. It is only of limited use for the design of industrial devices due to its high computational effort. Finally, a third, hybrid LES/RANS model is also applied in this thesis.

3.2.2.1 Reynolds-Averaged Navier-Stokes (RANS)

For most technical applications it is sufficient to know the average flow properties. Therefore, the conservation equations can be statistically averaged. The respective equations are shown below [170, 57].
A flow variable Φ is split into an averaged $\overline{\Phi}$ and a fluctuating part Φ'.

$$\Phi = \overline{\Phi} + \Phi' \tag{3.2.9}$$

The following relations are valid for RANS averaging: $\overline{\overline{\Phi}} = \overline{\Phi}$ and $\overline{\Phi'} = 0$. Since large density changes can occur in combustion, a density-weighted average $\widetilde{\Phi}$, called Favre average, is applied for the flow quantities, such as velocities, species and enthalpy. It is defined such that the average of the product of the fluctuating part with density vanishes.

$$\overline{\rho\Phi''} = 0 \tag{3.2.10}$$

The Favre averaged variable $\widetilde{\Phi}$ can then be derived by following equation:

$$\widetilde{\Phi} = \frac{\overline{\rho\Phi}}{\overline{\rho}}. \tag{3.2.11}$$

In so called unsteady RANS (URANS), the average is defined as an ensemble average and is solved time-dependent. This can be of advantage for some specific applications, where periodic flow phenomena are present.
The averaged conservation equations have the following form [57].

$$\frac{\partial \overline{\rho}}{\partial t} + \frac{\partial \left(\overline{\rho}\widetilde{u_i}\right)}{\partial x_i} = 0 \tag{3.2.12}$$

$$\frac{\partial \left(\overline{\rho}\widetilde{u_i}\right)}{\partial t} + \frac{\partial \left(\overline{\rho}\widetilde{u_i}\widetilde{u_j}\right)}{\partial x_j} = -\frac{\partial \overline{p}}{\partial x_i} + \frac{\partial \overline{\tau_{ij}}}{\partial x_j} + \frac{\partial \overline{\tau_{\mathrm{t},ij}}}{\partial x_j} \tag{3.2.13}$$

$$\frac{\partial \left(\overline{\rho}\widetilde{Y_\alpha}\right)}{\partial t} + \frac{\partial \left(\overline{\rho}\widetilde{u_i}\widetilde{Y_\alpha}\right)}{\partial x_i} = \frac{\partial \overline{j_{\alpha i}}}{\partial x_i} + \frac{\partial \overline{j_{\mathrm{t},\alpha i}}}{\partial x_i} + \overline{\omega_\alpha} \tag{3.2.14}$$

$$\frac{\partial}{\partial t}\left(\overline{\rho}\widetilde{h}\right) + \frac{\partial \left(\overline{\rho}\widetilde{u_i}\widetilde{h}\right)}{\partial x_i} = \frac{\partial \overline{q_i}}{\partial x_i} + \frac{\partial \overline{q_{\mathrm{t},i}}}{\partial x_i} \tag{3.2.15}$$

Compared to the instantaneous equations, additional terms occur in the averaged equations. These are unknown and must be modeled.

$$\overline{\tau_{\mathrm{t},ij}} = -\overline{\rho}\widetilde{u_i'' u_j''} \tag{3.2.16}$$

Similar correlations appear in the scalar equations for species mass and enthalpy.

$$\overline{j_{\mathrm{t},\alpha i}} = -\overline{\rho}\widetilde{u_i'' Y_\alpha''} \tag{3.2.17}$$

$$\overline{q_{\mathrm{t},i}} = -\overline{\rho}\widetilde{u_i'' h''} \tag{3.2.18}$$

Furthermore, an additional model is required to determine the mean chemical source term $\overline{\omega_\alpha}$. In this work, a joint multi-variate assumed probability density function (APDF) approach [56, 57] is applied, which is described in section 3.2.3.

The turbulent stress tensor $\overline{\tau_{\mathrm{t},ij}}$ in equation 3.2.13 describes the correlation of the velocity fluctuations. A common closure approach is the eddy viscosity model. It is assumed that the turbulent stresses can be modeled similar to the viscous stress tensor τ_{ij} as function of the mean velocity gradients and a proportionality factor μ_t (cp. eq. 3.1.3).

For an incompressible flow, the Reynolds stress tensor can be written as follows.

$$\overline{\tau_{\mathrm{t},ij}} = -\overline{\rho}\widetilde{u_i'' u_j''} \approx \mu_\mathrm{t}\left(\frac{\partial \widetilde{u_i}}{\partial x_j} + \frac{\partial \widetilde{u_j}}{\partial x_i}\right) - 2\overline{\rho} k \delta_{ij} \tag{3.2.19}$$

Different models can be found in literature for the determination of the turbulent viscosity μ_t. In the present work, the two-equation Shear Stress Transport (SST) model by Menter [114] is applied. Two additional partial differential equations are solved for the turbulent kinetic energy k and the inverse time scale ω. The SST model combines advantages of the Wilcox k-ω turbulence model [170] in the proximity to walls (especially for flow seperation under adverse pressure gradients) with the standard k-ε model [78] in the mean flow by an automatic blending function. In the present work, the SST model is applied according to the version from 2003 [113].

$$k = \widetilde{u_i'' u_i''} \quad \text{and} \quad \omega = \beta^* \frac{\varepsilon}{k} \quad \text{with} \quad \beta^* = 0.09 \tag{3.2.20}$$

The turbulent viscosity μ_t can be described as function of k and ω.

$$\mu_\mathrm{t} = \min\left(\overline{\rho}\frac{k}{\omega}, \overline{\rho}\frac{a_1 k}{F_2 S}\right) \quad \text{with} \quad a_1 = 0.31 \tag{3.2.21}$$

The switch between the k-ε and k-ω models is given by two blending functions F_1 and F_2.

These depend on the distance to the nearest wall y and on flow variables.

F_2 is defined by:

$$F_2 = \tanh\left[\left[\max\left(\frac{2\sqrt{k}}{\beta^*\omega y}, \frac{500\mu}{y^2\omega\overline{\rho}}\right)\right]^2\right]. \tag{3.2.22}$$

The strain rate S is given by the mean velocity gradients.

$$S = \sqrt{2S_{ij}S_{ij}} \quad \text{with} \quad S_{ij} = \frac{1}{2}\left(\frac{\partial\widetilde{u_i}}{\partial x_j} + \frac{\partial\widetilde{u_j}}{\partial x_i}\right) \tag{3.2.23}$$

The two transport equation for k and ω are derived from the Navier-Stokes equations.

$$\frac{\partial(\overline{\rho}k)}{\partial t} + u_j\frac{\partial(\overline{\rho}k)}{\partial x_j} - \frac{\partial}{\partial x_j}\left[(\mu + \sigma_{\mathrm{k}}\mu_{\mathrm{t}})\frac{\partial k}{\partial x_j}\right] = P_{\mathrm{k}} - \beta^*\overline{\rho}k\omega \tag{3.2.24}$$

$$\frac{\partial(\overline{\rho}\omega)}{\partial t} + \widetilde{u_j}\frac{\partial(\overline{\rho}\omega)}{\partial x_j} - \frac{\partial}{\partial x_j}\left[(\mu + \sigma_\omega\mu_{\mathrm{t}})\frac{\partial\omega}{\partial x_j}\right] = \gamma\frac{\overline{\rho}}{\mu_{\mathrm{t}}}P_{\mathrm{k}} - \beta\overline{\rho}\omega^2 + 2(1-F_1)\overline{\rho}\sigma_{\omega 2}\frac{1}{\omega}\frac{\partial k}{\partial x_j}\frac{\partial\omega}{\partial x_j} \tag{3.2.25}$$

F_1 is the second blending function.

$$F_1 = \tanh\left\{\left\{\min\left[\max\left(\frac{\sqrt{k}}{\beta^*\omega y}, \frac{500\nu}{y^2\omega}\right), \frac{4\overline{\rho}\sigma_{\omega 2}k}{CD_{\mathrm{k}\omega}y^2}\right]\right\}^4\right\} \tag{3.2.26}$$

$$CD_{\mathrm{k}\omega} = 2\overline{\rho}\sigma_{\omega 2}\frac{1}{\omega}\frac{\partial k}{\partial x_j}\frac{\partial\omega}{\partial x_j} \tag{3.2.27}$$

The production term P_{k} is a function of the velocity gradients and the turbulent viscosity.

$$P_{\mathrm{k}} = \mu_{\mathrm{t}}\frac{\partial\widetilde{u_j}}{\partial x_i}\left(\frac{\partial\widetilde{u_j}}{\partial x_i} + \frac{\partial\widetilde{u_i}}{\partial x_j}\right) \tag{3.2.28}$$

The constants γ, β, σ_{k} and σ_ω are calculated as a blend from the corresponding constants of the k-ω (1) and k-ε (2) models.

$$\Phi = F_1\Phi_1 + (1 - F_1)\Phi_2 \tag{3.2.29}$$

The constants for this model are set according to Menter [113].

$$\begin{aligned}\gamma_1 = 5/9, \beta_1 = 0.075, \sigma_{\mathrm{k}1} = 0.85, \sigma_{\omega 1} = 0.5,\\ \gamma_2 = 0.44, \beta_2 = 0.828, \sigma_{\mathrm{k}2} = 1, \sigma_{\omega 2} = 0.856\end{aligned} \tag{3.2.30}$$

The eddy viscosity hypothesis is based on the assumption that the turbulence viscosity is isotropic. But larger uncertainties must be assumed for anisotropic, strongly 3-dimensional flow structures with complex strain fields and recirculating flows [23, 75].

Turbulent Scalar Fluxes The turbulent scalar fluxes of species mass $j_{\mathrm{t},\alpha i}$ and enthalpy $q_{\mathrm{t},i}$ in equations 3.2.14 and 3.2.15 can be modeled in analogy to the Boussinesq hypothesis (eq. 3.2.19). It is assumed that the unclosed turbulent fluxes can be described similar to Fick's and Fourier's laws (eq. 3.1.6 and 3.1.9) by the gradient of the scalar and a diffusivity constant. The turbulent diffusivities are derived by the assumption that the turbulent species and heat fluxes j_{t} and q_{t} are analogous to the turbulent momentum flux τ_{t} in equivalence to the laminar principles (3.1.7 and 3.1.13).

$$\overline{j_{\mathrm{t},\alpha i}} = -\overline{\rho}\widetilde{u_i'' Y_\alpha''} \approx \frac{\mu_{\mathrm{t}}}{Sc_{\mathrm{t}}} \frac{\partial \widetilde{Y_\alpha}}{\partial x_i} \tag{3.2.31}$$

$$\overline{q_{\mathrm{t},i}} = -\overline{\rho}\widetilde{u_i'' h''} \approx \frac{\mu_{\mathrm{t}}}{Pr_{\mathrm{t}}} \frac{\partial \widetilde{h}}{\partial x_i} \tag{3.2.32}$$

The characteristics of turbulent Schmidt and Prandtl numbers in complex jet flows for gas turbine applications was analyzed in detail by Ivanova [75]. It was found that the turbulent Schmidt numbers vary in the range between 0.5 and 0.9. Therefore, constant turbulent Schmidt and Prandtl numbers of $Sc_{\mathrm{t}} = 0.7$ and $Pr_{\mathrm{t}} = 0.7$ are applied in the present work.

3.2.2.2 Hybrid RANS/LES

In this work the hybrid RANS/LES model "Scale-Adaptive Simulation" (SAS) is applied as a comparable low-cost scale-resolving turbulence model. It was developed by Menter and Egorov [116] and is based on the SST model. The model works in cost-efficient RANS mode in steady flows and close to the walls. But in flow regions with high grid resolution and unsteady vortex shedding, a broad turbulent spectrum can be resolved (in contrast to (U)RANS methods).

An additional production term Q_{SAS} is included in the ω-equation 3.2.25.

$$Q_{\mathrm{SAS}} = \max\left[\hat{\zeta}\kappa S^2 \frac{L_{\mathrm{t}}}{L_{\mathrm{vK}}} - C\frac{2}{\sigma_\Phi} k \max\left(\frac{1}{\omega^2}\frac{\partial\omega}{\partial x_j}\frac{\partial\omega}{\partial x_j}, \frac{1}{k^2}\frac{\partial k}{\partial x_j}\frac{\partial k}{\partial x_j}\right), 0\right] \tag{3.2.33}$$

The "von Karman" length scale L_{vK} depends on the second velocity derivative, which becomes effective when large unsteady structures are resolved by the grid.

$$L_{\mathrm{vK}} = \max\left(\kappa\frac{S}{\sqrt{\frac{\partial^2\widetilde{u_i}}{\partial x_k^2}\frac{\partial^2\widetilde{u_i}}{\partial x_j^2}}}, C_{\mathrm{s}}\sqrt{\frac{\kappa\hat{\zeta}}{\beta_{\omega 2}/\beta_{\mathrm{k}}-\gamma_2}}\Delta\right) \tag{3.2.34}$$

The constants $\beta_{\omega 2}$, β_{k} and γ_2 are set according to the SST-model (eq. 3.2.30). The other constants are set as follows:

$$\hat{\zeta} = 3.52, C = 2, \kappa = 0.41, \sigma_\Phi = 2/3 \text{ and } C_{\mathrm{s}} = 0.145. \tag{3.2.35}$$

3.2.2.3 Large-Eddy Simulation

Statistical Description Another concept for the statistical description of turbulent flows is the spatially filtering approach. Here, a spatial filter G is applied to Φ. Similar to the RANS approach, Φ is split into a filtered part $\overline{\Phi}$ and a fluctuation part Φ'. However, in contrast to RANS, both parts are a function of time. The filtered variable Φ is defined by a convolution with a spatial filter function G [141, 51].

$$\overline{\Phi}(x) = \int_{\Delta} G(x-x')\,\Phi(x')\,dx' \tag{3.2.36}$$

In contrast to Reynolds-averaging, the filtered variables have following properties: $\overline{\overline{\Phi}} \neq \overline{\Phi}$ and $\overline{\Phi'} \neq 0$. In this work, the Favre averaging according to equation 3.2.11, is also applied for the spatially filtered quantities. The filter width is usually similar to the grid size Δ. The filtered Navier-Stokes equations are similar to the RANS equations. But the unclosed turbulent flux $\tau_{\mathrm{t},ij}$ describes only the influence of the unresolved turbulent scales. It is therefore called residual or subgrid scale (sgs) stress tensor. In the LES context the tilde denotes the filtered values.

$$\overline{\tau_{\mathrm{t},ij}} = \overline{\tau_{\mathrm{sgs},ij}} = -\overline{\rho}\left(\widetilde{u_i''u_j''} - \widetilde{u}_i\widetilde{u}_j\right) \tag{3.2.37}$$

The same holds for the scalar turbulent fluxes.

$$\overline{j_{\mathrm{t},\alpha i}} = \overline{j_{\mathrm{sgs},\alpha i}} = -\overline{\rho}\left(\widetilde{u_i''Y_\alpha''} - \widetilde{u}_i\widetilde{Y_\alpha}\right) \quad \text{and} \quad \overline{q_{\mathrm{t},i}} = \overline{q_{\mathrm{sgs},i}} = -\overline{\rho}\left(\widetilde{u_i''h''} - \widetilde{u}_i\widetilde{h}\right) \tag{3.2.38}$$

Turbulent Stresses The turbulent subgrid stress tensor $\overline{\tau_{\mathrm{sgs},ij}}$ is also modeled by the Boussinesq hypothesis [16, 51], similar to RANS.

$$\overline{\tau_{\mathrm{sgs},ij}} = -\overline{\rho}\left(\widetilde{u_i'' u_j''} - \widetilde{u}_i\widetilde{u}_j\right) = \mu_t\left(\frac{\partial \widetilde{u}_i}{\partial x_j} + \frac{\partial \widetilde{u}_j}{\partial x_i}\right) - 2\overline{\rho}k_{\mathrm{sgs}}\delta_{ij} \tag{3.2.39}$$

LES models are in general simpler compared to RANS models, since only the unresolved scales need to be modeled. In the present work the Wall-Adapting Local Eddy-Viscosity (WALE) model by Ducros et al. [32] is chosen as LES subgrid model. In contrast to other subgrid turbulence models, the WALE model gives reliable behavior close to walls without requiring additional damping functions.

$$\mu_t = \overline{\rho}\left(\Delta C_{\mathrm{w}}\right)^2 \frac{\left(S_{ij}^{\mathrm{d}} S_{ij}^{\mathrm{d}}\right)^{3/2}}{\left(\widetilde{S}_{ij}\widetilde{S}_{ij}\right)^{5/2} + \left(S_{ij}^{\mathrm{d}} S_{ij}^{\mathrm{d}}\right)^{5/4}} \tag{3.2.40}$$

$$S_{ij}^{\mathrm{d}} = \frac{1}{2}\left(\frac{\partial \widetilde{u}_i}{\partial x_k}\frac{\partial \widetilde{u}_k}{\partial x_j} + \frac{\partial \widetilde{u}_j}{\partial x_k}\frac{\partial \widetilde{u}_k}{\partial x_i}\right) - \frac{1}{3}\delta_{ij}\left(\frac{\partial \widetilde{u}_k}{\partial x_k}\right)^2 \tag{3.2.41}$$

The default WALE coefficient C_{w} is 0.325 for wall-bounded turbulence [131].

Turbulent Scalar Fluxes The turbulent scalar subgrid fluxes of species mass $\overline{j_{\mathrm{sgs}}}$ and enthalpy $\overline{q_{\mathrm{sgs}}}$ are also solved by the analogy assumption with the turbulent stresses as shown in equation 3.2.32.

$$\overline{j_{\mathrm{sgs},\alpha i}} = -\overline{\rho}\left(\widetilde{u_i'' Y_\alpha''} - \widetilde{u}_i\widetilde{Y_\alpha}\right) \approx \frac{\mu_{\mathrm{sgs}}}{Sc_{\mathrm{t}}}\frac{\partial \widetilde{Y_\alpha}}{\partial x_i} \tag{3.2.42}$$

$$\overline{q_{\mathrm{sgs},i}} = -\overline{\rho}\left(\widetilde{u_i'' h''} - \widetilde{u}_i\widetilde{h}\right) \approx \frac{\mu_{\mathrm{sgs}}}{Pr_{\mathrm{t}}}\frac{\partial \widetilde{h}}{\partial x_i} \tag{3.2.43}$$

3.2.3 Modeling of Turbulence-Chemistry-Interaction (TCI)

The approach to model the linear chemical source term ω_α is described in section 3.2.1. In turbulent flows, the averaged or filtered chemical source term $\overline{\omega_\alpha}$ (cp. eq. 3.2.14) must be determined [169].

$$\overline{\omega_\alpha} = M_\alpha \sum_{r=1}^{N_{\mathrm{r}}} \left(\nu_{\alpha r}'' - \nu_{\alpha r}'\right)\overline{\omega_r} \tag{3.2.44}$$

If laminar chemistry is assumed, such that $\overline{\omega_{\mathrm{r}}} = \mathrm{f}(\widetilde{T}, \widetilde{Y_\alpha})$, considerable inaccuracies might be introduced due to the strong non-linear dependence of the chemical source term on temperature and species. Therefore, a turbulence-chemistry interaction (TCI) model is required to

account for the unresolved fluctuations. A multi-variate assumed probalility-density function (PDF) approach is used in the present work. A detailed derivation can be found in Gerlinger [56, 57] and Di Domenico [30].
The advantage of the assumed PDF model is that only two additional transport equations for the temperature and the sum of the species variances (σ_T and σ_Y) must be solved.

$$\sigma_\mathrm{T} = \widetilde{T''^2} \qquad \text{and} \qquad \sigma_\mathrm{Y} = \sum_{\alpha=1}^{N_\mathrm{s}} \widetilde{Y_\alpha''^2} \tag{3.2.45}$$

$$\frac{\partial\left(\rho\sigma_\mathrm{T}\right)}{\partial t} + \frac{\partial\left(\rho u_i \sigma_\mathrm{T}\right)}{\partial x_i} = \frac{\partial}{\partial x_i}\left(\frac{\mu_\mathrm{t}}{Pr_\mathrm{t}}\frac{\partial\sigma_\mathrm{T}}{\partial x_i}\right) + 2\frac{\mu_\mathrm{t}}{Pr_\mathrm{t}}\left(\frac{\partial\widetilde{T}}{\partial x_i}\right)^2 - C_\mathrm{T}\frac{\overline{\rho}\sigma_\mathrm{T}}{\tau_\mathrm{t}} \tag{3.2.46}$$

$$\frac{\partial\left(\rho\sigma_\mathrm{Y}\right)}{\partial t} + \frac{\partial\left(\rho u_i \sigma_\mathrm{Y}\right)}{\partial x_i} = \frac{\partial}{\partial x_i}\left(\frac{\mu_\mathrm{t}}{Sc_\mathrm{t}}\frac{\partial\sigma_\mathrm{Y}}{\partial x_i}\right) + 2\sum_{\alpha=1}^{N_\mathrm{s}}\overline{\rho}\frac{\mu_\mathrm{t}}{Sc_\mathrm{t}}\left(\frac{\partial\widetilde{Y_\alpha}}{\partial x_i}\right)^2 - C_\mathrm{Y}\frac{\overline{\rho}\sigma_\mathrm{Y}}{\tau_\mathrm{t}} \tag{3.2.47}$$

The diffusion coefficients correspond to the turbulent Prandtl and Schmidt number. The dimensionless dissipation constants are set to $C_\mathrm{T} = 1$ and $C_\mathrm{Y} = 2$. τ_t is the turbulent time scale. The shapes of the assumed probability density functions are defined by the Favre averaged means ($\widetilde{T}$, $\widetilde{Y_\alpha}$) and the corresponding variances (σ_T, σ_Y). A clipped Gaussian shape is used as temperature distribution (eq. 3.2.48) [58, 30].

$$P\left(\hat{T}\right) = \frac{1}{\sqrt{2\pi\sigma_0}} exp\left[-\frac{\left(\hat{T}-\widetilde{T}_0\right)^2}{2\sigma_0}\right] + A_1\delta\left(\hat{T}-\widetilde{T}_\mathrm{min}\right) + A_2\delta\left(\hat{T}-\widetilde{T}_\mathrm{max}\right) \tag{3.2.48}$$

To avoid any physically impossible temperature ranges, the PDF is limited to the minimal ambient temperature T_min and the adiabatic flame temperature T_max. Additional Dirac pulses δ are employed at bounds. They have the size of the clipped areas A_1 and A_2. The parameters T_0 and σ_0 are defined such that the correct values for $\widetilde{T}$ and σ_T are obtained and that the normalization property of the PDF is ensured.
For the species a multi-dimensional beta-PDF is used, which is given by the following expression [58, 30].

$$P\left(\hat{\mathbf{Y}}\right) = \frac{\Gamma\left(\sum_{\alpha=1}^{N_\mathrm{s}}\beta_\alpha\right)}{\prod_{\alpha=1}^{N_\mathrm{s}}\Gamma(\beta_\alpha)}\delta\left(1-\sum_{\alpha=1}^{N_\mathrm{s}}\hat{Y}_\alpha\right)\prod_{\alpha=1}^{N_\mathrm{s}}\hat{Y}_\alpha^{\beta_\alpha-1} \tag{3.2.49}$$

with

$$\hat{\mathbf{Y}} = \left(\hat{Y}_1, \hat{Y}_2, ..., \hat{Y}_{N_\mathrm{s}}\right)^T \tag{3.2.50}$$

$$\beta_\alpha = \widetilde{Y_\alpha} B \qquad \text{and} \qquad B = \frac{\sum_{\alpha=1}^{N_\mathrm{s}} \widetilde{Y_\alpha}(1-\widetilde{Y_\alpha})}{\sigma_\mathrm{Y}} - 1 \tag{3.2.51}$$

The species PDF is defined by the species means $\widetilde{Y_\alpha}$ and just one single variance quantity, the turbulent scalar energy σ_Y. This multi-variate β-PDF approach was developed by Girimaji [60]. It has the advantage that only one additional transport equation must be solved. The drawback is that the mass fraction variances and covariances are no longer independent. Finally, the averaged reaction rates $\overline{\omega_r}$ can be derived from the probability density functions. With assumption of statistical independence of temperature and gas composition, the following relation is employed [56, 30].

$$\overline{\omega_r} = \overline{k_{\mathrm{f},r}} \overline{\prod_{\alpha=1}^{N_\mathrm{s}+1} \left(\frac{\overline{\rho}\widetilde{Y_\alpha}}{M_\alpha} \right)^{\nu'_{\alpha r}}} - \overline{k_{\mathrm{b},r}} \overline{\prod_{\alpha=1}^{N_\mathrm{s}+1} \left(\frac{\overline{\rho}\widetilde{Y_\alpha}}{M_\alpha} \right)^{\nu''_{\alpha r}}} \tag{3.2.52}$$

The individual terms can be assessed by integration along the probability density functions [58].

$$\overline{k_r} = \int_{\hat{T}=T_\mathrm{min}}^{\hat{T}=T_\mathrm{max}} k_r\left(\hat{T}\right) P\left(\hat{T}\right) d\hat{T} \tag{3.2.53}$$

$$\overline{\prod_{\alpha=1}^{N_\mathrm{s}+1} \left(\frac{\overline{\rho}\widetilde{Y_\alpha}}{M_\alpha} \right)^{\nu'_{\alpha r}}} = \int_{\hat{\mathbf{Y}}} \left[\prod_{\alpha=1}^{N_\mathrm{s}+1} \left(\frac{\overline{\rho}\widetilde{Y_\alpha}}{M_\alpha} \right)^{\nu'_{\alpha r}} \right] P\left(\hat{\mathbf{Y}}\right) d\hat{\mathbf{Y}} \tag{3.2.54}$$

To reduce the cost of the numerical simulations, the resulting expressions are calculated in advance and stored in look-up tables.

3.2.4 Residence Time

Revealing insight into the time-dependent evolution of autoignition can be gained by assessment of the local residence time. The residence time model, which is applied in the present work, is based on the work by Ghirelli and Leckner [59] and holds for turbulent transient flows with density changes. The local residence time is defined as the time that a fuel particle has spent inside the computational domain since its inflow at the inlet boundary. It is derived by the solution of two additional transport equations for a passive scalar Γ and the so called "quantity of residence time" Q.

$$\frac{\partial\left(\overline{\rho}\widetilde{\Gamma}\right)}{\partial t} + \frac{\partial\left(\overline{\rho}\widetilde{u_i}\widetilde{\Gamma}\right)}{\partial x_i} = -\frac{\partial}{\partial x_i}\left[\left(\mu + \mu_\mathrm{t}\right) \frac{\partial \widetilde{\Gamma}}{\partial x_i} \right] \tag{3.2.55}$$

$$\frac{\partial\left(\overline{\rho}\widetilde{Q}\right)}{\partial t}+\frac{\partial\left(\overline{\rho}\widetilde{u}_i\widetilde{Q}\right)}{\partial x_i}=-\frac{\partial}{\partial x_i}\left[\left(\mu+\mu_{\mathrm{t}}\right)\frac{\partial\widetilde{Q}}{\partial x_i}\right]+\widetilde{\Gamma}\overline{\rho} \tag{3.2.56}$$

The last term in equation 3.2.56 is the production term of Q. The quantity of residence time increases by one unit residence time per unit elapsed time. The diffusive fluxes are modeled by the gradient-diffusion hypothesis and unity Schmidt numbers. The passive scalar Γ is set to one at the fuel inflow boundary and zero in the coflow. The residence time quantity Q is zero at both inlets. Finally, the local residence time τ_{res} equates to the ratio of the two transported quantities.

$$\widetilde{\tau_{\mathrm{res}}}=\frac{\widetilde{Q}}{\widetilde{\Gamma}} \tag{3.2.57}$$

4 Validation Methodology

This chapter deals with the review of validation methodologies and uncertainty quantification in computational modeling. This topic has recently gained increasing interest in industry and academia. The ASME published a "Standard for Verification and Validation (V&V) in CFD and Heat Transfer" in 2009 [3] and holds a V&V symposium since 2012. Also the "Society for Industrial and Applied Mathematics" introduced a new conference and a journal on uncertainty quantification in 2012. The increased reliance on numerical simulation for the industrial development processes also raised the demand for standardized validation processes and quantitative estimates of the modeling accuracy.

4.1 Fundamentals

An overview of the terminology and validation techniques is presented in this section.

Terminology/ Definition

The following definition is given in the "AIAA Verification and Validation Guide for CFD":

> *"[Validation is] the process of determining the degree to which a model is an accurate representation of the real world from the perspective of the* ***intended use of the model****. [...] The estimation of a range within which the simulation modeling error lies is a primary objective of the validation process and is accomplished by comparing a simulation results (solution) with an appropriate experimental result (data) for* ***specified validation variables*** *under a* ***specified set of conditions.****"* [2]

> *"****There can be no validation without experimental data with which to compare the results of the simulation.****"* [2]

A similar description of the term "Validation" is given in a Sandia report by Oberkampf:

> *"Validation of a model or code cannot be mathematically proven; validation can only be assessed* ***for individual realizations*** *of nature."* [134]

It is important to distinguish between "Validation" and "Verification". As stated in the "AIAA Verification and Validation Guide for CFD" : *"validation must be preceded by code verification and solution verification. Code verification establishes that the code accurately solves the mathematical model incorporated in the code. Solution verification estimates the numerical accuracy of a particular calculation"* [2]. Verification can be conducted by comparison with analytical solutions.
Many traditional validation approaches aim to decide whether a computational model is right or wrong in general. However, the above-quoted definitions state, that a model validation can only provide information about the accuracy of a model under the specific conditions of the reference test case. Furthermore, it is emphasized that the validation should be conducted with respect to the intended use of the model.

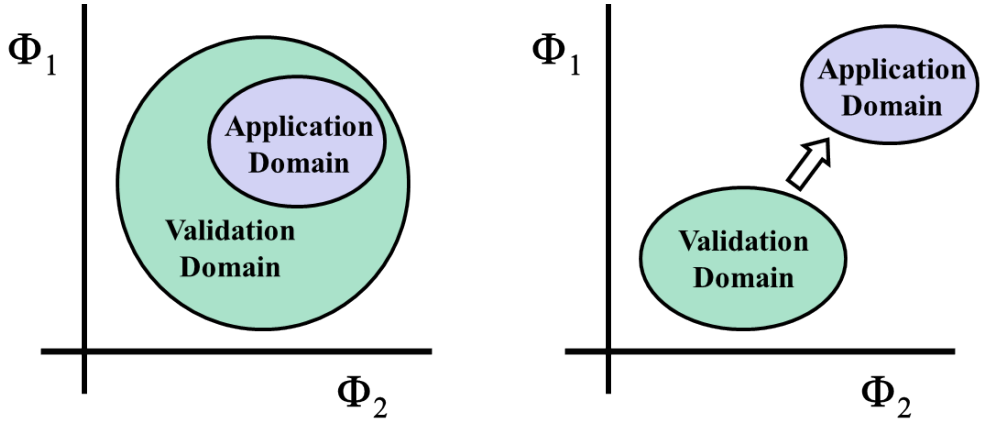

Figure 4.1.1: Relation between validation domain and application domain [134]

In figure 4.1.1 the validation domain represents the range of conditions (Φ_1 and Φ_2) at which the validation has been conducted. The application domain comprises the conditions of the intended use of the model. In the left figure, the model has been validated under the relevant operating conditions. It can be assumed that the same physical phenomena and properties prevail, when the model is applied in the design process.
However, in the right figure, the physical conditions differ for validation and application. This also means that different physical phenomena might exist under these conditions, such as different chemical pathways or deviating turbulence-chemistry characteristics, which were not considered during the design and validation of the model.
If the discrepancy between test conditions and the application of interest is large, the credibility of the model is questionable. Therefore a validation should be conducted as close to the actual operating conditions as possible and the application of interest should be defined

carefully prior to the validation process [133]. The description of the application of interest should include a description of the system (e.g. geometry, boundary and inflow conditions, physical parameters) as well as relevant scenarios and system response quantities.
Often, the behavior of an engineering system can be described by numerous quantities. Usually not all quantities are of interest for the intended use of the model. Prior to the validation process, a set of relevant "system response quantities" (SRQ) [133, 156] should be defined, which reflect the main objective of the system [168]. In many systems, the system response quantities are a direct output of the system. However, in some cases the system response quantities must be derived by transformations [156].

Uncertainty Quantification and Validation Metric

When comparing experimental data and numerical solutions, different levels of precision can be applied (figure 4.1.2). The representation of the results is called "Validation Metric". The term is defined by Oberkampf as follows:

> *"**Validation metric:** a mathematical operator that measures the difference between a **system response quantity (SRQ)** obtained from a simulation result and one obtained from experimental measurements."* [134]

An illustrative way to present results, is the comparison of 2-dimensional contour-plots (top image in figure 4.1.2). However, very limited quantitative information can be extracted from this type of diagram. More specific information is given by the comparison of deterministic response quantities (left image). Although, no uncertainty ranges are considered in deterministic comparisons. The information content is further increased, when also experimental measurement uncertainties are included in the analysis. However, a comprehensive validation requires the quantification of errors and uncertainties in both, numerical and experimental results [3, 133].
Uncertainty quantification has gained increasing interest in recent years (s.o.). A very comprehensive overview of uncertainty quantification for turbulent combustion modeling is given by Najm [125]. An accurate estimation of modeling capabilities is of high relevance for engineering design and scientific investigations. In engineering, the quantitative estimation of modeling uncertainties is of special relevance for reliability assessment, determination of safety factors and for decision making. This is especially true for complex safety-related systems, where extensive testing is not always possible and miscalculations can have a big impact. In scientific studies, a numerical model can only be validated reliably, if quantitative uncertainties are provided for both, experimental and numerical uncertainties. Otherwise it is not possible to determine, whether any discrepancies between experimental and numerical results are due to measurement uncertainties or model deficiencies.

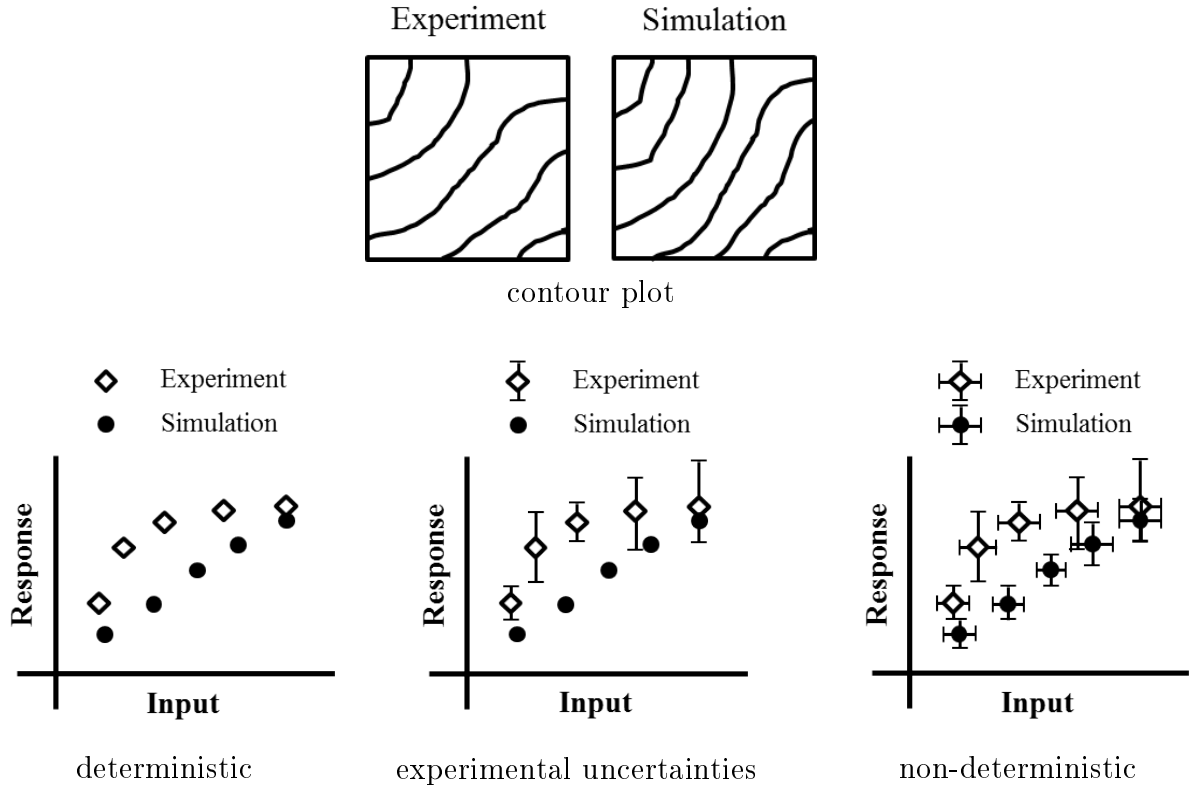

Figure 4.1.2: Increasing quality of validation metrics [134]

The potential sources of uncertainty in the numerical modeling can be divided into two types. The **"model input uncertainties"** [133] include boundary and inflow conditions, specific model parameters (e.g. turbulence modeling constants or chemical rate coefficients) and geometry specifications of the computational domain. Whereas **"model form uncertainties"** [133] arise due to deficiencies in the physical model and inappropriate model assumptions.

Validation Hierarchy

As described above, the model credibility gained through model validation does only apply to the actual test conditions (figure 4.1.1). When the model is used for different conditions than for which it has been validated, a reliable estimation of the predictive capability is not possible. However, as stated by Oberkampf, the experimental validation data, which can be gained under realistic operating conditions is usually very limited:

> *"For typical complex engineering systems (e.g., a gas turbine engine), multidisciplinary, coupled physical phenomena occur together. Data are measured on the engineering hardware under realistic operating conditions. The quantity and quality of these measurements, however, are essentially always very limited. It is difficult, and sometimes impossible, for complex systems to quantify most of the test conditions*

required for computational modeling, e.g., [...] coupled time-dependent boundary conditions." [133]

Furthermore, also in the computational modeling, significant simplifications must be accepted under technically relevant conditions due to high turbulent Reynolds numbers and increased model complexity.

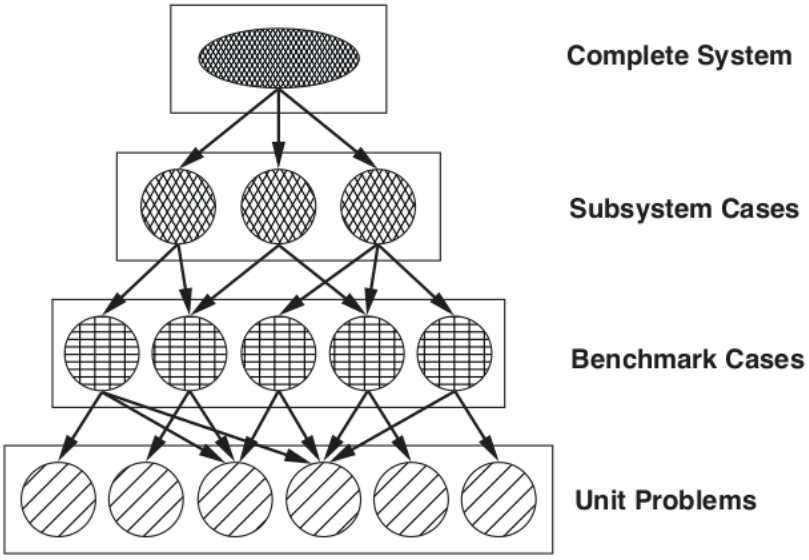

Figure 4.1.3: Validation hierarchy [133]

To overcome the experimental and numerical limitations under realistic operating conditions, a novel validation methodology by Oberkampf [133] is applied. A hierarchy of several deliberately selected experiments is build on basis of the complete technical system. The hierarchy can be divided into different levels of complexity, including subsystems, benchmark cases and unit problems. The physical complexity, such as spatial and temporal dimensionality, geometric complexity and physical process coupling is reduced from one level to the next. This way the separate submodels and submodel interactions can be validated at different levels of complexity. With decreasing complexity of the experimental test conditions a higher accuracy of the experimental reference data can be achieved. But at lower system level, the similarity with the complete system is also reduced. In contrast to the conventional approach, where computational (sub)models are validated by labscale experiments (e.g. unit and benchmark cases) and afterwards applied to test conditions, the procedure is reversed in the hierarchy approach. The design of the labscale experiments is geared to the application of interest and is defined in such a way, that it resembles the complete technical system in one or more characteristic features.

4.2 Validation under Gas Turbine Operating Conditions

As described in the previous section, the conditions of the validation test cases must be carefully defined and compared with the realistic engine conditions.

In the present validation study, autoignition modeling capabilities are assessed for gas turbine operating conditions. In specific, it is investigated how accurate premature autoignition of hydrogen-rich fuels can be predicted in the premix section of the Alstom gas turbine GT24/GT26 reheat combustor.

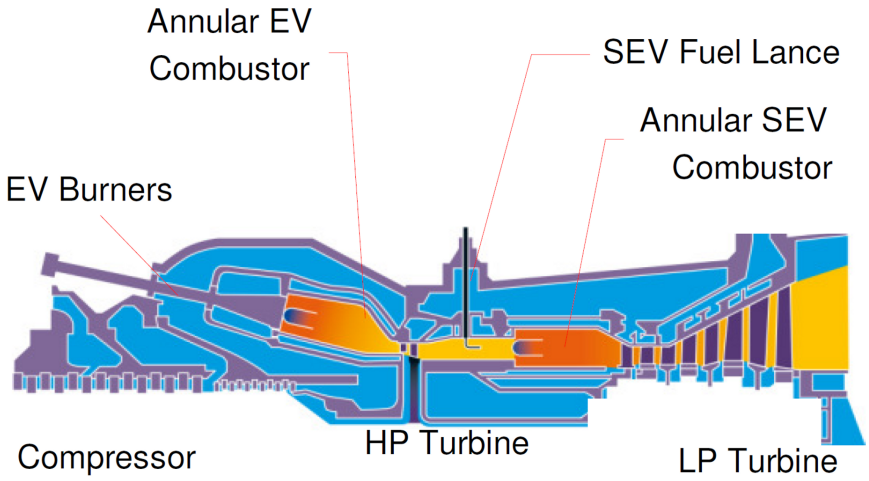

Figure 4.2.1: Scheme of the Alstom gas turbine engine GT24/GT26 [143]

4.2.1 Application of Interest

System

Premix Section of a Reheat Gas Turbine Combustor

Engine Operating Conditions

Highly Turbulent Flow
High Pressure (20 bar)
Jet-in-Crossflow Configuration for Fuel Injection
Composition: Hot Vitiated Air ($T_{cf} \approx 1300\,K$) and Hydrogen-Rich Fuel

Scenario

Autoignition (Operation Limit)

Sequential Combustion

The sequential gas turbine combustion system allows a high fuel flexibility in combination with high efficiency and low emissions. It has been realised in the GT24/GT26 by Alstom [80]. In contrast to other conventional gas turbine systems, the sequential combustion system is based on two subsequent combustion stages (figure 4.2.1). In a first combustion stage compressed air is burned in the "EV" combustor. The exhaust is then partially expanded in a high-pressure turbine. Afterwards, additional fuel is injected and mixed with the partly depressurized hot exhaust from the first stage. The mixture is burned in the secondary "SEV" reheat combustor before it is fully expanded in the low pressure turbine.

Reheat Combustor

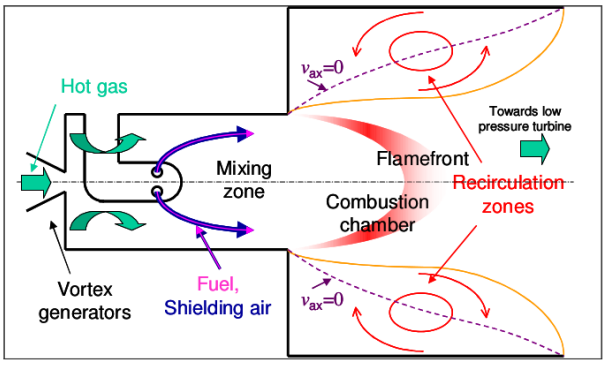

Figure 4.2.2: Schematic sketch of the reheat combustor [36]

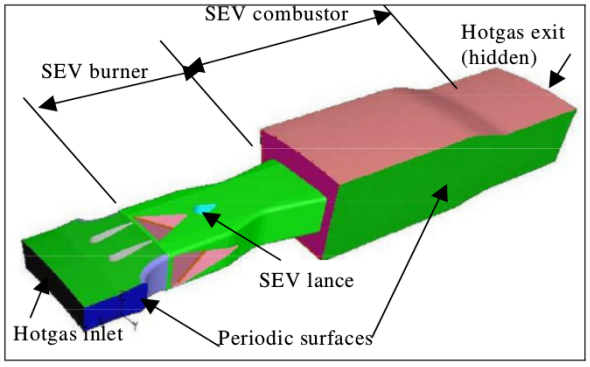

Figure 4.2.3: Geometry of the reheat combustor [36]

As described by Güthe et al. [67], the combustion process in the reheat combustor is stabilized and controlled by autoignition. The generic operation and convenient interplay of two different flame stabilization mechanisms (flame propagation in the first and autoignition in the second stage) allows a particularly high part load efficiency and wide range of fuel flexibility in combination with low emissions.

However, special attention must be paid to the design of the reheat stage. The reheat combustor is operated in lean premixed mode. The preliminary mixing of fuel and oxidizer can provide a very homogeneous combustion with small mixture and temperature variations. The elimination of temperature peaks allows for very low NO_x emissions which increase exponentially with temperature [161]. Unfortunately, the residence time, which is available for adequate mixing is limited by the ignition delay time of the combustible mixture.

The prediction of premature autoignition in the premix section of the reheat combustor is the central aspect of the present study. The premix section operates at a pressure of about 20 bar and the hot exhaust gas is characterized by temperatures of about 1300 K [143]. A scheme of the mixing section is shown in figures 4.2.2 and 4.2.3. The fuel is injected through multiple jets into a perpendicular stream of hot exhaust gas from the first combustion stage [36]. This jet-in-crossflow configuration allows for an efficient mixing of the two streams. Due to the high velocities and large combustor dimensions the flow is highly turbulent [80].

Hydrogen-Rich Fuels

Nowadays, there is a pressing environmental need to reduce the CO_2 emissions [127]. In gas turbine applications CO_2 emissions can be reduced through a reduction of the carbon fuel content. Several new technologies already exist in an advanced state of development, such as syngas fuels from gasification of coal and biomass, pre-combustion carbon-capture and storage (CCS) and the power-to-gas technology, where excessive wind power is converted into hydrogen by electrolysis. Therefore, future gas turbine systems will have to handle a large range of fuels with high hydrogen content.

These hydrogen-rich fuels have different combustion characteristics compared to conventional natural gas. Thus, for example the autoignition delay time is significantly reduced. However, premature ignition in the premix section must be avoided, since it can lead to critical damage of the combustor [93]. In the present work, a fuel mixture of up to 70 vol% hydrogen in nitrogen is applied as target fuel. It has been identified as a suitable reference fuel for an integrated gasification combined cycle (IGCC) with 90 % CO_2-capture-rate in the European Framework Project ENCAP [94].

4.2.2 Validation Hierarchy

In the present thesis, the validation hierarchy approach has been applied to the Alstom GT24/GT26 gas turbine combustion system [148, 149]. The design of validation hierarchy for the Alstom gas turbine system in figure 4.2.4 is based on the general scheme in figure 4.1.3. The complete system (top box) is more and more reduced to increasingly simpler subsystems, benchmark cases and unit problems, which are investigated in the following chapters. Each box represents one experiment and provides a short overview about the respective test case. As described above, the experiments were deliberately chosen in such a way, that they reflect one or more characteristic features of the complete technical system. These features: technical environment, physical conditions and scenarios (section 4.1) are specified in the left, blue columns. The available reference quantities for autoignition events, flow and mixture fields are provided in the the right, green column.

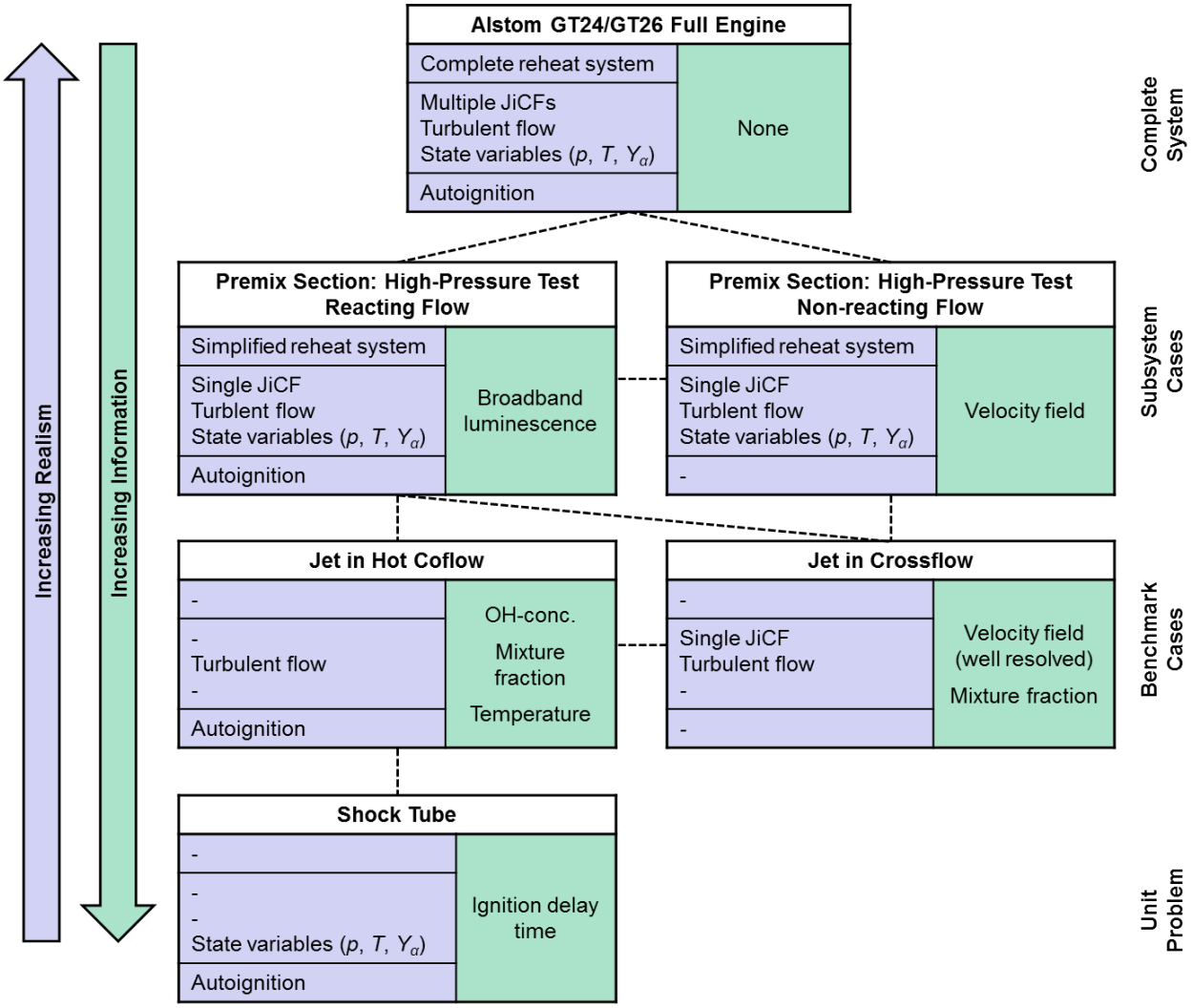

Figure 4.2.4: Experiment validation hierarchy for the premix section of the Alstom GT24/GT26 SEV combustor

Validation Experiments under Gas Turbine Conditions

The first box in figure 4.2.4 represents the full gas turbine engine. Unfortunately, there are no studies published on autoignition experiments in a real engine, since there is no optical accessibility for detailed diagnostic measurements.

However, the conditions in the SEV premix section can be resembled in high pressure lab experiments. The two subsystem experiments (second row in figure 4.2.4), which are used in the present study are based on a recent sophisticated DLR subsystem experiment, which was operated under conditions very similar to the sequential gas turbine conditions [46, 44, 45, 42]. The test section is significantly reduced in size compared to the real gas turbine, but the physical conditions are comparable. Thus, the studies were performed at a pressure of 15 bar, temperatures between 1100 K and 1250 K and flow velocities of about 200 m/s. The resulting Reynolds number $Re \approx 500'000$ - $1'000'000$ is comparable to real-engine conditions [80]. The complex gas turbine fuel injection system is simplified to a generic jet-in-crossflow configuration with a small momentum ratio $J = 2$ - 4. The mixing section is optically accessible through quartz glass windows for the laser diagnostic measurement of ignition events. The upstream and downstream entities are designed similar to the real engine to emulate proper technical boundary conditions. However, the detailed exit profiles of the turbine for temperature and velocity as well as detailed burner geometries are not incorporated.

For the present work, two different validation experiments are used from the high pressure test rig: one to analyse the autoignition processes and a second without combustion to compare the velocity fields. In the **reacting jet-in-crossflow** configuration (figure 4.2.4, 2nd row, left box), autoignition events were monitored with time-resolved measurement of the broadband luminescence. It was found that separated ignition kernels interact with the low velocity region in the jet lee and can anchor there as a stable flame within the premix section. In the **non-reacting test case** (2nd row, right box), the velocity field was investigated with particle image velocimetry (PIV).

Although, advanced measurement techniques were applied in these experiments, it is difficult to accurately quantify the boundary conditions under these challenging test conditions. Thus, for example, it was not possible to measure turbulent temperature fluctuations, which were found to have a significant impact on autoignition.

Validation Experiments under Simplified Conditions

To gain a deeper understanding of the validation results under high pressure engine conditions, three additional validation experiments were selected. This facilitates the investigation of the different submodels and their interactions. Nevertheless, the simplified and therefore more precise and reliable experiments are closely related to the application of interest.

The first selected simplified experiments are ignition delay time measurements in **shock tubes** by Keromnes at al. [86] (last box in figure 4.2.4). Only enclosed homogeneous mixtures are considered and any influence of mixing and transport processes is neglected. But this study comprises the impact of the realistic thermochemical state on the chemical process, including pressure, temperature and composition. The second simplified experiment is a **turbulent jet-in-crossflow** test case by Andreopoulos [5] (left box in 3rd row). Here, the influence of chemistry is disregarded to facilitate the validation of turbulent mixing modeling under technical relevant test conditions. This inert experiment is characterized by a high turbulence intensity at $Re = 82'000$ and a low momentum ratio ($J = 4$), which are comparable to the actual gas turbine conditions. Finally, the **jet-in-hot-coflow experiment** by Arndt et al. [8] (right box in 3rd row) is selected to analyze the turbulence-chemistry interaction. The physical phenomena of ignition onset in form of separated ignition kernels is similar to what has been observed in the application oriented subsystem experiment. But the measurements were conducted at atmospheric pressure and a more simple straight jet-in-coflow configuration ($Re = 15'000$), which provides detailed insight into the interaction of turbulent motion and chemical reaction.

5 Validation under Generic Conditions

In this chapter, the validation experiment under simplified conditions (figure 4.2.4: unit problems and benchmark cases) are analyzed. As described in the previous chapter, each test case represents a set of specific characteristics of the technical application.

5.1 Autoignition in a Homogeneous System

The first generic test case is focused solely on the chemical kinetics. In a preliminary analysis (section 5.1.1 and 5.1.3), the relevant pressure, temperatures and compositions are identified, which correspond to the real gas turbine conditions. Based on these results, an appropriate shock tube experiment is selected and several chemical reaction mechanisms are compared for the respective engine conditions. Any influence of mixture variations and transport processes are not considered in this analysis.

5.1.1 Shock Tube Experiment under GT Operating Conditions

The relevant engine operating conditions in the reheat section of sequential gas turbines are quite challenging. The fuel is injected at a pressure of about 15 bar into hot vitiated air from the first stage at temperatures in the range of $T_{\mathrm{HG}} = 1100 \text{ - } 1400\,\mathrm{K}$. In the present work, the application of hydrogen rich fuels is studied. A relevant composition of up to 70 % hydrogen in nitrogen is considered, which corresponds to 90 % carbon capture. The actual conditions for this investigation are geared to the high pressure subsystem experiment by Fleck et al. [45], which is presented in detail in chapter 6. The respective compositions for the fuel and the hot vitiated air are specified in table 5.1.

Table 5.1: Fuel and oxidizer compositions for the homogeneous reactor study (given in mole fractions)

	T [K]	X_{H2}	X_{N2}	X_{O2}	X_{H2O}	X_{CO2}
Hot vitiated air	1100 - 1400	0	0.769	0.150	0.054	0.027
Fuel	313	0.31	0.69	0	0	0

In the respective combustion experiment, ignition already occurred at hydrogen contents of about 30 %. Therefore, this value is also applied for the homogeneous reactor study.

To ensure a reliable validation at the above shown conditions, a suited reference shock tube experiment must be selected. Two important criteria must be considered. As described in section 2.3 “Turbulent Mixing Layer”, in non-premixed systems autoignition is initiated around a specific most-reactive mixture fraction. The homogeneous system must relate to the conditions around this mixture fraction. Furthermore, the validation must be conducted for the relevant chemical reaction path. In the applicable pressure and temperature range, the hydrogen fuel can ignite through two different mechanisms, which are described in detail in section 2.1 “Homogeneous Systems”. Therefore, the most-reactive mixture state and the respective ignition path are identified in a preliminary study (section 5.1.3).

5.1.2 Numerical Simulation with Homogeneous Reactor Modeling

Homogeneous reactor simulations are conducted under the experimental temperature and pressure conditions. The chemical reaction modeling tool Cantera [62] is used to conduct the studies for a zero-dimensional constant pressure reactor. It is a closed system with no inlets or outlets. Adiabatic, inert walls are assumed and the volume is variable. In the preliminary study, the reaction mechanism by Ó Conaire at al. [135] is used. The ignition delay time is determined in accordance with the shock tube measurements by the maximum OH* concentration. Therefore, the OH* submechanism by Kathortia et al. [82] is added to the hydrogen mechanisms.

5.1.3 Preliminary Analysis of GT Operating Conditions

At first, a preliminary analysis of the ignition process under gas turbine conditions is conducted to identify the location of the most-reactive mixture fraction Z_{mr}, at which the first ignition kernels will probably emerge. The baseline conditions correspond to the experiment by Fleck et al. [45] (tab. 5.1).

In figure 5.1.1 the ignition delay times are calculated for specific homogeneous mixtures, which represent different local mixture states of the non-premixed system. The calculated ignition delay times are plotted versus the initial hydrogen content of the respective mixtures. The mixture variations are conducted for three different hot gas temperatures ($T_{\mathrm{HG}} = 1173\,\mathrm{K}$, $1273\,\mathrm{K}$ and $1373\,\mathrm{K}$). The most-reactive conditions are located at lean mixtures with a hydrogen content X_{H2} of less than $2\,\%$. This corresponds to a mixture fraction of $Z = 0.05$ and an equivalence ratio of $\Phi = 0.07$. However, under very lean conditions, the heat release is very small. This is presented in figure 5.1.2. The temporal evolution of different mixtures are shown at a temperature of $1173\,\mathrm{K}$. The most-reactive mixture conditions are around a hydrogen content of $X_{\mathrm{H2}} = 0.5\,\%$ (black line in figure 5.1.1). But for this mixture (green line in figure 5.1.2), the maximum temperature increase is about $1\,\%$ (within the mixing section

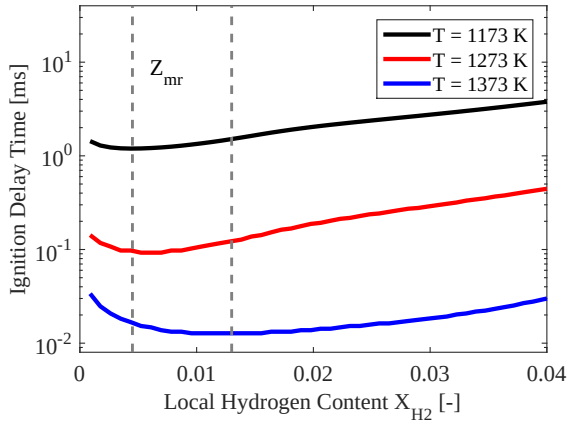

Figure 5.1.1: Ignition delay time under gas turbine operating conditions ($p = 15\,\text{bar}$)

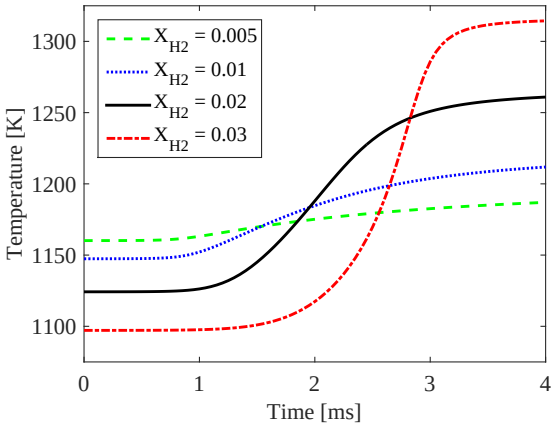

Figure 5.1.2: Temperature evolution for $T_{\text{HG}} = 1173\,\text{K}$ and $p = 15\,\text{bar}$

residence time of about 0.5 ms, chapter 6). In the CFD simulations, which are presented in chapter 6, it was found that this is not sufficient to initiate a self-sustaining ignition kernel. The relevant kernels actually emerge at slightly richer conditions of about $X_{\text{H2}} = 2\,\%$.

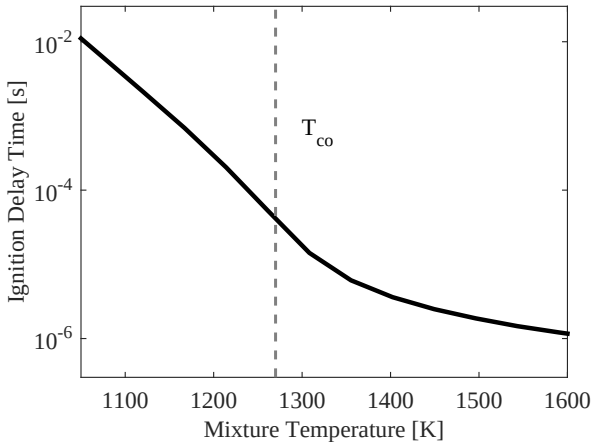

Figure 5.1.3: Temperature dependency of ignition delay time for engine operating conditions at $p = 15\,\text{bar}$ and $X_{\text{H2}} = 0.02$

For a reliable validation with appropriate reference data, it is also necessary to identify the ignition regime. The crossover conditions between the second and third ignition limit (section 2.1) can be assessed by equations 2.1.6 to 2.1.8. For a pressure of 15 bar and a relevant hydrogen mole fraction of $X_{\text{H2}} = 0.02$ the crossover temperature is $T_{\text{co}} = 1270\,\text{K}$. The temperature range of 1100 - 1400 K, which is of interest in the present work, lies in the transition region between the two ignition paths. However, in figure 5.1.2 it is apparent that

the actual local mixture temperatures for the relevant fuel-air mixtures (e.g. $X_{H2} = 0.02$) can be about to 50 K lower than the hot gas temperature. This means that the majority of relevant ignition conditions are below the crossover temperature (third limit). As described in chapter 2, above crossover, ignition proceeds mainly through the fast build-up of H-radicals and is only weakly affected by turbulence. Below this crossover temperature, ignition through H-atom build-up is inhibited and a second path through the slow build-up of HO_2 and H_2O_2 leads to ignition. In this third ignition limit, diffusive and convective transport processes can influence the ignition process significantly.
The trend of ignition delay time for 15 bar and $X_{H2} = 0.02$ is plotted over the relevant temperature range in figure 5.1.3. It is obvious that the ignition delay time grows much more rapidly in the third limit (below crossover) compared to the second limit (above crossover). Consequently, the ignition delay time is much more sensitive to temperature in the third limit. It should also be emphasized that the ignition delay time is plotted in logarithmic scale. In the third ignition limit (for temperatures up to 1270 K), the logarithm of the ignition delay depends linearly on temperature and the following relation can be deduced.

$$\log \frac{\tau_1}{\tau_2} = -0.011(T_1 - T_2) \tag{5.1.1}$$

Thus, for example, a temperature uncertainty of ± 10 K results in an ignition delay time range of ± 29 %.

5.1.4 Validation of Chemical Reaction Modeling

Based on the results of the preliminary study under gas turbine conditions, a suited shock tube experiment is selected for the validation of the chemical reaction mechanisms. In this reference experiment, the homogeneous mixtures should also be located around and below the crossover temperature (section 2.1). In a detailed literature study, only few experiments were identified which fulfill these conditions. The best suited data are DLR shock tube experiments, which were published in Kermones et al. [86]. In these experiments, the ignition delay time of lean $H_2/O_2/N_2$-mixture with an equivalence ratio of $\Phi_{local} = 0.5$ (corresponds to $X_{H2} = 0.0347$) were measured at a high pressure p between 15 to 16.5 bar and a temperature range of 1060 - 1243 K. The crossover temperature for these conditions is T_{co}=1207 K. The ignition delay times are determined by the maximum of the OH* concentration at 308 nm. The measurement uncertainty of the mixture temperature is ± 10 K. This is visualized by the horizontal error bar in figure 5.1.4.
In figure 5.1.4, four different recent chemical reaction mechanisms are compared to the experimental measurements: Ó Conaire at al. [135] from 2004, Burke et al.[17] from 2012, Konnov [89] from 2008 and Li et al. [96] from 2004. Around the crossover temperature $T_{co} = 1207$ K,

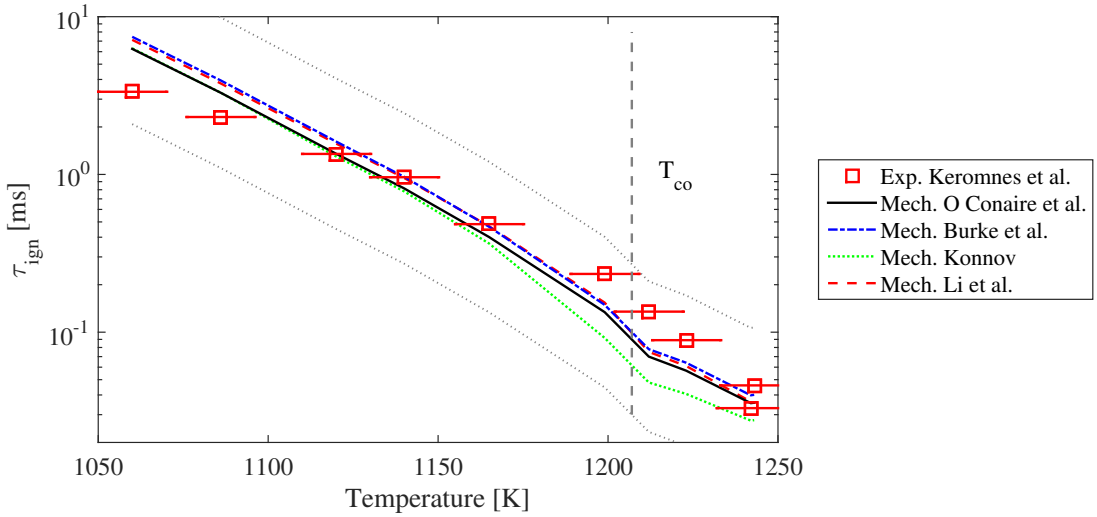

Figure 5.1.4: Ignition delay times for shock tube experiments by Keromnes et al. at $\Phi = 0.50$

the simulations tend to underestimate the ignition delay times. Whereas at low temperatures, the ignition delay time is predicted increasingly too large compared to the experimental data. All four mechanisms perform very similarly. The mechanism by Ó Conaire et al. is selected as reference mechanism for further studies. The quantitative comparison with the experimental data yields maximum deviations of -48 % (at 1212 K) and +87 % (at 1060 K). If the measurement uncertainty of ± 10 K is included, the model uncertainty results in up to ± 110 %. This is visualized in figure 5.1.4 by the two grey dotted lines.

Conclusions

In a preliminary study it was found that ignition under gas turbine conditions proceeds mainly through HO_2 and H_2O_2 build-up at temperatures below the crossover temperature. This means that the ignition process is more sensitive to (turbulent) transport processes and has a higher temperature sensitivity compared to the majority of turbulent hydrogen ignition experiments in literature, which were conducted under conditions above crossover (section 2.4 Turbulent Jet-in-Hot-Coflow). The experiment by Keromnes et al. [86] was selected as most suitable reference experiment for the validation of the chemical reaction mechanisms. Homogeneous reactor simulations were conducted and compared with the experimental data for the validation of different reaction mechanisms. It was found that the four tested mechanisms have a similar accuracy, which is in the range of ± 110 % under the respective engine conditions.

5.2 Turbulent Mixing in a Jet-in-Crossflow

The experimental reference data at high pressure engine operating conditions (chapter 6, figure 4.2.4: subsystem cases) allows only for a limited validation of the turbulent mixing modeling between fuel jet and oxidizer crossflow. The spatial resolution of the PIV velocity measurements is limited and there is no experimental reference data for the scalar mixing field (section 6.1). Furthermore, at engine operating conditions, there are considerable uncertainties in the inflow conditions, such as turbulence intensity and boundary layer thickness at the computational inflow boundary.
To get a better insight into the turbulence model capabilities for this flow configuration, a generic atmospheric jet-in-crossflow experiment is studied in this section. The test case by Andreopoulos and Rodi [4, 5] was identified as suitable benchmark validation experiment (figure 4.2.4), since the most relevant flow characteristics, the jet to crossflow momentum ratio and high turbulence levels are similar to the high pressure ignition experiment.
Three different turbulence models, Large-Eddy Simulation (LES), Scale-Adaptive Simulation (SAS) and Unsteady-RANS (URANS), are applied and compared with respect to model capabilities and costs. Special attention is payed on the modeling of the shear layer vortices and the wake region.

5.2.1 Atmospheric Flow Experiment by Andreopoulos and Rodi

The validation experiment by Andreopoulos and Rodi [4, 5] was conducted at a velocity ratio of $R = 2$ and a comparable high jet Reynolds number of $Re = 82'000$. Although, this Reynolds number is one order of magnitude smaller compared to the high pressure ignition experiment ($Re = 600'000$), there is no comparable jet-in-crossflow experiment (at the respective velocity ratio) in literature with a higher Reynolds number. Furthermore, at high Reynolds numbers, large velocity gradients at the wall make accurate measurements more difficult [4, 97, 42] (figure 5.2.6, section 6.1). In the generic test case, it is also possible to conduct a well-resolved LES. Since the computational cost for wall-resolved LES scales with $Re^{2.4}$ [140], resolved LES are not feasible for industrial relevant flows at $Re \leq 10^6$ [140]. Whereas, at moderate Reynolds numbers in the range of 10^5, wall-resolved Large-Eddy Simulations are still feasible [140] (section 5.2.3.2). In the generic test case, the application of LES is additionally facilitated, since no side and top walls must be resolved, which is necessary in the high pressure test case. Moreover, just one fluid with constant density and viscosity must be considered. This means only one additional equation for the mixing temperature must be solved, whereas in the test case at engine operating conditions, 19 additional scalar equations are solved for the different species.
The experiments were conducted in a closed-circuit wind tunnel at ambient conditions with

pure air. The jet stream was heated by 4 K above the ambient crossflow temperature and therefore the density is almost identical in both streams. The mixing field was assessed by measurements of the local temperature. The mixture state can be defined by a dimensionless temperature Θ (equation 5.2.1). It is comparable to the mixture fraction Z.

$$\Theta = \frac{T - T_{\mathrm{cf}}}{T_{\mathrm{jet}} - T_{\mathrm{cf}}} \tag{5.2.1}$$

The temperatures were measured by cold-wire probes and the velocity fields were determined by cross-wire probes. At these large test rig dimensions and a convenient environment, detailed data of averaged quantities as well as higher moments and scalar fluxes could be obtained. Furthermore, the boundary conditions are adequately defined. The pipe flow has a diameter of $D = 50$ mm and an upstream length of $12\,D$ from plenum to jet orifice. The jet enters into the plenum with a bulk velocity of $u = 27.8$ m/s.

5.2.2 Numerical Simulation with Non-reacting CFD

The high pressure test case, which is described in detail in chapter 6, is characterized by a high turbulent Reynolds number in the order of 10^6. Such technical flows are typically simulated with RANS models. While this method provides satisfactory results for a large range of flows [23], it has deficiencies in capturing large-scale anisotropic flow structures [53], which are significant in jet-in-crossflows (section 3.2.2). LES approaches, which directly resolve large turbulent structures, should be preferred for such flow types. However, at high turbulent Reynolds numbers, LES can become prohibitively expensive [27, 140]. An alternative can be provided by hybrid RANS/LES turbulence models. Simple or less important flow regions can be modeled by cost-efficent RANS methods, while scale-resolving (LES-like) methods are applied in critical flow regions. In the present work, the Scale-Adaptive Simulation (SAS) approach by Menter and Egorov [116] is applied. In contrast to other hybrid methods, this model does not require any predefined rigid RANS/LES interface. It switches automatically from RANS to LES mode as soon as large unsteady turbulent structures can be resolved by the mesh. Ivanova et al. [76] demonstrated that SAS modeling is more accurate compared to RANS modeling for jets-in-crossflow at intermediate momentum ratios. In the present high pressure test case the jet is injected at a very low momentum ratio of $J = 1\text{-}4$ ($R = 1\text{-}2$). Several studies indicate that transition from RANS to LES is not well defined for such low momentum ratios, since only weak flow instabilities are present in the shear layer [34, 33, 39, 152]. This should also be analyzed in this benchmark study [146].

The computational domain is presented in figure 5.2.1. The spatial dimensions of the grid: streamwise $-2 \leq x/D \leq 7$, lengthwise $-2 \leq y/D \leq 24.4$ and spanwise $-6 \leq z/D \leq 6$ are based on previous DNS and LES studies for similar configurations [177, 154, 52]. The point of origin

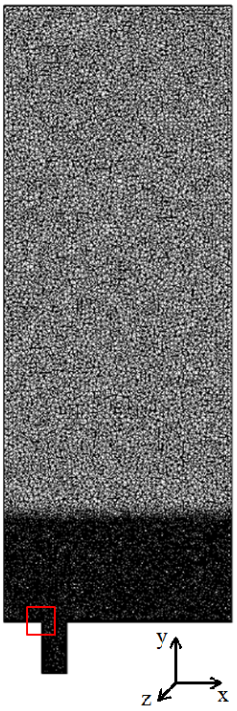

Figure 5.2.1: Full grid

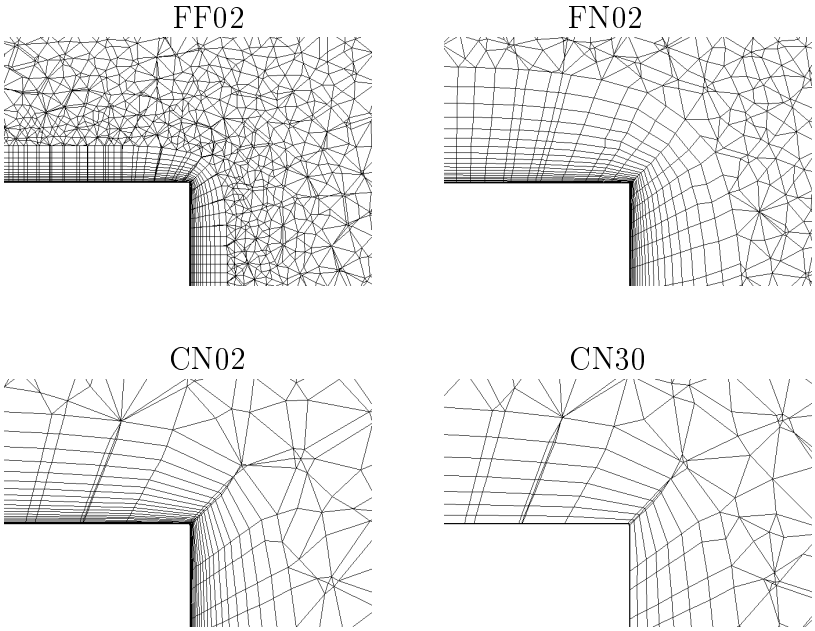

Figure 5.2.2: Grid resolutions at nozzle interface, detail at -0.68 $\leq x/D \leq$ -0.32, -0.10 $\leq y/D \leq$ 0.14

Table 5.2: LES guidelines

Direction	Dimensions
Streamwise:	$50 \leq \Delta x^+ \leq 150$
Wall-normal:	$\Delta y_w^+ < 1$
Spanwise:	$15 \leq \Delta z^+ \leq 40$

Table 5.3: Grid specifications

Grid name	Points [10^6]	$\Delta x_{mix}/D$	$\Delta x_w/D$	Δy_w^+	Δx_{mix}^+
FF02	31.2	0.03	0.008	2	120
FN02	11.0	0.03	0.030	2	120
CN02	2.2	0.06	0.060	2	240
CN30	1.8	0.06	0.060	30	240

is located in the center of the jet orifice. The channel height was chosen in agreement with the experimental dimension to consider the accurate displacement of the coflow. Attention must also be payed to the periodic side walls, which must have a sufficient distance to the jet flow. This is ensured by subsequent analysis of the simulated flow field. At the outlet at $x/D = 7$, the jet flow has a spanwise extension of $z/D = \pm 2.25$, defined on 1 % temperature increase ($\Phi = 0.01$). Therefore a wall distance of $z/D = \pm 6$ is sufficient.

Four different mesh resolutions are tested. The mesh spacing is commonly measured in non-dimensional wall units Δx^+, which is defined by the friction velocity u_τ and the wall shear stress τ_w [23, 142].

$$x^+ = \frac{u_\tau x}{\nu} \qquad \text{with} \qquad u_\tau = \left(\frac{\tau_w}{\rho}\right)^{1/2} \tag{5.2.2}$$

Recommendations for an adequate LES resolution are given in a NASA memorandum by Georgiadis et al. [55]. The guidelines are presented in table 5.2. Similar values can also be found in Davidson [29] and Menter [115]. In the strict sense, the notation in wall units can only be applied to "flat-plate-like" configurations [55] with homogeneous flow direction. In flows with no homogeneous flow direction [55], such as separating or swirling flows [23], the definition of the reference wall shear value τ_w is not clearly defined. Nevertheless, wall units are a convenient quantity to compare grid resolutions with consideration of the flow Reynolds number. The grid properties, which are applied to the jet-in-crossflow test case by Andreopoulos and Rodi, are listed in table 5.3. The grid characteristics are also indicated by the grid names. The first letters F (Fine) and C (Coarse) describe the main grid resolution: $\Delta x/D = 0.03$ and 0.06 respectively, or when expressed in dimensionless wall units: $\Delta x^+_{mix} = 120$ and 240 based on the pipe flow. The fine grid is within the recommended LES resolution guidelines while the coarse grid resolution is outside of the recommended bounds. At engine conditions, where the Reynolds numbers are usually very high, LES can only be performed at reasonable cost on very coarse grids. Therefore, it is interesting to assess the capability of LES modeling on grids with a comparably coarse resolution. Since the grid is unstructured, the mesh spacing in the domain is constant in all directions ($\Delta x^+_{mix} = \Delta y^+_{mix} = \Delta z^+_{mix}$). The second letter in the grid names refers to the resolution along the walls. N (Normal) is used, when the wall parallel resolution is similar to the resolution in the main domain. In the largest grid FF02, the resolution at the wall is additionally reFined. The last two numeric characters describe the first wall normal cell size in non-dimensional wall units Δy^+. A constant time step of $2 \cdot 10^5$ s is used in all computations, which results in CFL numbers smaller than 0.6.

Three different turbulence models are applied in this work. These are namely Large-Eddy Simulation (LES), Scale-Adaptive Simulation (SAS) and Unsteady Reynolds-Averaged Navier-Stokes Simulation (URANS). The methods are described in detail in section 3.2.2. Unsteady velocity fields are applied in the LES computations. Therefore, additional LES of a flat plate and a turbulent pipe flow were conducted and time-resolved slices were extracted and saved in accordance with the experimental measurements. During the simulation of the jet-in-crossflow, these slices were applied to the inlet boundaries at each new time step. Furthermore, the time-averaged LES inflow data is used as inflow condition for the SAS and URANS simulations. In the grids with full wall resolution, the turbulent boundary layers are directly simulated by the turbulence model. In the coarsest grid CN30, a first wall cell height of $\Delta y^+ = 30$ and empirical wall functions are applied. The scalar heat transport is closed by the gradient-diffusion hypothesis with a turbulent Prandtl number of $Pr_t = 1.0$ (section 3.2.2.1). Adiabatic boundary conditions are applied at the walls.

5.2.3 Validation of Turbulence Modeling

As described in section 2.5, there are two critical regions for the simulation of reacting jets-in-hot-crossflow. These are located in the lean shear layer around Z_{mr}, where ignition events occur preferentially as well as the low velocity wake region ($x/D \leq 5$), which is important for the flame anchoring process. The following evaluation of turbulence modeling is therefore focused on these two regions. All results are evaluated at the plane of symmetry $z/D = 0$.

5.2.3.1 Periodic Shear Layer Vortices

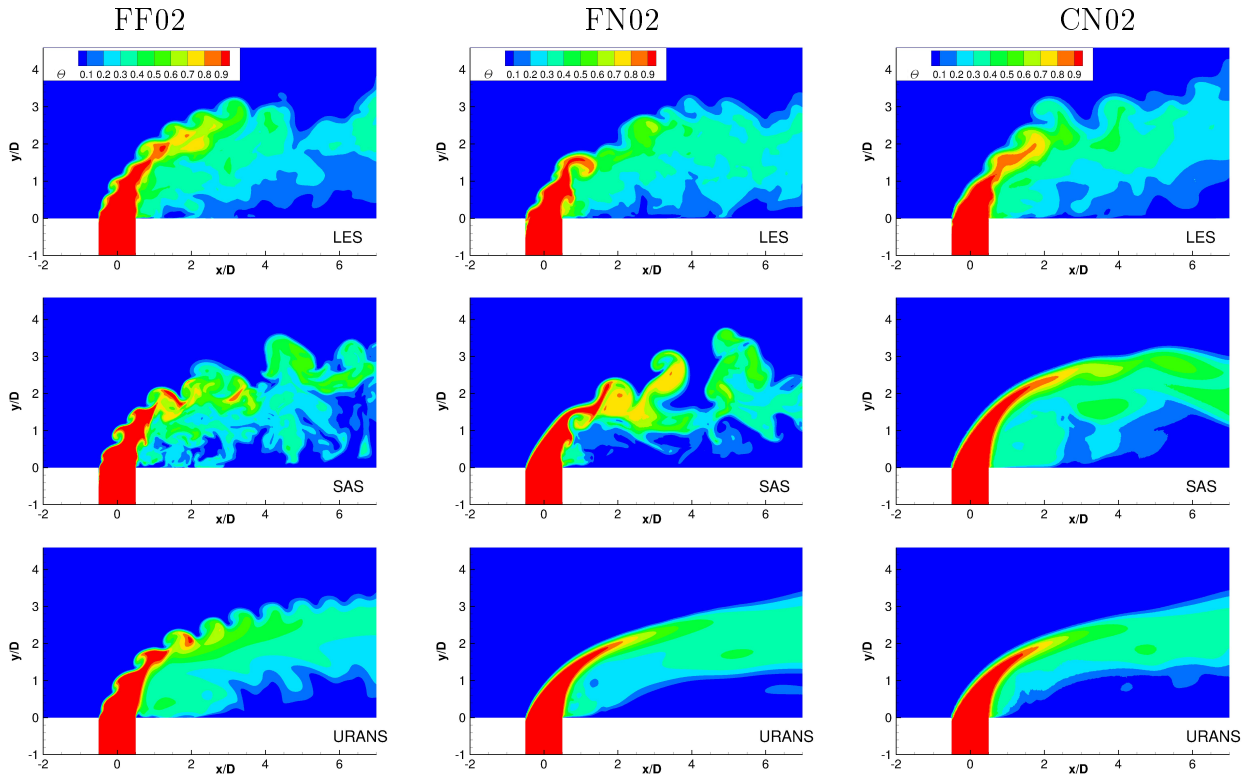

Figure 5.2.3: Instantaneous mixture field at $z/D = 0$

It is demonstrated in section 5.3 (Turbulent Autoignition in a Jet-in-Hot-Coflow), that the transient ignition process and the minimum ignition location depend strongly on the time-dependent evolution and associated local properties of large periodic shear layer vortices. To capture the rare most-upstream ignition kernels with computational models, it is therefore necessary to resolve these vortices. A good impression of the shear layer vortex resolution can be gained from instantaneous mixture plots. These are presented in figure 5.2.3. At the highest grid resolution (FF02) the periodic vortex structures are reproduced with all three turbulence models. With the smaller grids (FN02 and CN02), the shear layer vortices are less distinct.

Influence of Pipe Wall Resolution: Particularly interesting is the fact, that the resolution along the walls seems to have a large influence on the shear layer vortex shedding, comparing grids FF02 and FN02. The main grid resolution of both grids is similar, only the wall resolution in the main flow direction is refined in grid FF02.

At this low velocity ratio ($R = 2$), the shear layer vortices are not only produced by Kelvin-Helmholtz instabilities in the jet-crossflow interface above the jet nozzle. Kelso at al. [84] describe the existence of a so called "hovering vortex", which surrounds the jet at the front and side in the vicinity of the nozzle. At Reynolds numbers above 1500, this vortex is unstable. It moves up and down and produces periodic vortices on the windward side of the jet. These shear layer vortices are of very large scale and more periodic compared to pure Kelvin-Helmholtz instabilities. The mechanism is well captured by the high resolved computations (FF02). Figure 5.2.4 presents the averaged (left) and an instantaneous (right) mixture field for the LES on the finest grid FF02 at the jet-crossflow interface. Streamlines indicate the flow directions. In average, the hovering vortex is located in the pipe at x/D = -0.496 and y/D = -0.066. The periodic vortex shedding becomes obvious in the instantaneous plot. In both perspectives, crossflow fluid is entrained into the pipe. More detail on the shear layer vortex shedding is presented in figure 5.2.5. The temporal evolution of the streamwise jet velocity V is shown for a monitor point at the jet orifice (x/D = -0.496 and $y/D = 0$). Strong velocity pulsations in positive and negative direction are present in the high resolved LES (FF02). The amplitude is reduced when the wall resolution is coarsened (LES on FN02). With the SAS on the finest grid (FF02), some periodic fluctuations are still reproduced. But these are much smaller and smoother. When the resolution along the wall is reduced (grid FN02), vortex shedding within the pipe by the hovering vortex can not be reproduced. Nevertheless, some vortex structures in the shear layer are still resolved (figure 5.2.3, FN02, SAS). But these are solely produced by Kelvin-Helmholtz instabilities. With the coarsest resolution CN02, the SAS and URANS turbulence models do not resolve any distinct vortex structures, not even any Kelvin-Helmholtz instabilities.

5.2.3.2 Large-Eddy-Simulation

A quantitative validation can be obtained from the time-averaged results. The wall-resolved LES runs are presented figure 5.2.6. The profiles are plotted at four streamwise positions ($x/D = 0$, 2, 4 and 6), which are indicated at the bottom x-axis. The scaling of the streamwise velocity U and the dimensionless temperature Θ can be found at the top x-axis. In general, good agreement with experimental data is obtained for all three grids. Nevertheless the jet trajectory, defined by the position of the maximum streamwise velocity U, is slightly higher on the coarse grid CN02. The experimental data is met very well with the higher resolution grids

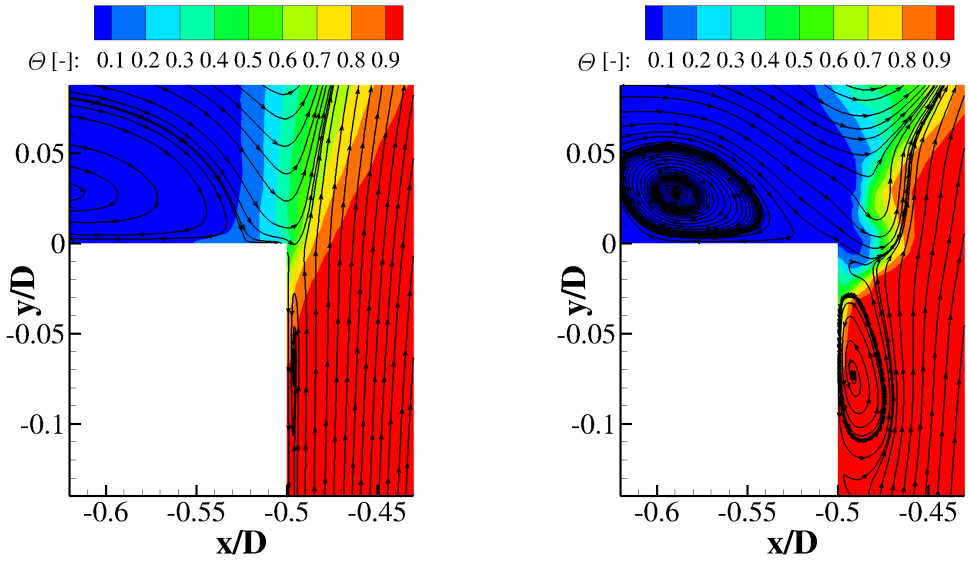

Figure 5.2.4: Mixture field with stream lines at the leading edge of the pipe orifice for LES with grid FF02, left: time-averaged, right: instantaneous

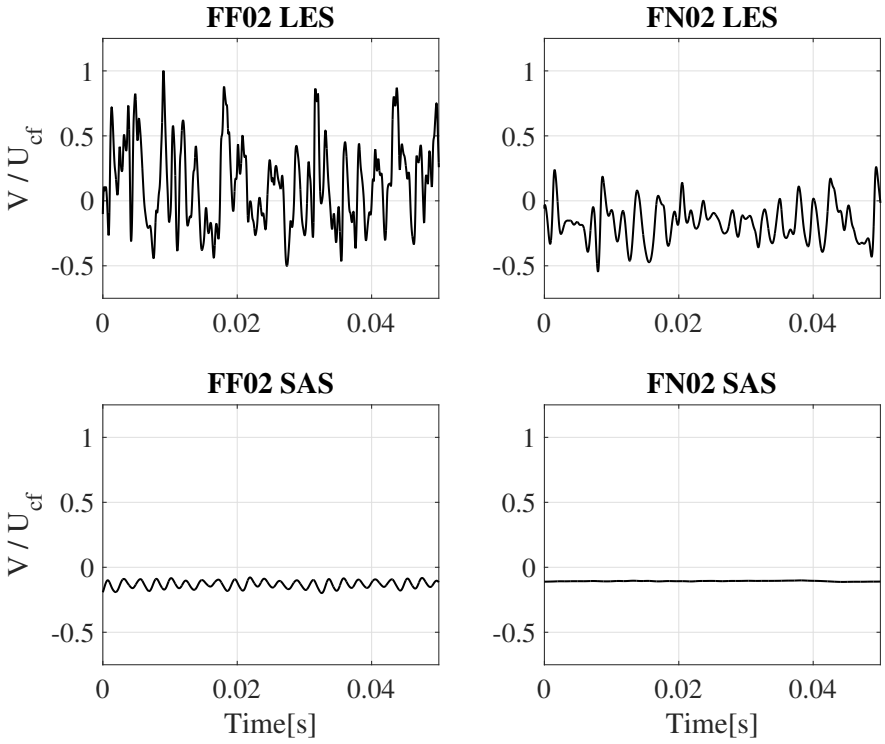

Figure 5.2.5: Temporal evolution of upstream velocity U at the leading edge of the pipe orifice ($x/D = $-0.496 and $y/D = 0$)

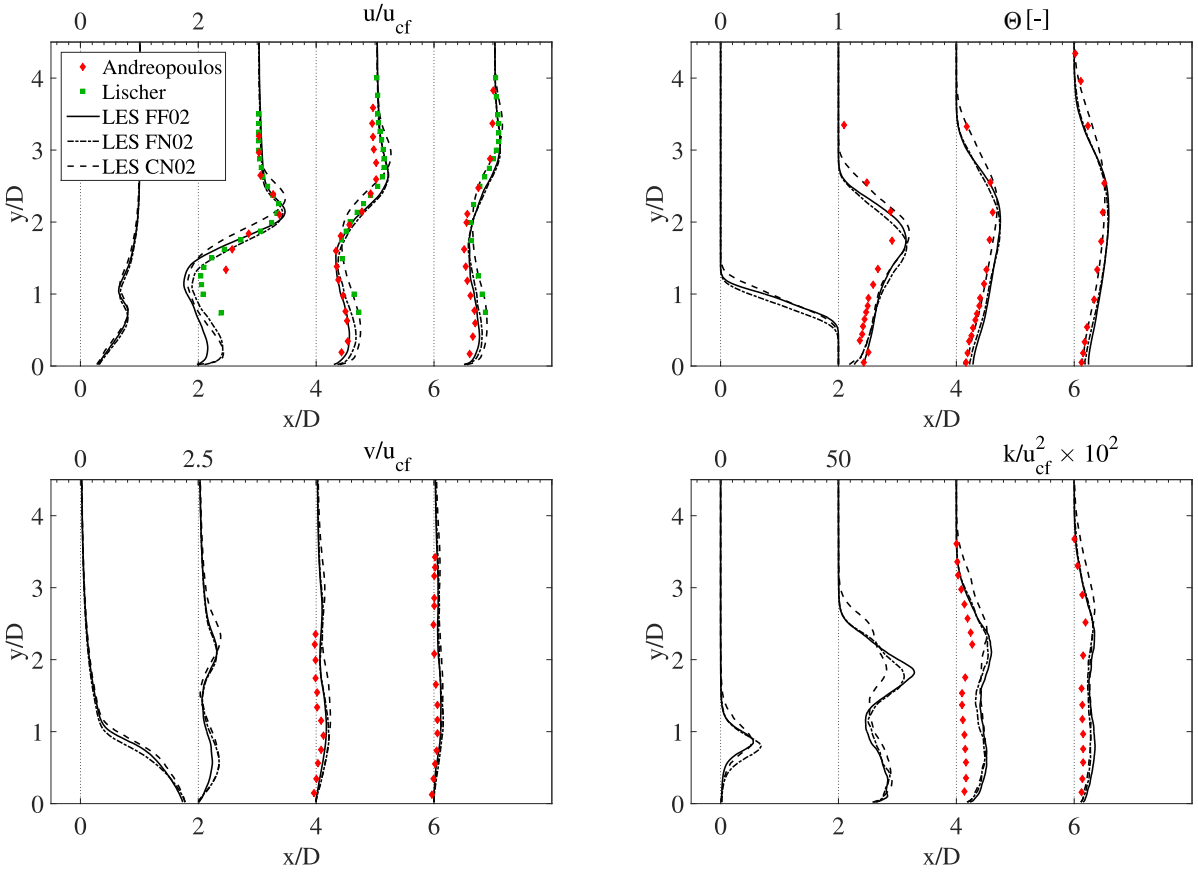

Figure 5.2.6: LES grid study: Time-averaged profiles at $z/D = 0$ for various streamwise positions $x/D = 0$, 2, 4 and 6

FF02 and FN02. In the front part of the low velocity wake region, at $x/D = 2$ and $y/D = 1.5$, the simulations deviate visibly from the experimental measurement by Andreopoulos and Rodi. In this region the average streamwise velocity is close to zero. Since hot-wire probes cannot resolve the direction of the flow, instantaneous negative velocities might have been misinterpreted and considered wrongly with a positive direction. Therefore, comparative PIV measurements of the streamwise velocity U were conducted by Donnert and are published in the dissertation of Lischer [97]. The PIV data shows a much better agreement with the simulations in the low velocity region.

Of special interest with regard to ignition is the mixing in the lean shear layer region at mixture fractions below $Z = 0.1$ (sections 2.3 and 5.1), corresponding to $\Theta = 0.1$ At these conditions the mixture fraction gradient on the two smaller grids FN02 and CN02 is less steep compared to grid FF02. This can be related to the insufficient resolution of the large-scale vortex shedding by the hovering vortex, which was explained in section 5.2.3.1.

5.2.3.3 Scale-Adaptive-Simulation

In the subsystem experiments which are investigated in chapter 6, the Reynolds numbers are in the order of 10^6. As described above, at such high Reynolds numbers, LES with sufficient grid resolution is not feasible. The Scale-Adaptive Simulation (SAS) approach (section 3.2.2.2) provides a combination of cost-efficient RANS modeling for the inflow streams and scale-resolving modeling of the jet-crossflow mixing. Unfortunately, at engine operating conditions (section 6.1) there is no sufficient experimental reference data to validate the SAS modeling approach for the jet-in-crossflow mixing. Therefore, the capability of the SAS modeling is validated in the present chapter for a similar configuration with detailed experimental reference data and well-resolved LES results (figures 5.2.6 and 5.2.10). However, when comparing LES and SAS results, it must be considered that unsteady turbulent structures are applied at the LES inflow; whereas time-average quantities are applied at the SAS inflow to validate the performance of the integrated RANS/LES-switch at the jet interface. The performance of the SAS is also compared to URANS modeling. The results are presented in figures 5.2.7 to 5.2.10. The SAS capabilities are compared with LES and URANS on grids FF02 and CN02.

High grid resolution: The performance of the SAS on the finest grid FF02 is comparable to the LES run (figure 5.2.7). There are just minor differences between SAS and LES, whereas the URANS deviates significantly. This is particularly distinct for the time-averaged velocities at the locations $x/D = 2$ and 4. The ratio of the turbulent kinetic energy in figure 5.2.8 (top, center) clearly reveals the SAS switch from URANS to LES mode. The SAS model is in URANS mode in the incoming pipe flow and crossflow. The transition takes place quickly. Within 1 pipe diameter from the orifice, more than 80 % of the turbulent velocity fluctuations are resolved. Also the turbulent viscosity ratio with a maximum value of $r_{\nu,SAS,max} = \max\left(\nu_t/\nu\right)_{\mathrm{SAS}} = 74$ (figure 5.2.8) indicates a good scale resolution. In contrast, with URANS almost no turbulent structures are resolved along the jet trajectory ($u_{\max}$) and in the wake (figure 5.2.3). The maximum viscosity ratio reaches $r_{\nu,\mathrm{URANS,max}} = \max\left(\nu_t/\nu\right)_{\mathrm{URANS}} = 1550$ (figure 5.2.8).

Coarse grid resolution: On the coarse grid CN02 the SAS results are less accurate (figure 5.2.9). The mixing is significantly underestimated with SAS and URANS. The mixture fraction gradient in the upper shear layer is too steep, the jet spread and its mixing is delayed. From the instantaneous mixture fraction fields (figure 5.2.3) can be concluded that no distinct shear layer vortices are resolved with SAS and URANS. Here the SAS profiles are quite comparable to the URANS results, although the jet penetrates more into the crossflow (figure 5.2.9). From this it can be concluded, that the transition into scale-resolving mode

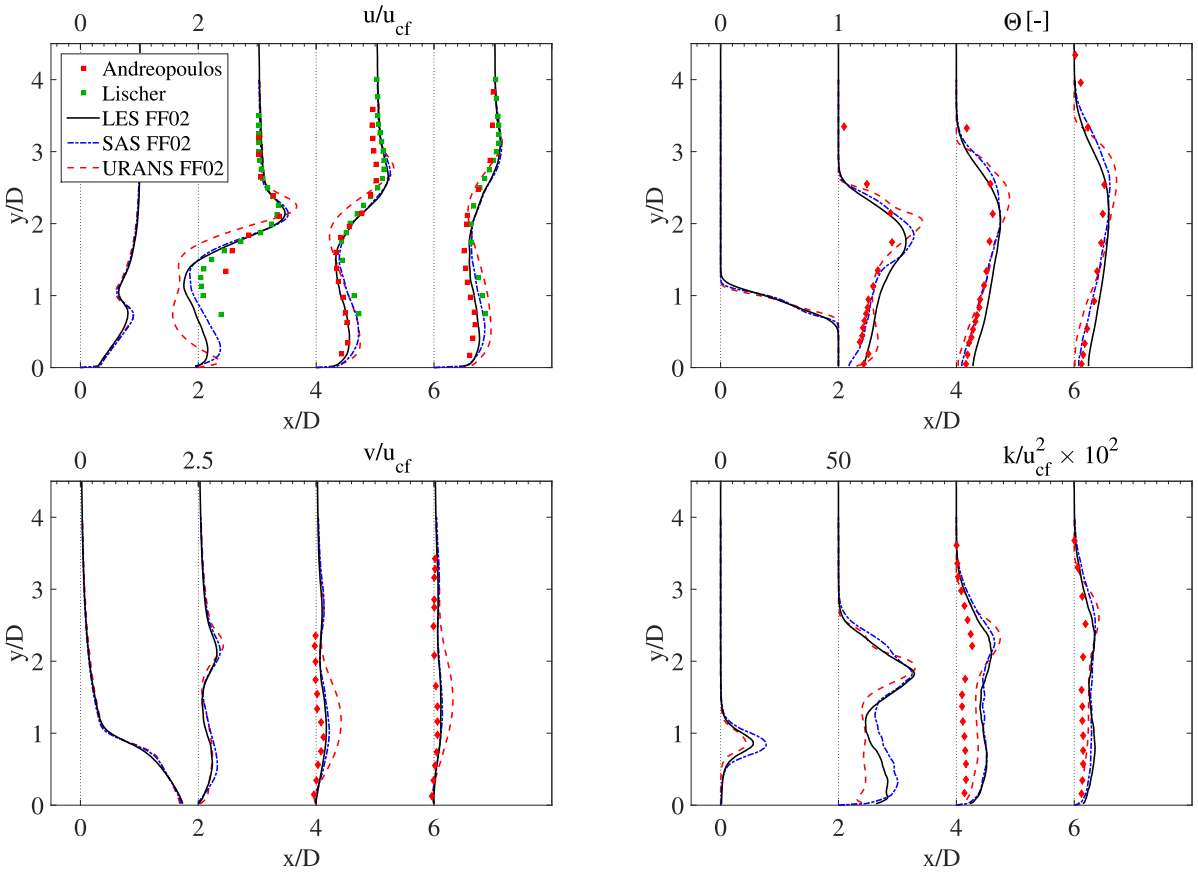

Figure 5.2.7: SAS grid study: Time-averaged profiles at $z/D = 0$ for various streamwise positions $x/D = 0$, 2, 4 and 6

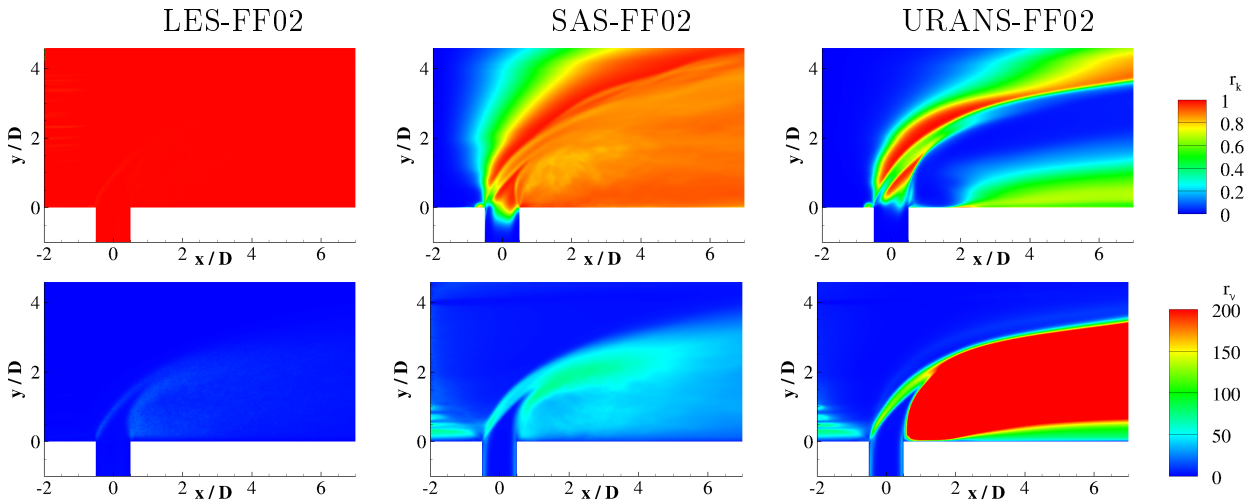

Figure 5.2.8: FF02: Quality of turbulence resolution, top: ratio of turbulent kinetic energy, bottom: turbulent viscosity ratio

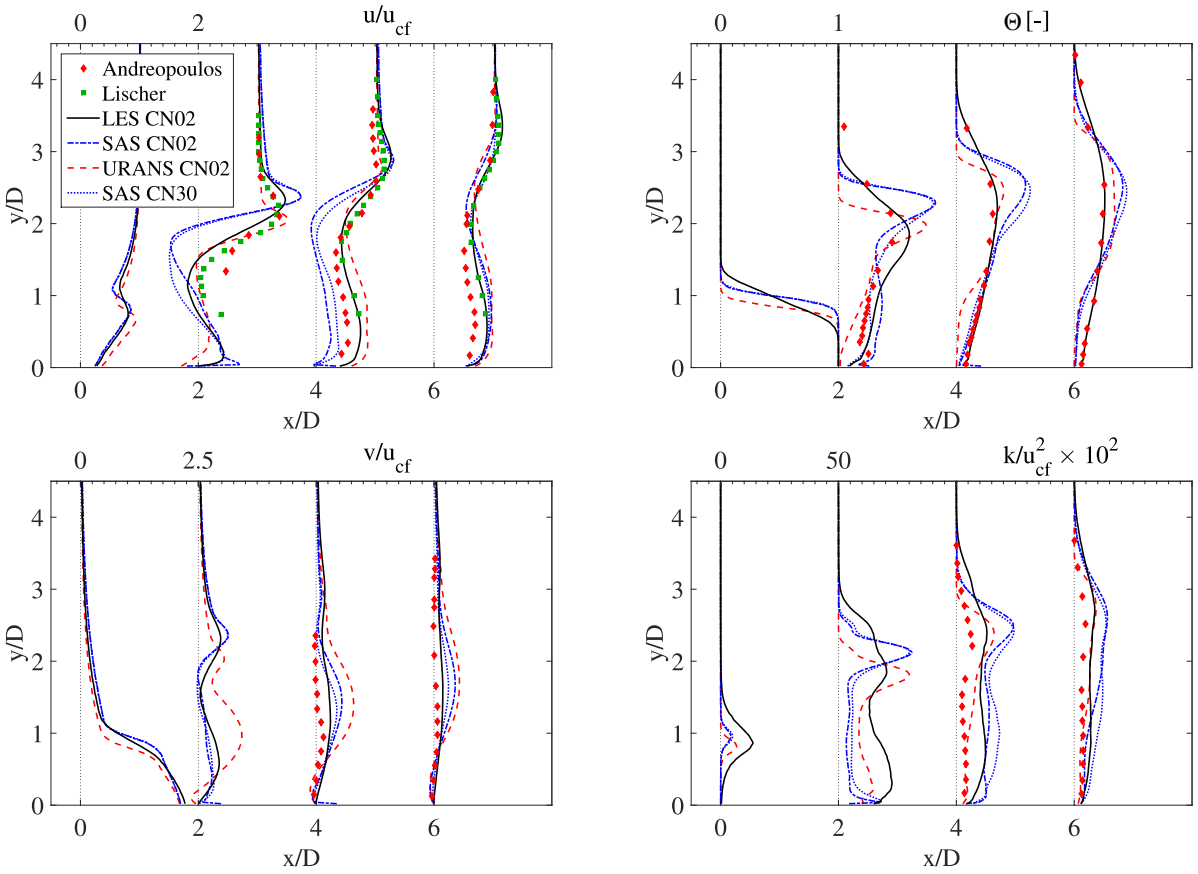

Figure 5.2.9: SAS grid study CN02: Time-averaged profiles at $z/D = 0$ for various streamwise positions $x/D = 0$, 2, 4 and 6

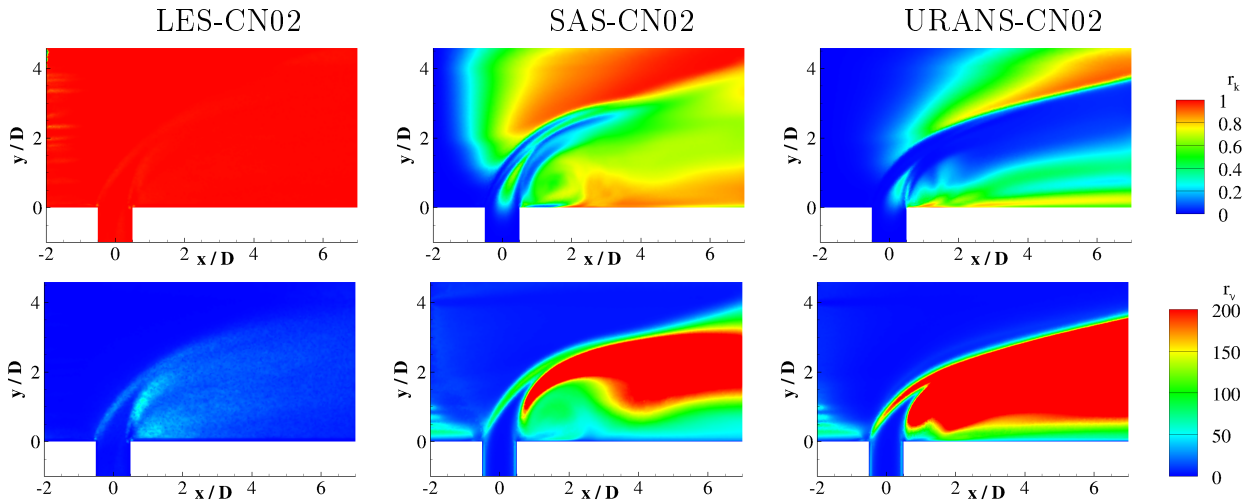

Figure 5.2.10: CN02: Quality of turbulence resolution, top: ratio of turbulent kinetic energy, bottom: turbulent viscosity ratio

is delayed and not completed in the most part of the domain (figure 5.2.10). Nevertheless, more scales are resolved compared to URANS. With respect to the wake, the SAS performs much better compared to the URANS. Especially at $x/D = 2$ and $x/D = 4$ better mixing can be achieved for $y/D < 1.5$.
Finally, the SAS results with wall functions on grid CN30 are also included in figure 5.2.9. It is demonstrated, that the application of wall functions gives comparable results to computations with wall resolution (CN02). Hence, by application of wall functions, the grid size can be reduced further to save computational resources, while keeping a similar modeling accuracy.

Conclusions

Table 5.4: Modeling costs and turbulence resolution quality

Grid name	Grid points $[10^6]$	$\Delta x_{\mathrm{mix}}/D$	CPU time [h]	$\max(\nu_t/\nu)$ LES	$\max(\nu_t/\nu)$ SAS	$\max(\nu_t/\nu)$ URANS
FF02	31.2	0.03	1100	23	74	1550
FN02	11.0	0.03	600	24	94	1370
CN02	2.2	0.06	80	60	540	1370
CN30	1.8	0.06	40	-	540	1320

In table 5.4 a quantitative overview of cost and quality is presented for the different grids and turbulence models. The computational costs are given in CPU hours per crossflow residence time (0.032 s). It varies only with the number of grid points, while the turbulence model has hardly any influence. The turbulence resolution quality is specified by the maximum viscosity ratio. It depends on both, the grid resolution as well as the turbulence model.
The LES performs surprisingly well on all three grids. However, in technical applications with at higher Reynolds numbers, the computational costs can become unaffordable. The hybrid SAS model allows to switch between URANS or LES modes automatically in different flow sections. In jet-in-crossflow applications much cost can be saved when upstream and downstream ducts are modeled with URANS and the jet-crossflow mixing region is computed by a scale-resolving model.
With respect to SAS modeling, two important conclusions can be derived from this investigation. First, the shear layer vortices can only be resolved with very high grid resolution and special emphasis must be payed on the resolution of the wall shear layer close to the jet-to-crossflow interface. The spatial and temporal resolution of these shear layer vortices is critical to capture first ignition events as shown in the previous section 5.3. Second, the SAS turbulence model should be favored above the URANS model, since it captures the mixing process in the wake more accurately. However, in the shear layer both models underestimate the mixing process to a similar extend.

5.3 Turbulent Autoignition in a Jet-in-Hot-Coflow

The major objective of the third labscale study is the investigation and model validation of the turbulence-chemistry interaction. As demonstrated in sections 2.2 and 5.1, hydrogen autoignition below crossover is very sensitive to turbulent transport and temperature variations. Both influences lead to an increased variation and scattering of the local ignition process. This is also observed in the subsystem experiment at engine operating conditions of Fleck et al. [45]. The autoignition kernels occur clearly separated with a very large spatial distribution in the location of their first emergence. This large variation is of special significance in the jet-in-crossflow configuration, since the most upstream kernels can initiate flame anchoring in the low velocity region of the jet lee (sections 2.5 and 5.2). To reproduce this anchoring process in the jet lee, it is necessary to capture the spatial kernel distribution accurately.

A suited experiment for the investigation of ignition scattering is the turbulent jet-in-hot-coflow test case (DLR JHC) of Arndt et al. [8]. In contrast to other jet-in-hot-coflow experiments (section 2.4), where often only the average lift-off height has been assessed, the study of Arndt et al. provides detailed statistical information on the individual ignition events. Furthermore, high-resolved, high-speed optical measurements give insight into the physical turbulence-chemistry interaction during the ignition process.

These measurements were conducted at labscale test conditions at atmospheric pressure and intermediate Reynolds number. The reduced Reynolds number facilitates the application of sufficiently resolved Large-Eddy Simulation. The analysis of the numerical results is divided into two parts. In section 5.3.3, the TCI modeling is validated first with respect to statistical experimental data. Afterwards in section 5.3.4, the time-resolved LES results are used to analyze the transient ignition process.

5.3.1 Atmospheric Autoignition Experiment by Arndt et al.

Table 5.5: Inflow conditions for the numerical simulation; the gas compositions are given in mass fraction

	$\dot{m}$ [g/s]	T [K]	Y_{N2} [-]	Y_{O2} [-]	Y_{H2O} [-]	Y_{OH} [-]	Y_{CH4} [-]
Coflow	4.814	1495	0.7565	0.1228	0.1206	0.0001	0
Jet	0.207	290	0	0	0	0	1.0

A couple of contributions have been published recently on extensive measurements in the DLR Jet-in-Hot-Coflow Burner (DLR JHC) [111, 10, 7, 9, 138, 8]. The experiments were conducted by groups at DLR Stuttgart and the Ohio State University. This test case differs

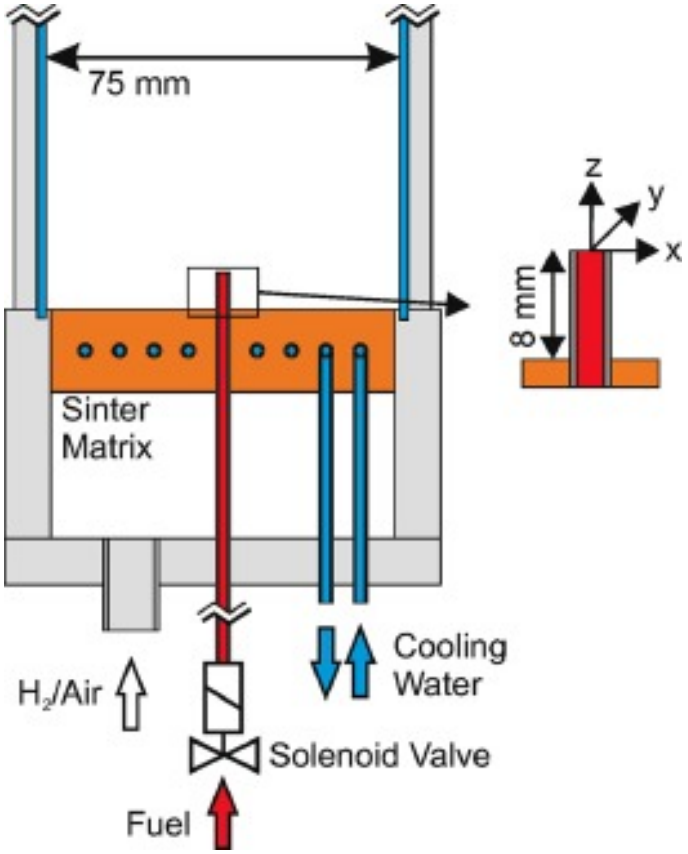

Figure 5.3.1: Experimental setup of the DLR JHC burner, figure reprinted from Arndt et al. [8] with permission from Elsevier

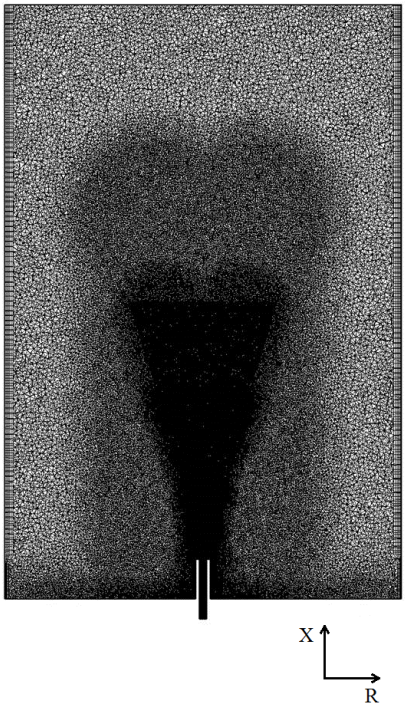

Figure 5.3.2: Computational grid

from other jet-in-hot-coflow experiments in the transient injection of the fuel jet (compare section 2.4). This procedure allows to measure the accurate ignition time and location and its dependence on specific parameters, such as the local mixture conditions and scalar dissipation rate.

The experimental setup is presented in figure 5.3.1. The combustion chamber has a square cross-sectional area with 80 x 80 mm and a length of 120 mm. It consists of 4 large quartz glas windows. In the measurements of mixture fraction and temperature two windows were removed, but no relevant disturbance on the coflow was detected within the region of interest. The hot coflow is generated by a lean hydrogen-air flame, which is stabilized on a sinter matrix with 75 x 75 mm cross section. The experiments were conducted at atmospheric conditions. The exhaust gas has a temperature of 1495 K, which is about 4 % lower than the adiabtic flame temperature. This value has been verified by measurement and can be assessed with an accuracy of 1 - 2 % using high-speed Rayleigh scattering [8]. Since the ignition delay time is very sensitive to temperature, the quantitative specification of the temperature uncertainty

is very important for a reliable validation. But such a high accuracy can only be achieved at labscale conditions. The coflow composition for chemical equilibrium and the total mass flow rate are given in table 5.5. The resulting coflow velocity is approximately 4 m/s.

The fuel nozzle is elevated by 8 mm above the sinter matrix. Methane fuel is injected from an orifice with a 1.5 mm diameter. The bulk exit velocity is 178 m/s, which results in a Reynolds number of 15'400. Upstream of the nozzle, the pipe has a length of more than 150 diameters. Hence, the pipe flow is fully developed at the pipe exit.

The experimental reference data comprises simultaneous high-speed measurements of mixture fraction and temperature, which were conducted with planar Rayleigh-scattering. Furthermore, quantitative data of hydroxyl concentration is provided from planar laser-induced fluorescence (PLIF). Statistical data of the lift-off height was obtained from OH* chemiluminescence imaging. The experimental methods are described in Arndt et al. [8].

5.3.2 Numerical Simulation with LES/URANS and Assumed PDF

Two turbulence models are applied for the study of the jet-in-hot-coflow: The URANS SST model and the LES WALE model (section 3.2.2.1). The closure of the chemical source term is provided by the APDF model (section 3.2.3). However, with LES only the influence of the unresolved subgrid fluctuations must be modeled. The chemical reactions are specified by the reduced mechanism DRM19 [83]. It is based on the GRI-Mech 1.2 and considers 19 species and 84 reactions [49, 48]. Furthermore, the residence time is modeled for the jet flow. The numerical methods are described in detail in chapter 3 (section 3.2.4).

The computational grid is shown in figure 5.3.2. In the ignition region the grid is resolved by 0.3 mm. The first wall layer inside the pipe has a height of 0.006 mm, which gives a dimensionless wall distance Δy_w^+ of 3.5. The total grid comprises about 1.2 million grid points. About 1/3 of these is required for the short pipe flow. The temporal resolution is set to $5 \cdot 10^{-8}$ s.

The inflow boundary for the turbulent pipe flow is set 8 jet diameters upstream of the jet inlet. In the URANS, steady-state profiles for velocity, turbulent kinetic energy and omega are applied. In the LES, unsteady velocity fields are imported at each time step, which were generated previously by a separate LES of a developed turbulent pipe flow. The top part of the pipe wall, which is sourrounded by hot coflow, is subject to heat transport. The wall temperatures were estimated by an analytic 1D heat flux balance across a 0.75 mm stainless steel cylinder wall [90]. Afterwards, preliminary CFD simulations were conducted to adjust the wall temperatures by matching the heat fluxes across the inner and outer pipe walls. Thus, the final wall temperatures are set to 460 K inside and to 471 K at the outer surface of the pipe. Since the jet inlet is located downstream of the coflow inlet, it can be assumed that

the coflow exhaust gas is in chemical equilibrium state, when the mixing starts. Therefore, equilibrium conditions are applied at the coflow inlet boundary. The inflow is treated laminar and the sides are bounded by walls.

5.3.3 Validation of TCI Modeling

This section is divided into three parts. In the first two subsections, the chemical and turbulent mixing modeling are evaluated separately. In the third part, the URANS and LES results are validated with respect to turbulence-chemistry interaction.

5.3.3.1 Chemical Reaction Mechanism

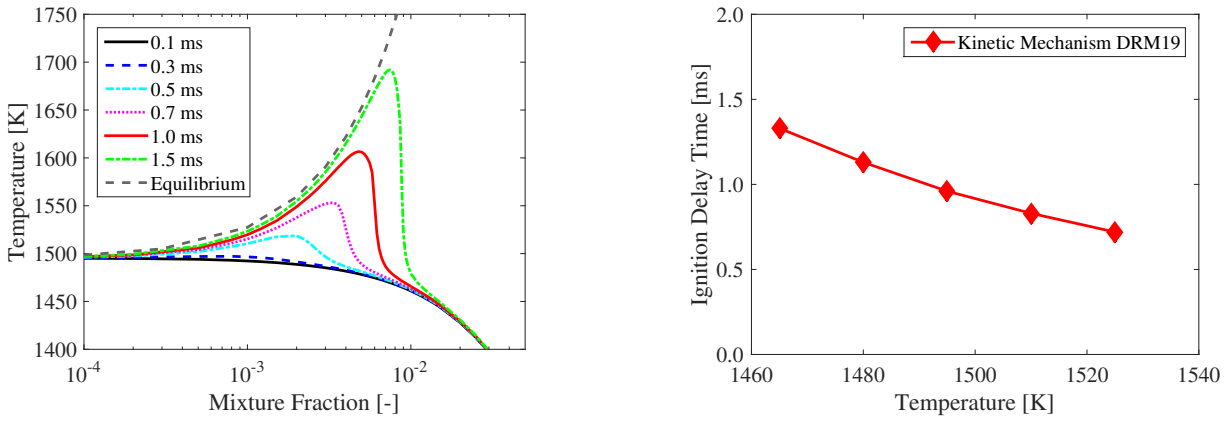

Figure 5.3.3: Chemistry (homogeneous mixtures): Temperature evolution (left) and ignition delay time at $Z = 0.005$ (right) for DLR JHC

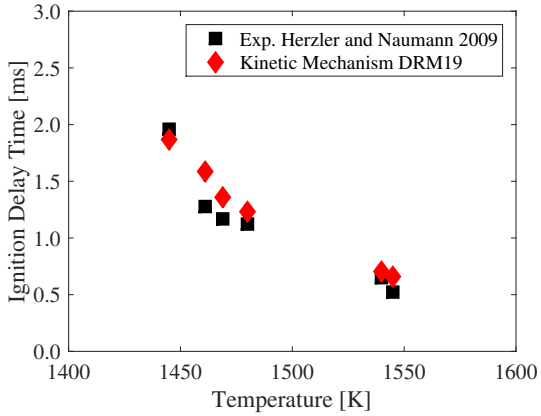

Figure 5.3.4: Chemistry: Validation of kinetic mechanism for reference data by Herzler and Naumann [69]

Before the 3-dimensional test case of the turbulent jet is evaluated, the capabilities of the applied chemical kinetic reaction mechanism are validated. Just as in section 5.1, homogeneous reactor simulations are compared to appropriate shock tube reference data. The relevant ignition conditions are presented in figure 5.3.3. In the DLR JHC test case, ignition is initiated at mixture fractions between $Z = 0.001$ and $Z = 0.01$. At a baseline condition of $Z = 0.005$ ($\Phi = 0.16$, $T_{\mathrm{HG}} = 1495\,\mathrm{K}$), the ignition delay time is $\tau_{\mathrm{ign}} = 0.96\,\mathrm{ms}$ and it is very sensitive to hot gas temperature variations (figure 5.3.3). The temperature of the hot gas can be measured with an accuracy of up to 2 % [8]. This uncertainty results already in an ignition time uncertainty of $\pm 30\,\%$.
The reaction mechanism DRM19 [83] is validated with shock tube measurements by Herzler and Naumann [69]. These were taken in methane/oxygen mixtures, diluted in Argon and with small amounts of ethylene. The equivalence ratio is $\Phi = 0.5$ and measurements were taken at relevant hot gas temperatures and atmospheric pressure. The results are shown in figure 5.3.4. The DRM19-mechanism [83] can predict the ignition delay times with an accuracy of $\pm 25\,\%$ for the respective data points. The combined uncertainty of the chemical reaction modeling, including hot gas temperature and chemical kinetic model, is therefore significant. Thus without consideration of any turbulent influence, the ignition delay time can only be predicted within $\pm 55\,\%$.

5.3.3.2 Turbulent Mixing

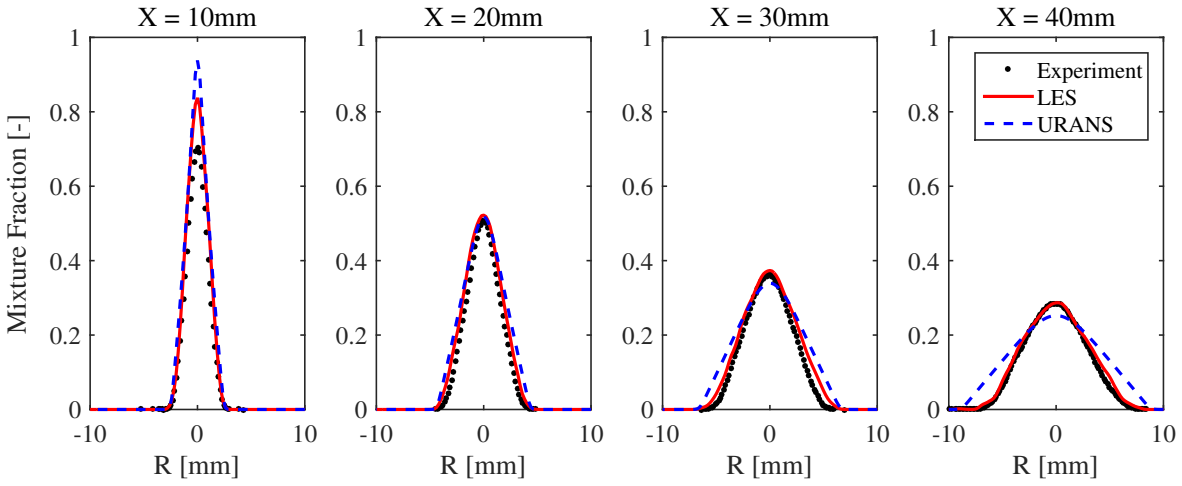

Figure 5.3.5: Turbulent Mixing: Mixture fraction

To get an impression of the turbulence modeling capabilities, the non-reacting mixing field is analyzed. In Figure 5.3.5 the time-averaged mixture fraction distributions are presented at four streamwise positions from $x/D = 10\,\mathrm{mm}$ to $40\,\mathrm{mm}$. The experimental mixture fractions stem from steady-state fuel distributions before the first ignition event. The mixture fraction

corresponds to the methane mass fraction. As demonstrated in section 2.2, this is a valid assumption since no significant fuel is consumed before ignition events occur. The agreement between LES and experiment is very good. According to measurements, the jet core is slightly less mixed at lower positions. But at low mixture fractions (below $Z = 0.01$), where ignition takes place, the data agrees very well. With URANS, the mixing is too fast for lean mixtures. Especially, the tails at the outer periphery of the jet are not captured accurately. At very lean mixtures (below $Z = 0.01$), the mixture fraction gradient is too high and at richer conditions it is smaller compared to the measurements.

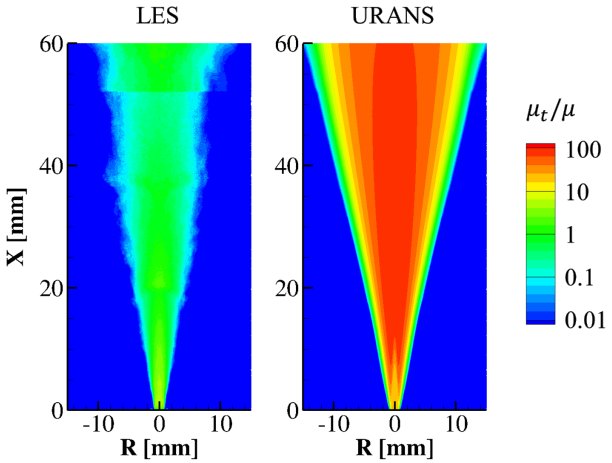

Figure 5.3.6: Turbulent Mixing: Viscosity ratio

The eddy viscosity ratio μ_t/μ is shown in figure 5.3.6. It is plotted in logarithmic scale. With LES, a very good resolution can be achieved. The viscosity ratio is below 10 in the whole domain and even below 1 in the reaction region at low mixture fractions. The ratio of the resolved to the total turbulent kinetic energy k_{res}/k_{tot} is also above 95 % for LES (not shown here). Whereas with URANS, only less than 1 % of the kinetic energy of the fluctuations is directly resolved in the relevant mixture fraction range $Z \geq 0.001$. The viscosity ratio goes up to 100.

5.3.3.3 Turbulence-Chemistry Interaction (TCI)

$$c_{OH} = \frac{p}{RT} X_{OH} N_A \tag{5.3.1}$$

The average flame distribution is represented by the OH number concentration c_{OH}. This quantity is used as reference, since it has been assessed quantitatively from the experimental OH-LIF signal [6]. The OH number concentration is defined in equation 5.3.1 and depends on pressure, temperature and OH mole fraction. The two universal constants are given by $N_A = 6.0221 \cdot 10^{23}\,\mathrm{mol}^{-1}$ and $R = 8.3145\,\mathrm{J/(K\,mol)}$.

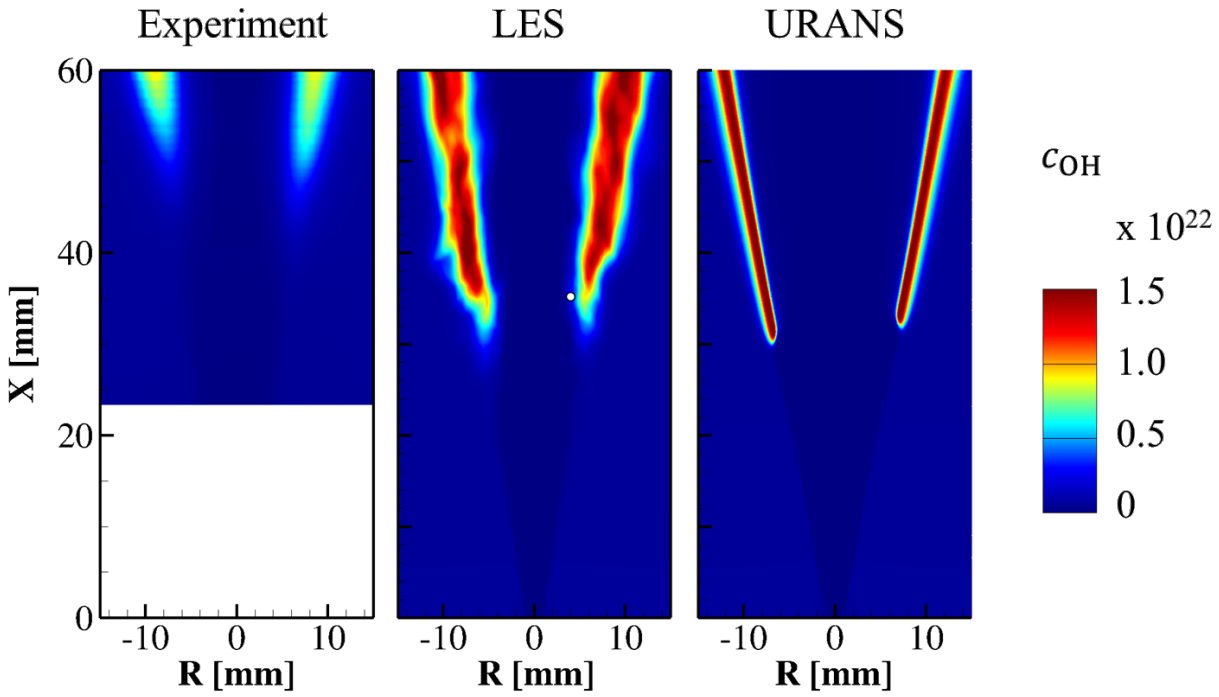

Figure 5.3.7: Turbulence-Chemistry Interaction: Average hydroxyl concentration

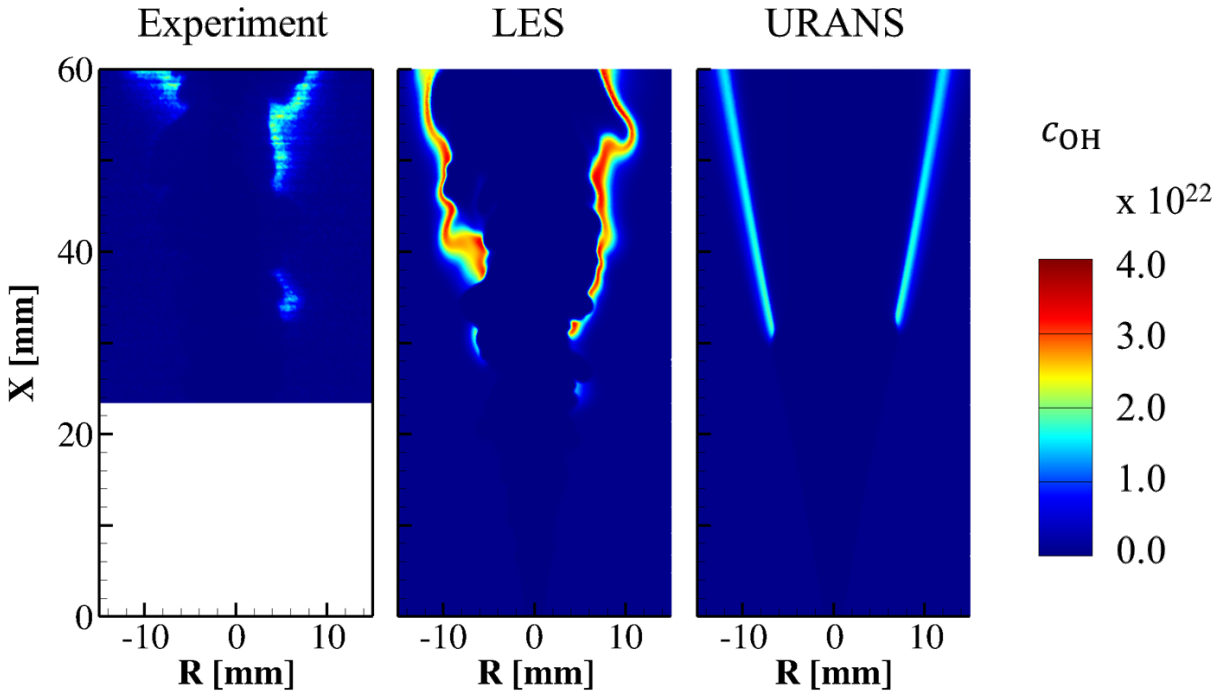

Figure 5.3.8: Turbulence-Chemistry Interaction: Instantaneous hydroxyl concentration

The experimental and numerical results are presented in figure 5.3.7. The maximum time-averaged concentration $c_{\mathrm{OH,max}} = 1 \cdot 10^{22}$ is met with both turbulence models. In the experiment, the averaged lift-off height is located at about 50 mm. In the LES it is shifted upstream by about 20 mm, which is a difference of about 40 %. This discrepancy can be attributed to uncertainties in the hot gas temperature and parameter uncertainties in the chemical reaction mechanism. It is within the respective accuracy limits as shown in the previous subsection. Although, the URANS mixing field deviates significantly from the quite accurate LES results, a very similar average lift-off height can be achieved with URANS compared to LES. The maximum OH concentration is also nearly the same, just the radial width of the flame is a little bit slimmer. Examples of instantaneous c_{OH} distributions are shown in figure 5.3.8. In the time-resolved views of the experiment and LES, the flame front is actually disrupted and considerably scattered in streamwise direction. But the instantaneous URANS result is very similar to the smooth time-averaged distribution and no separate ignition kernels or flame extinction are captured.

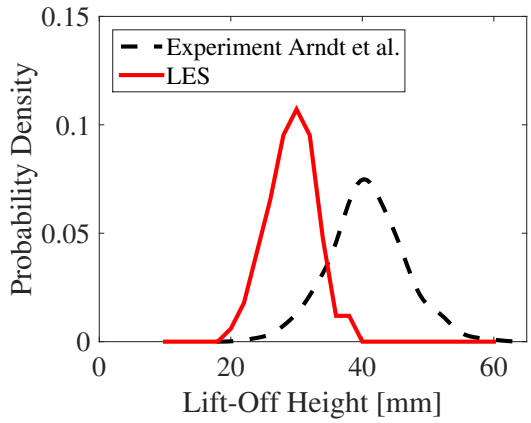

Figure 5.3.9: TCI: Probability density distribution of lift-off height for experiment and simulation

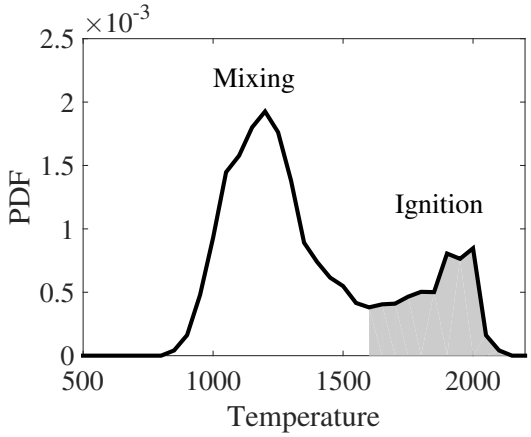

Figure 5.3.10: TCI: Temperature PDF in LES ($R = 35\,\mathrm{mm}$, $X = 4\,\mathrm{mm}$)

Figure 5.3.9 shows the probability density distribution of the lift-off height. In the experiment, the total range of ignition locations is scattered by about 100 % relative to the average lift-off height. The LES exhibits a similar characteristic. The distribution is comparable to the experiment, just the mean is shifted upstream as observed in the 2-dimensional c_{OH}-distributions (figure 5.3.7). The peak is slightly narrower and higher compared to the experiment. This can probably be related to the limited averaging time or might also be due to insufficient spatial resolution of the computational grid as explained in the next paragraph. The URANS probability density distribution is not shown in the plot, since it is almost a Dirac pulse at $x = 31\,\mathrm{mm}$ and almost no variation in the lift-off height can be observed.

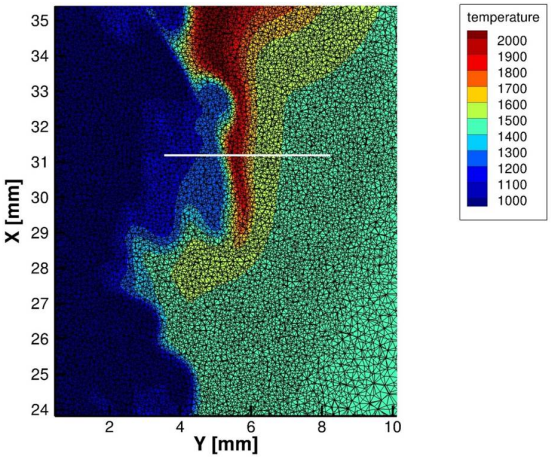

Figure 5.3.11: TCI: Instantaneous distribution of temperature, jet center line is located at the left

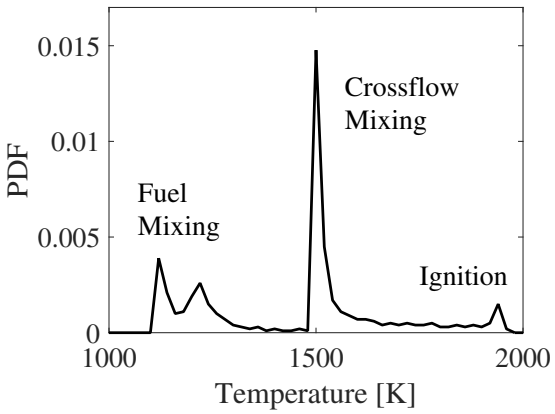

Figure 5.3.12: TCI: Spatial statistics along line between $X = 4$ - $8\,\mathrm{mm}$ at $R = 31\,\mathrm{mm}$

As described previously, the APDF model is applied for modeling of turbulence-chemistry interaction. The temperature is described by the first and second moment (mean and variance) and a Gaussian distribution is assumed to model the impact of unresolved temperature fluctuations on the averaged chemical source term. In the present atmospheric DLR JHC test case, a high resolution of the turbulent scales can be achieved (section 5.3.3.2). The LES results are used to evaluate the temperature distribution in an autoigniting jet flow for the resolved scales. The temperature has been tracked at several locations for about 0.5 ms. Of special interest is the flame root, which is characterized by sporadic evolution of ignition kernels. A representative location for the flame root is selected at $X = 4\,\mathrm{mm}$ and $R = 35\,\mathrm{mm}$ (indicated as white point in figure 5.3.7). The corresponding temperature distribution in figure 5.3.10 actually exhibits a bi-modal shape. The first peak can be related to the mixing of fuel and crossflow, whereas the second peak results from intermittent ignition events. The gray area below the ignition peak can be interpreted as ignition probability. If the TCI model would contain a bi-modal shape for the temperature distribution, it might even be possible to model the variation of ignition height with URANS.

With respect to the high pressure test case, where high LES resolution is not feasible, the influence of coarse spatial resolution is analyzed in figure 5.3.11. The local temperature distribution is analyzed across the flame front at the flame root. In the presented example, the temperatures are evaluated along the white line at $R = 31\,\mathrm{mm}$ between $X = 4$ - $8\,\mathrm{mm}$. In this example, also the instantaneous spatial distribution has a multi-modal shape. Therefore, it must be considered, that the spatial variation of ignition locations might also not be fully captured with the present APDF approach if the LES resolution is too coarse.

5.3.4 Analysis of Transient Ignition Process

In this part, the LES results are analyzed to study the transient ignition process. It is shown that the physical interaction of turbulence and chemical reaction are responsible for the broad spatial scattering of ignition kernels [145].

5.3.4.1 Setup: Starting Jet

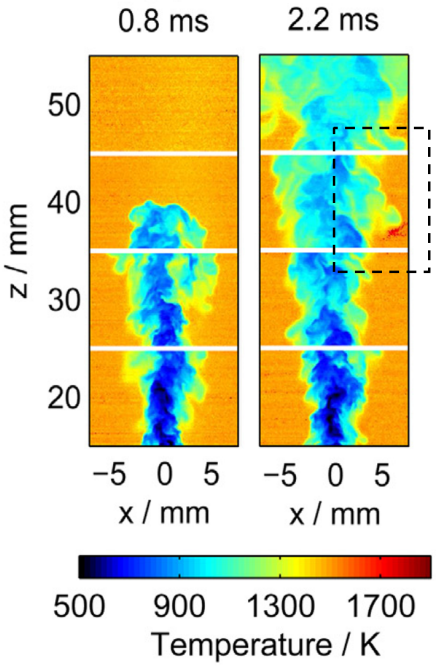

Figure 5.3.13: Experiment: Instantaneous temperature distribution of the starting jet, figure reprinted from Arndt et al. [8] with permission from Elsevier

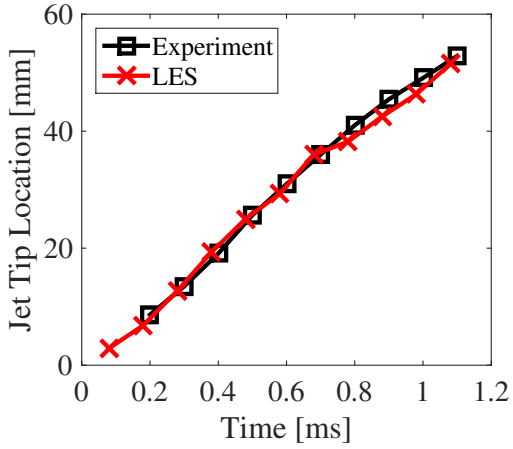

Figure 5.3.14: Experiment and LES: Temporal evolution of jet tip above the orifice

In addition to the steady-state analysis (section 5.3.3), Arndt et al. [8] also investigated the onset of ignition in a pulsed jet. First, they lighted the hydrogen flame on the surface of the sinter matrix to produce a steady hot coflow. Afterwards, the fuel valve was opened and the evolution of the starting fuel jet and the transient process of first ignition events was monitored. The expansion of the starting jet is presented in figure 5.3.13 at $t = 0.8$ and 2.2 ms. The temporal evolution of jet tip position above the nozzle is shown in figure 5.3.14. The jet tip is defined by the stoichiometric mixture fraction. The starting time $t = 0$ ms is defined as the time, when the jet leaves the pipe.

A corresponding LES with transient fuel injection was conducted on the same computational set-up as for the steady-state analysis, which was presented in the previous section. The unsteady pipe inflow velocity profiles were also produced in a preliminary LES pipe com-

putation. However, to model the transient onset after the opening of the fuel valve, the simulation was started from a resting zero-velocity state and a constant pressure gradient was applied along the fuel pipe. The value of the gradient is set in accordance to the fuel mass flow at steady-state conditions. The temporal evolution of the jet tip positions agrees very good with the experimental data, despite this rather simple pressure-drop approach (figure 5.3.14).

5.3.4.2 Comparison with Experimental Results

An exemplary ignition sequence is shown in figure 5.3.15. The frame is indicated in figure 5.3.13. In this experimental sequence, ignition occurred at about 2.2 ms and a height of 37 mm. Simultaneous high-speed measurements of mixture fraction and temperature were conducted [8]. The figure shows the instantaneous mixture fraction in the top row and the squared mixture fraction gradient at the bottom row, which is proportional to the scalar dissipation rate. The red line indicates the stoichiometric mixture fraction $Z_{\mathrm{st}} = 0.0297$ and the white line marks the ignition kernel by the temperature isoline at $T = 1560\,\mathrm{K}$. A corresponding ignition event from the numerical simulation is presented in figure 5.3.16. In this example ignition occurs at 2.3 ms and a height of 46 mm.
Both examples are representative for other ignition events, which were observed in the experiment and the simulation. The ignition mechanism is very similar in experiment and simulation. It can be observed, that ignition kernels always appear at very lean mixture fractions and low scalar dissipation rate (figures at 2.2 ms (experiment) and 2.3 ms (LES)). Similar findings are also reported in literature for more generic configurations as described in section 2.2. Beyond that, the present results show that ignition kernels evolve at the bottom side of large fuel bulges. After ignition the kernels usually grow and penetrate into a concave pocket to the rich fuel side (2.3 - 2.6 ms).
The experimental resolution is limited to mixture fractions above the stoichiometric and also the temperature indicates ignition comparable late. Supplemental information about the mixture fraction at the ignition location and the prior build-up of precursor species can be provided by high fidelity numerical simulation. The new findings on autoignition processes are presented in the next section (section 5.3.4.3).

5.3.4.3 Analysis of Numerical Results

From the numerical results, the most-reactive mixture fraction can be easily extracted and a second mixture fraction isoline is included in figure 5.3.17 at $Z_{\mathrm{mr}} = 0.005$. The mass concentration of the methyl radical (figure 5.3.17) reveals the pre-ignition location and the build-up of the radical pool long before a significant temperature rise occurs. It is evident that the build-up of precursor species is concentrated along the most-reactive mixture fraction. At 2.3 ms

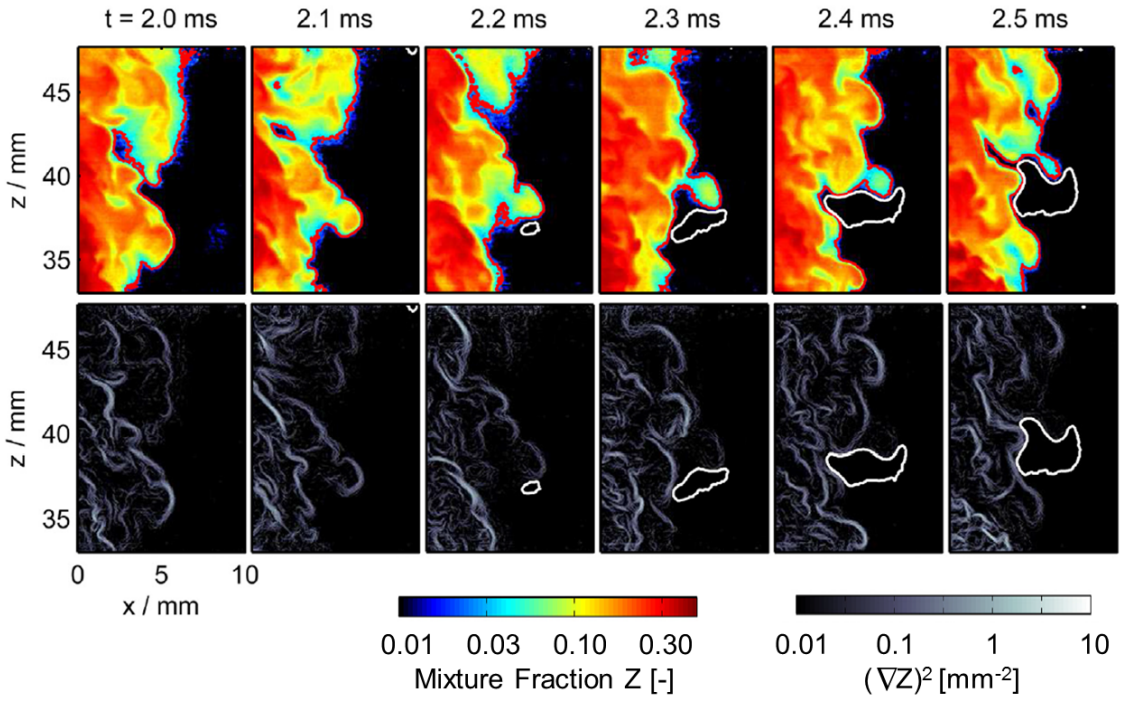

Figure 5.3.15: Experiment: Ignition sequence, figures reprinted from Arndt et al. [8] with permission from Elsevier

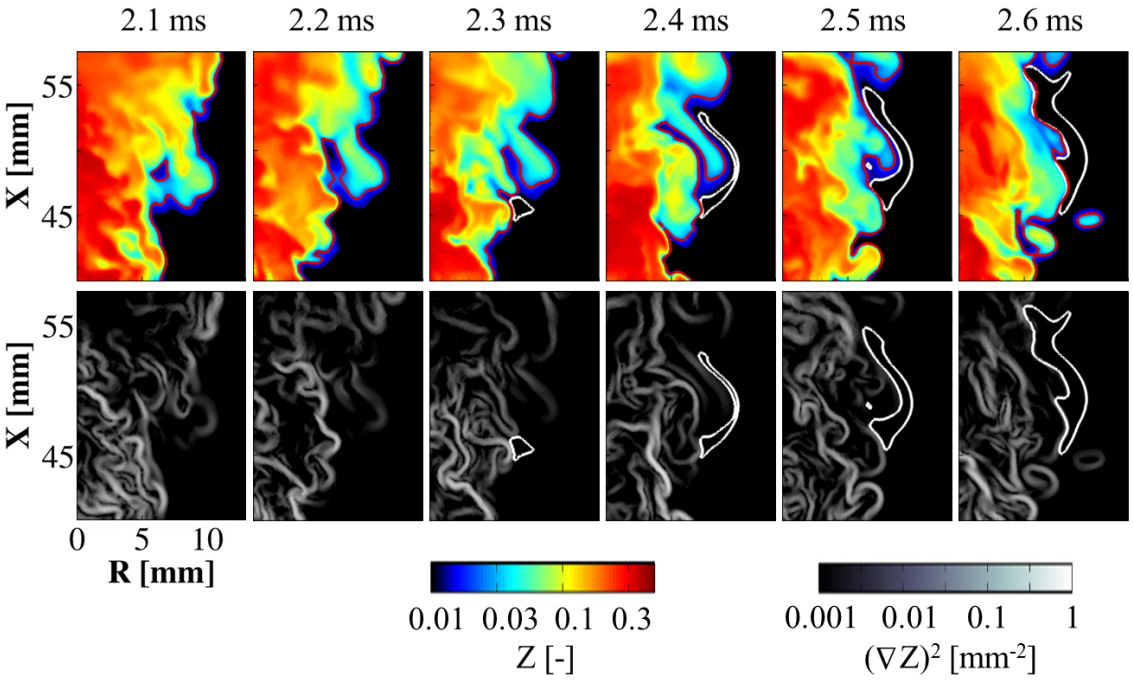

Figure 5.3.16: LES: Ignition sequence

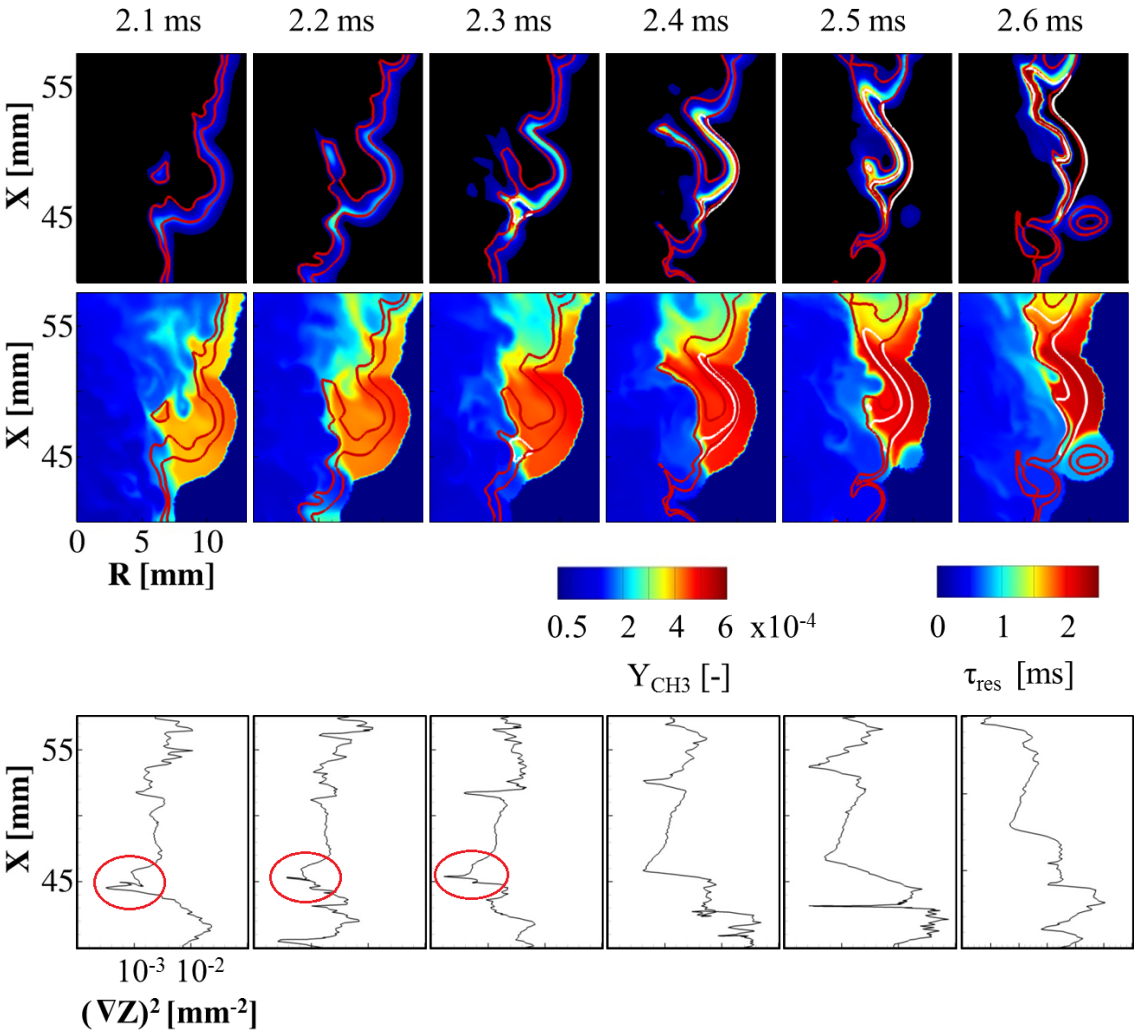

Figure 5.3.17: LES: Ignition sequence; 1st row: Mass fraction of methyl radical Y_{CH3}; 2nd row: Residence time τ_{res}; 3rd row: Squared mixture fraction gradient $(\nabla Z)^2$, Isolines: red lines $Z_{st} = 0.0297$ and $Z_{mr} = 0.005$, white line $T = 1560\,\mathrm{K}$; the location of the frame is indicated in figure 5.3.18

the maximum propagates towards the stoichiometric. And at 2.5 - 2.6 ms and $X = 55$ mm two separate flame fronts spread along Z_{st} and Z_{mr}.

In the last row of figure 5.3.17, the squared mixture fraction gradient $(\nabla Z)^2$ is plotted along the isoline of the most-reactive mixture fraction. It is obvious, that high methyl concentrations occur at locations with low mixture fraction gradients between $X = 44$ and 47 mm (2.1 - 2.3 ms). This demonstrates that small scale turbulent transport influences the ignition process, which was previously shown by various authors for more generic conditions [105, 70], such as turbulent mixing layers (section 2.3).

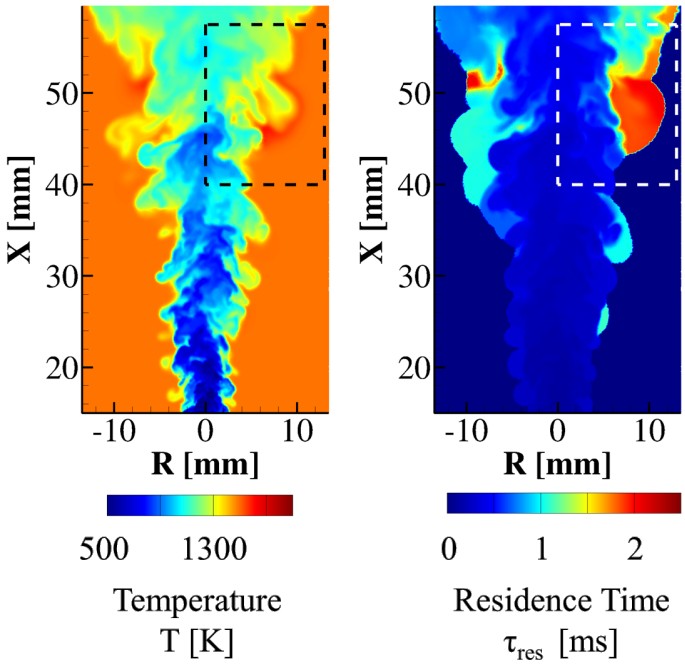

Figure 5.3.18: LES: Temperature and residence time, large view at 2.3 ms

The modeling of the residence time reveals the crucial mechanism for the large spatial scatter of the ignition location. The full view at ignition (2.3 ms) for the present example is shown in figure 5.3.18. In all observed ignition events, the ignition kernel location always coincides with very high residence time. It can be clearly seen in figure 5.3.17 that the radical pool builds up at the periphery of large-scale vortices. These large ring vortices are produced by high velocity gradients ($u_{cf} = 4$ m/s and $u_{jet} = 178$ m/s) close to the jet nozzle as described in section 2.4. They rapidly mix jet fluid and oxidizer and carry these well mixed fluid patches far into the slow coflow. After dissolution into smaller turbulent structures, the fluid patches are "trapped" in the coflow. Low scalar dissipation and long residence time at an almost constant location promote the build-up of radical pools and subsequent autoignition.

Conclusions

URANS and LES computations have been conducted for an atmospheric jet-in-crossflow experiment. It is shown, that a high LES resolution of the turbulent scales can be achieved ($\nu_t/\nu \leq 1$ in relevant region). The numerical results are validated with experimental data for the time-averaged mixture fraction and the OH number concentration. A satisfactory agreement is achieved. Uncertainties can mainly be related to the chemical reaction mechanism. The detailed analysis of the transient LES results reveals a multi-modal distribution for the temperature. Furthermore, it is found that ignition kernels evolve in large vortices at high residence time. The position of the most upstream kernels depend significantly on large turbulent structures. Therefore, the resolution of large-scale structures is fundamental for the accurate numerical prediction of the ignition scatter. It is also demonstrated that RANS methods are not able to capture these structures and the spatial distribution of the ignition locations.

6 Validation under Gas Turbine Operating Conditions

This chapter deals with the model validation under realistic operating conditions. Two test cases are presented, which where experimentally investigated by Fleck et al. [43, 46, 44, 45, 42] at the DLR high-pressure combustor test rig Stuttgart (HBKS). In the first test case, which is presented in section 6.1, the modeling capabilities of turbulent mixing modeling under gas turbine conditions are analyzed. The second test case is reported in section 6.2. It covers the model validation of the complete autoignition process, including turbulence, chemistry and their interaction. The scientific findings of the test cases under simplified conditions (chapter 5) are also used for the interpretation of the results under engine operating conditions.

6.1 Turbulent Mixing in a Jet-in-Crossflow

The first test case is focused on the analysis of turbulence modeling capabilities for jet-in-crossflow mixing under gas turbine operating conditions.

6.1.1 High Pressure Flow Experiment by Fleck et al.

First, the setup of the high pressure test rig is described in detail. An overview of the measured test conditions and system response quantities is provided in the subsequent sections.

6.1.1.1 Test Rig

Fleck et al. conducted measurements of diluted fuel jets in hot crossflow under high pressure conditions. The experimental test rig is presented in figure 6.1.1. A scheme of the general setup is provided in figure 6.1.2. The test rig was designed according to the reheat system of the staged Alstom gas turbine GT24/GT26 (more details in section 4.2.1). The high temperature crossflow is generated by a combination of electrical heating and combustion of natural gas in the hot gas generator. Before the gas enters the mixing section (MS), fresh dilution air is added to increase the oxygen content and to match the gas temperature and composition as expected for the gas turbine reheat combustor. The fuel jet is injected in the mixing section perpendicular to the crossflow. Fuel and shielding air (section 4.2.1) are

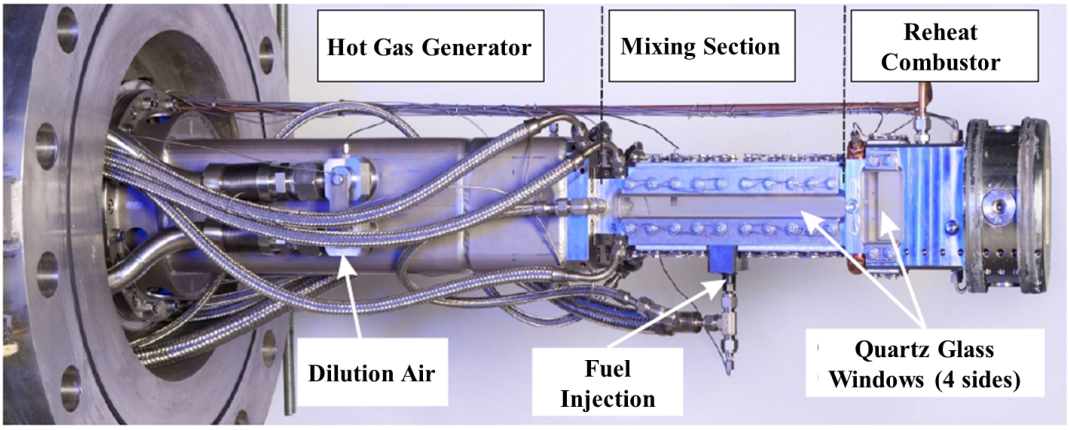

Figure 6.1.1: Experimental test rig [42]; flow from left to right

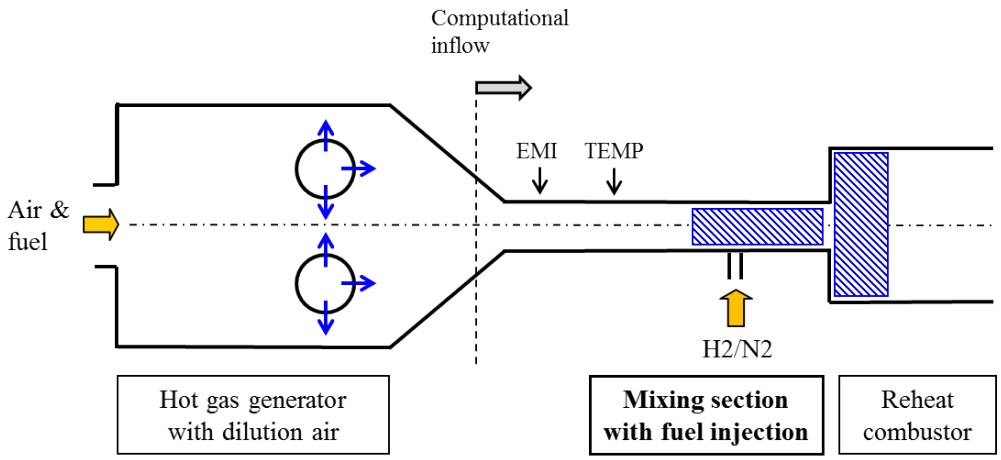

Figure 6.1.2: Scheme of experimental setup [46]

premixed in the present configuration. In accordance with the gas turbine system, a reheat combustion chamber is mounted downstream of the mixing section.

The combination of hot oxidizer and reactive fuel favors the occurrence of undesired premature autoignition in the mixing section. The analysis and computational modeling of the ignition processes are the central aspects of this work. The mixing section is a squared duct with a cross-sectional area of 25 x 25 mm and has a length of 100 mm from jet injection to the reheat chamber entrance. The round fuel pipe has a diameter of 5.6 mm and a length of 38 mm. Area contractions are places upstream of the channel and pipe duct. The fuel-crossflow mixing region is optically accessible through quartz glass windows within a height of ± 9 mm.

6.1.1.2 Test Conditions

Fleck et al. experimentally investigated a broad range of test parameters. Various fuel compositions were tested, nitrogen diluted hydrogen [46] as well as diluted hydrogen/natural gas blends [44]. The pressure was varied between 5 and 15 bar [45], different coflow temperatures were applied between 1173 and 1373 K and coflow velocities were varied between 200 and 300 m/s.

In the present work, only a small set of parameters is studied. The computational study on autoignition is focused on hydrogen/nitrogen fuel at a pressure of 15 bar and a crossflow velocity of 200 m/s. Compared to the generic test cases under atmospheric conditions, the Reynolds number is very high with $Re_{\mathrm{MS}} = 5 \cdot 10^5$. The hydrogen content was varied between 0 and 50 vol%. Dependent on the composition, the momentum ratio varied between $J = 2$ and 4. The full details of the reactive test case are provided in the next section.

Table 6.1: Inflow conditions for PIV test case ($J = 3.4$)

	$\dot{m}$ [g/s]	T [K]	ρ [kg/m^3]	X_{CH4} [-]	X_{H2} [-]	X_{N2} [-]	X_{O2} [-]	X_{H2O} [-]	X_{CO2} [-]
Crossflow	555.8	1186	4.3	0	0	0.769	0.150	0.054	0.027
Jet	61.2	313	9.9	0.39	0.05	0.56	0	0	0

For the experimental investigation of the turbulent mixing, Fleck [42] used a non-reacting fuel substitute. Additional methane was added to the fuel mixture to suppress autoignition in the premix section, but keeping the momentum ratio comparable to the reactive case. The respective test conditions for a momentum ratio of $J = 3.4$ are presented in table 6.1. The experimental reference data for the composition and temperature of the crossflow were measured by an intrusive emission probe (EMI) and a ceramic shielded thermocouple (TEMP) in the center of the mixing section, 180 mm and 104 mm upstream of the fuel injection (figure 6.1.2).

6.1.1.3 System Response Quantities

The velocity was measured by particle image velocimetry (PIV). Titanoxid particles with a size of about 1 μm were added to the dilution air in the hot gas generator. The measuring field had a spatial resolution of the 1.6 mm, which is quite coarse compared to the total window height of 18 mm. As noted by Fleck [42], high velocity gradients as they occur directly downstream of the fuel injection, might not be captured to the full extent.

The distributions of the average streamwise velocity and one instantaneous example are presented in figure 6.1.3. In the instantaneous picture, large structural velocity variations are visible. This is an important observation for the analysis of ignition and flame propagation, since these processes depend strongly on local and instantaneous conditions.

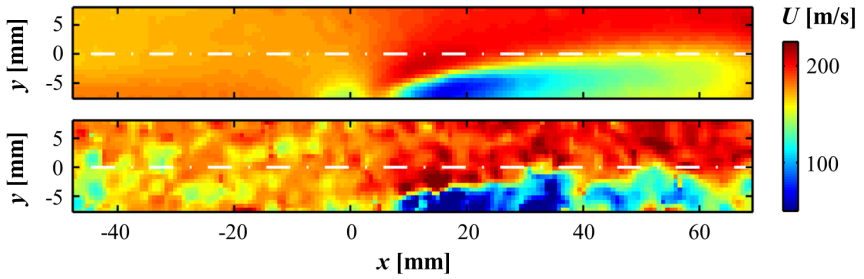

Figure 6.1.3: PIV measurements [42]: Average (top) and instantaneous (bottom) streamwise velocity in the plane of symmetry $z = 0\,\mathrm{mm}$

6.1.2 Numerical Simulation with Non-reacting CFD

Table 6.2: Grid specifications

	Grid Points [10^6]	Δx_{mix} [mm]	$\Delta x_{\mathrm{mix}}/D$ [-]	Time Step [s]	CPU time [h]	$\max(\nu_t/\nu)$ for $x < 25\,\mathrm{mm}$
SAS $\Delta x/D = 0.14$	1.3	0.8	0.14	$5{\cdot}10^{-7}$	100	ca. 450
LES $\Delta x/D = 0.02$	17.2	0.1	0.02	$5{\cdot}10^{-8}$	10600	50

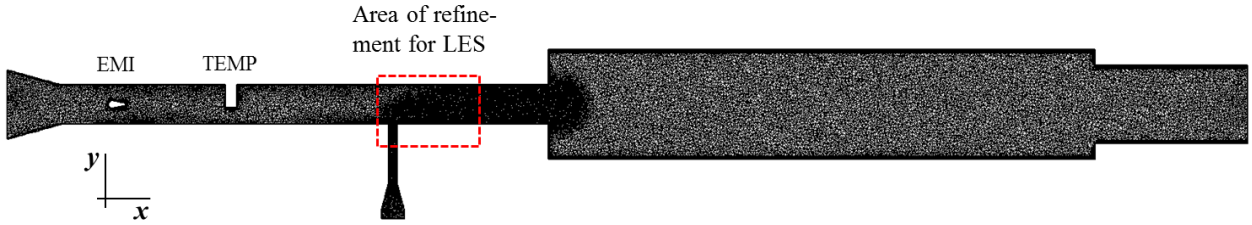

Figure 6.1.4: Computational grid for SAS

The selection of the computational methods is based on the findings from the generic test cases in capter 5. In the numerical study for autoignition in a turbulent jet (section 5.3), it was found that the instantaneous ignition locations depend mainly on large-scale turbulent structures at the outer periphery of the jet. Thus, the resulting spatial range of possible ignition locations can only be captured with scale-resolving methods, such as LES or SAS. RANS-methods can only provide information on the average ignition location. But in the present high pressure jet-in-crossflow configuration, the most-upstream ignition location is of special relevance for the occurrence of flame anchoring in the low-velocity region (sections 2.5 and 6.2.1.2). Therefore, scale-resolving turbulence models should be favored. However, very high Reynolds numbers in the order of $Re = 10^6$ are present under engine operating conditions. At such high turbulence levels, only relative coarse grid resolutions can be applied.

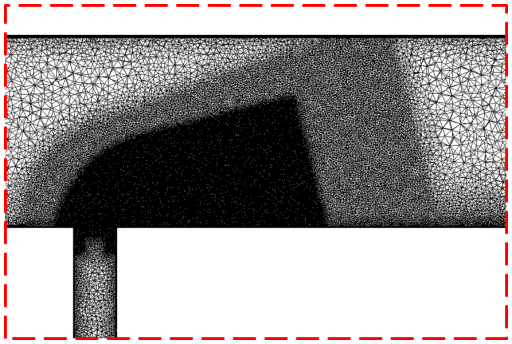

Figure 6.1.5: Grid refinement for LES; the detail is indicated by a red frame in figure 6.1.4

In section 5.2, the modeling capabilities of LES and SAS on very coarse grids were investigated for a generic jet-in-crossflow configuration. The study revealed that the SAS model should be favored above URANS modeling for similar resolutions. Furthermore, LES gives even better results, but more grid points are required for the resolution of the near-wall region.

Based on these findings, two different computational setups are applied. An overview of both setups is given in table 6.2. In the first setup "SAS $\Delta x/D = 0.14$", the SAS turbulence model is applied on a computational grid of about 1.4 million grid points and a spatial resolution of $\Delta x_{\mathrm{mix}} = 0.8\,\mathrm{mm}$. The computational cost is still within the limits to allow extensive parameter variations. Therefore this is a suitable setup for design studies in industrial application. The computational domain is shown in figure 6.1.4. It comprises the full mixing duct from the intersection to the hot gas generator at the inlet and the entrance into the reheat chamber at the outlet. Therefore, possible perturbations of the crossflow by the emission and temperature probes upstream of the jet injection are included. The detailed dimensions of the geometry are given in section 6.1.1.1.

In the second setup "LES $\Delta x/D = 0.02$", high fidelity LES is used on a finer grid. Thus, the grid was refined to $\Delta x_{\mathrm{mix}} = 0.1\,\mathrm{mm}$ in the relevant region for ignition and flame stabilization processes ($x = 0$ - $25\,\mathrm{mm}$). Although, the computational cost of this LES (17 million grid points) already exceeds industrial requirements, the grid is still too coarse to permit ultimate conclusions. Nevertheless, valuable information on tendencies for quality and influence of turbulence resolution can be obtained.

In both setups, a CFL number of 0.2 is applied. At larger time step sizes, non-physical artificial energy production occurs in the periphery in the shear layer vortices due to large local gradients. The averaged results were taken over an integration time of 10 mixing region residence times. The species mixing modeling is based on the gradient diffusion hypothesis. The turbulent diffusivities are derived from the thermal diffusivity by assuming $Sc_{\mathrm{t}} = Pr_{\mathrm{t}}$ (section 3.1).

The inflow streams are specified by the experimentally measured mass fluxes and top-hat velocity profiles. The channel walls are actively cooled in the experiment. The total heat flux are estimated by the measured temperature rise of the coolant flows (water and air). The specification of the boundary conditions was varied within the experimental uncertainties (Prause et al. [147, 150, 151]). It was found, that there is only a minor sensitivity of autoignition on the wall temperature. In the present test case, an isothermal boundary condition at $T_{\text{wall}} = 1100\,\text{K}$ is applied. Thereby, the correct heat flux through the walls is employed. Adiabatic conditions are applied for the temperature probe and the fuel pipe.

6.1.3 Validation of Turbulence Modeling

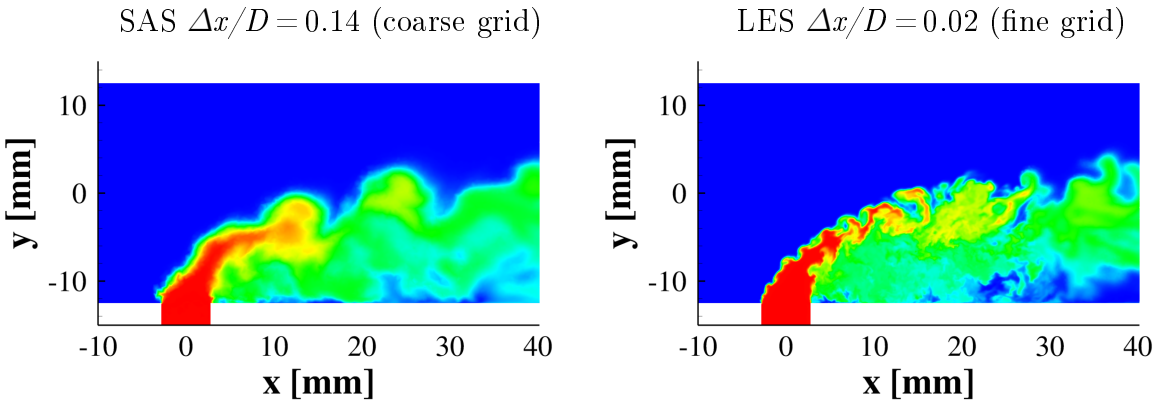

Figure 6.1.6: Instantaneous mixture fraction

Compared to the generic jet-in-crossflow test case at atmospheric pressure (section 5.2), the present data under high pressure conditions is less detailed. As described above, the experimental velocity measurements do not cover the near-wall region and the resolution of the measuring field is comparably coarse. Furthermore, the numerical resolution is also limited due to the high Reynolds number. To supplement the present data under high pressure conditions, the results are also compared to the findings from the atmospheric jet-in-crossflow test case, which was conducted at a similar momentum ratio ($J = 4$). Since the characteristics of a jet-in-crossflow are primarily dependent on the momentum ratio [84, 122], the velocity and mixture fields are comparable to the present high pressure test case. However, at atmospheric pressure, a reduced Reynolds number ($Re = 8 \cdot 10^4$) and better experimental accessibility facilitated more detailed measurements and a higher numerical resolution.
The experimental and numerical results under high pressure conditions (6.1) are presented in figures 6.1.7 and 6.1.8. The profiles are plotted along the channel height y at different streamwise locations x with intervals of $x = 10\,\text{mm}$ (at lower x-axis). The magnitudes of the specific quantities are indicated at the upper x-axis. The velocity components are compared

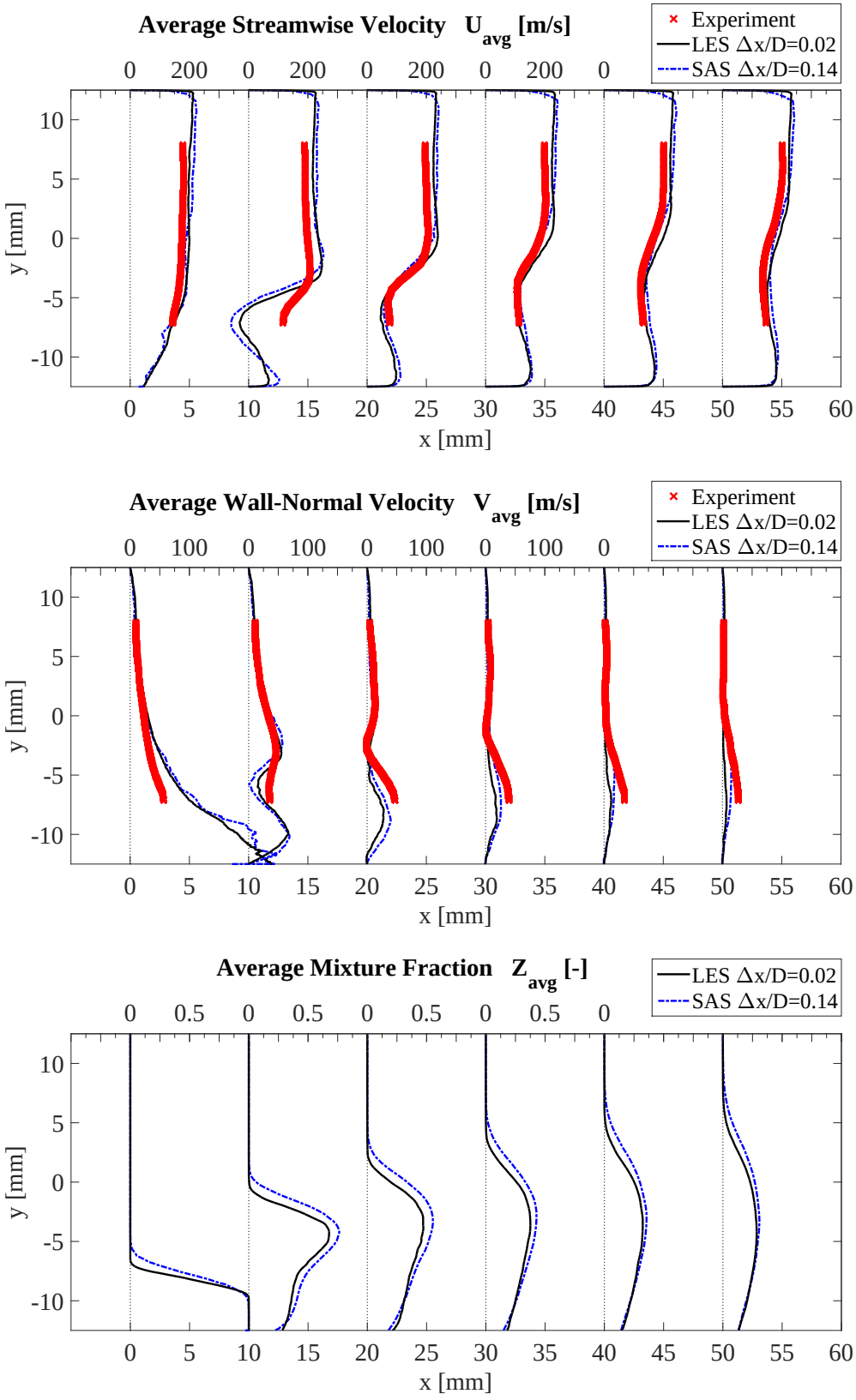

Figure 6.1.7: Average Velocity and Mixture Fields

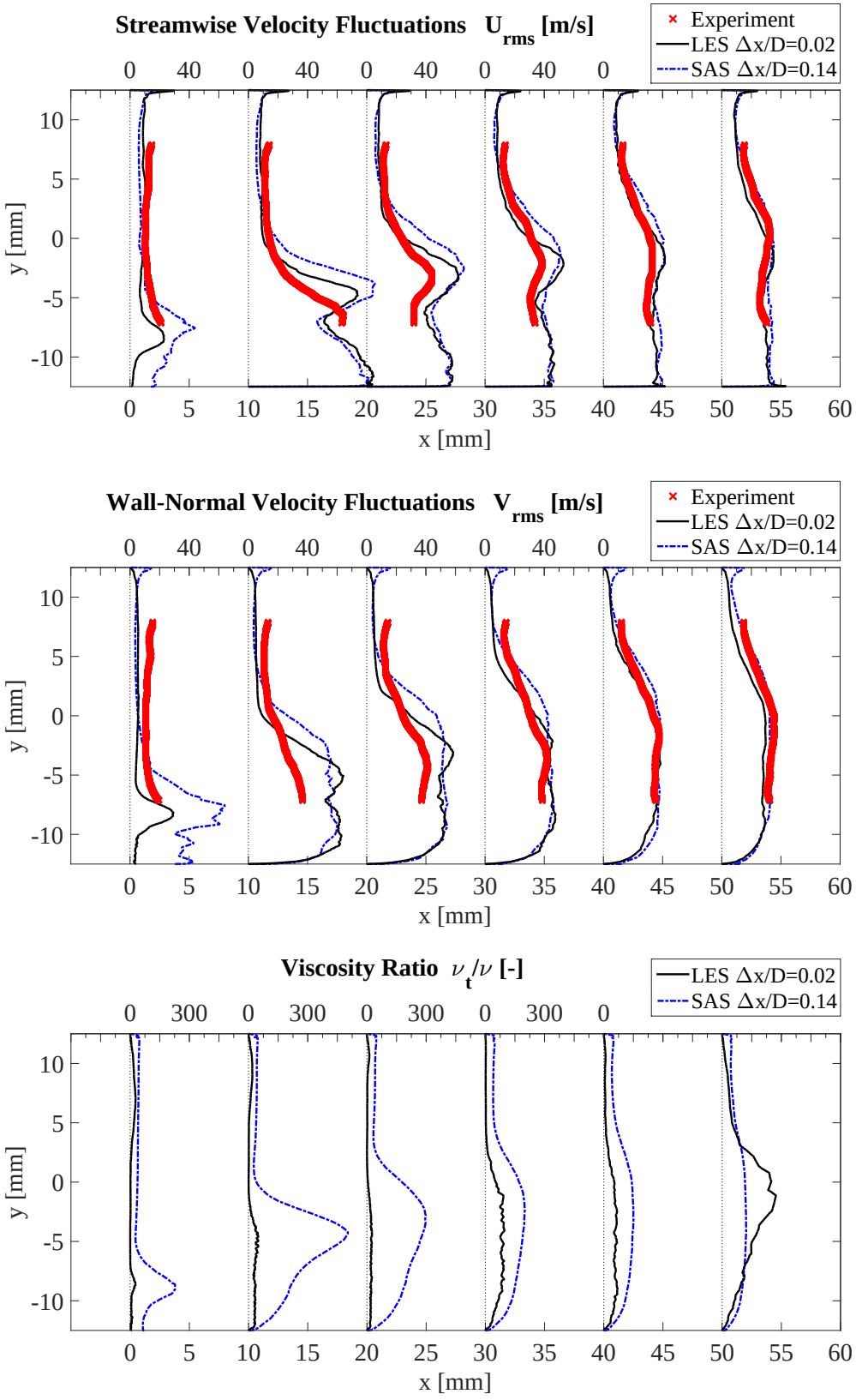

Figure 6.1.8: Velocity Fluctuations and Viscosity Ratio

with experimental data for the plane of symmetry ($z = 0\,\mathrm{mm}$) in the first two figures. In general, a satisfactory agreement can be achieved under engine conditions with both, SAS and LES. However in figure 6.1.7 (top image) at $x = 10\,\mathrm{mm}$ ($x/D \approx 2$), negative streamwise velocities and therefore a reverse flow are predicted by the numerical simulation, which was not observed in the experiment. Also the streamwise velocity gradient $\mathrm{d}u/\mathrm{d}y$ is much smaller compared to the PIV measurements. As explained already by Fleck [42], these potentially high velocity gradients might not be fully captured by the PIV measurements due to the limited spatial resolution. Comparative information can be gained from the atmospheric jet-in-crossflow experiment (section 5.2), which was conducted at similar momentum ratio. The measurements by Lischer [97] actually indicate higher gradients and negative velocities in this region. Therefore it can be assumed that the deviation in this region can be related to measurement inaccuracies.

The results of SAS and LES are very similar with only minor differences between the two setups. First, there is some deviation of up to 30 % in the average streamwise velocity u_{avg} in the near-wall recirculation region ($x \approx 10$ and $y <$ -10 mm). Second, the profiles of velocity fluctuations u_{rms}, v_{rms} and mixture fractions in the upper jet shear layer indicate a higher jet trajectory of the SAS solution compared to the LES case.

An indication of the turbulence resolution is given in figure 6.1.8 by the viscosity ratio. In the coarse SAS, the maximum viscosity ratio is about $(\nu_{\mathrm{t}}/\nu)_{\mathrm{SAS,max}} \approx 450$. The maximum value for the LES in the refined region ($x < 25\,\mathrm{mm}$) is much smaller: $(\nu_{\mathrm{t}}/\nu)_{\mathrm{LES,max}} \approx 50$. However, this is still a very high value for scale-resolving turbulence modeling, indicating limited resolution of smaller turbulent scales. Unfortunately, due to high computational cost, a higher grid resolution is not feasible under the present test conditions, especially for the more complex reacting flow (section 6.2).

More information on influence of grid resolution can be gained from the study of the atmospheric jet-in-crossflow (section 5.2). The resolution quality of the high pressure simulations corresponds to the atmospheric simulations on grid CN02 (table 5.4: $(\nu_{\mathrm{t}}/\nu)_{\mathrm{LES,CN02}} \approx 60$ and $(\nu_{\mathrm{t}}/\nu)_{\mathrm{SAS,CN02}} \approx 540$). The generic study shows, that the mean flow quantities can be reproduced well with such a coarse resolution. However, the periodic shear layer vortices, which are produced in the pipe can only be captured with a wall resolution of $\Delta \mathrm{x}_1^+ \approx 1$, which is not feasible at reasonable computational cost for the present Reynolds number between $Re = 5 \cdot 10^5$ and 10^6 (tab. 6.5) [55, 140]. Furthermore, the streamwise velocity in the near-wall region is overestimated. This is of relevance for the accurate prediction of the flame anchoring process.

Conclusions

The computational simulation can reproduce the turbulent mixing within the experimental measurement accuracy. Very similar results are obtained with coarse SAS and refined LES. However, the large-scale shear layer vortices, which are produced due to instabilities in the pipe exit, cannot be reproduced with both computational setups due to insufficient grid resolution. Finally, the numerical simulations reveal negative streamwise velocities in the leeward side of the jet. These are of special importance for the flame stabilization mechanism, which is investigated in the next section.

6.2 Turbulent Autoignition in a Jet-in-Crossflow

In the final test case, the predictive capability of different approaches for autoignition modeling are analyzed and quantified for gas turbine operating conditions.

6.2.1 High Pressure Autoignition Experiment by Fleck et al.

The test rig and general test conditions are already described in sec. 6.1.1.1 and 6.1.1.2. In the present section, only specific test conditions (sec. 6.2.1.1) and system response quantities (section 6.2.1.2) are described, which are relevant for the analysis of the reactive test case.

6.2.1.1 Test Conditions

The present analysis is focused on the results, which were obtained at a pressure of 15 bar, crossflow velocities of 200 m/s and for premixed H_2/N_2 fuel mixtures. In the autoignition experiments, the fuel hydrogen concentration was varied between 0 and 50 vol%. The nitrogen mass flow was set to a constant value of 61.0 g/s. The hydrogen mass flow was increased stepwise. The resulting momentum ratio varied between $J = 2$ for pure nitrogen and $J = 4$ for the target hydrogen concentration of 50 vol%. Furthermore, the hot gas temperature was varied between 1130 K and 1240 K.

When the experimental and numerical results are compared quantitatively, additional information on the uncertainties of the test conditions is required, since any inaccuracy in the boundary conditions can have a direct effect on the accuracy of the computational simulation (see also: theoretical background on validation in chapter 4). Therefore, a detailed sensitivity study under gas turbine operating conditions was conducted (Prause et al. [151]). It was found that the most relevant source of input uncertainty for the numerical simulation is the hot crossflow temperature. As shown for the homogeneous system in section 5.1, autoignition is very sensitive on temperature variations. Small measurement uncertainties in the range of 2 % can alter the ignition delay time by a factor of 2. Therefore, in the present test case, the uncertainties in temperature measurements must be assessed as accurate as possible.

A comprehensive evaluation of the hot crossflow temperature is presented in the following paragraph.

Crossflow Temperature During the autoignition test campaign, the hot gas temperature was determined by a ceramic shielded thermocouple in the center of the mixing duct (figure 6.1.2). The measurements had a tolerance of $\pm 0.6\,\%$ and a relative standard deviation of $1\,\%$ ($\pm 12\,\mathrm{K}$). However, the temporal response of the thermocouple is in the order of $0.1\,\mathrm{s}$. This is a very large time interval compared to the fuel residence time of about $0.5\,\mathrm{ms}$ within the mixing duct.

Table 6.3: Flow conditions in hot gas generator

	$\dot{m}$ [g/s]	T [K]	X_{N2} [-]	X_{O2} [-]	X_{H2O} [-]	X_{CO2} [-]
Exhaust	348	1660	0.755	0.113	0.087	0.044
Dilution Air	207	303	0.790	0.210	0	0

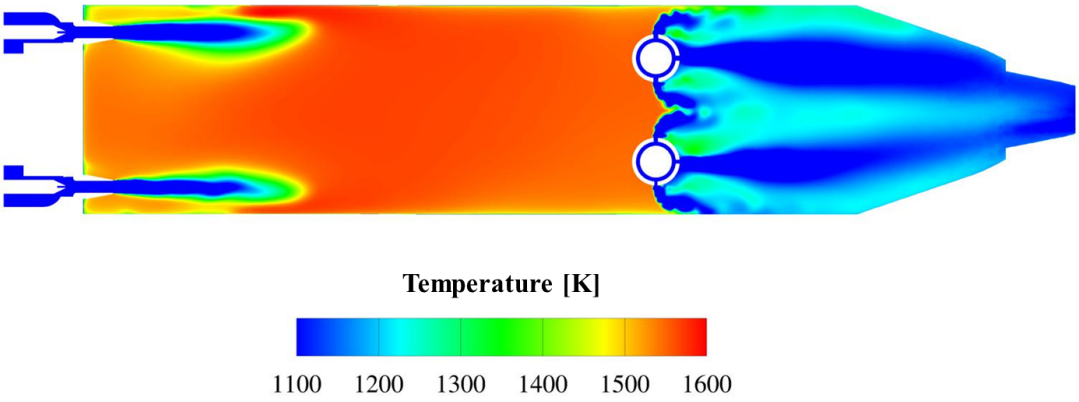

Figure 6.2.1: Simulated temperature distribution in the hot gas generator upstream of the mixing section (URANS)

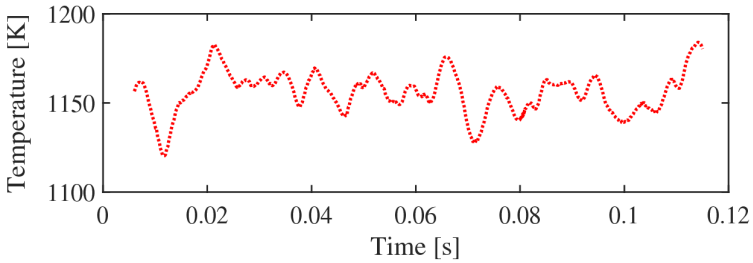

Figure 6.2.2: Simulated temperature evolution at the intersection between hot gas generator outlet and mixing section inlet

High-frequency temperature fluctuations might be introduced in the upstream hot gas generator by the admixture of fresh dilution air through air flutes. A URANS study of the hot gas generator indicates that significant unmixedness persist in the fuel mixing section [151]. The properties of the two inflow streams are presented in table 6.3 (the resulting mixture composition is given in table 6.5). The simulation results show considerable temperature fluctuations at the inlet of the mixing channel (figures 6.2.1 and 6.2.2). These high-frequency fluctuations in the millisecond range cannot be resolved by the thermocouple, but are of significant influence on autoignition characteristics (section 6.2.3).
Due to the high sensitivity of autoignition to temperature, an accurate information of these temperature variations is required. But URANS simulation cannot provide reliable quantitative information for this highly unstable turbulent mixing process and better suited simulations, such as LES would exceed the computational capacities due to the high Reynolds numbers of this test case. Therefore, additional laser-Raman measurements with high spatial and temporal resolution were conducted for the detection and determination of temperature fluctuations. A detailed description of the measurement campaign is given in Ax [11]. Raman spectroscopy enables the simultaneous measurement of the major species concentrations such as N_2 and H_2O.

$$I_\alpha = I_{\text{Laser}} \frac{X_\alpha}{T} C_\alpha \tag{6.2.1}$$

The scattering signal I_α depends mainly on the initial laser beam intensity I_{Laser}, the temperature, the mole fraction of the respective species α and the proportionality factor C_α for species α.
Several measurement series were conducted for various conditions in the mixing duct. The data of an exemplary series is presented in figure 6.2.3. 1000 instantaneous spectra were evaluated for each series with a temporal resolution of 350 ns at a repetition rate of 10 Hz. The relative standard deviations for this series are $\sigma_{I_{\text{N2}}} = 5.0\,\%$ for the nitrogen signal and $\sigma_{I_{\text{H2O}}} = 6.6\,\%$ for the water signal. These variations are partially composed of inherent uncertainties of the Raman measurement technique, but also possible fluctuations of the temperature or the mixture. The different influence parameters are discussed below. Special difficulties needed to be overcome during the measurement campaign due to the demanding application-oriented test conditions.

- One challenge is the small extension of the measurement section. In Raman spectroscopy, a very high laser intensity is required to get a sufficient signal to noise ratio. But the laser intensity is limited by the window resistance. The local laser impact at the window surface can be reduced by broadening of the laser beam. However, this

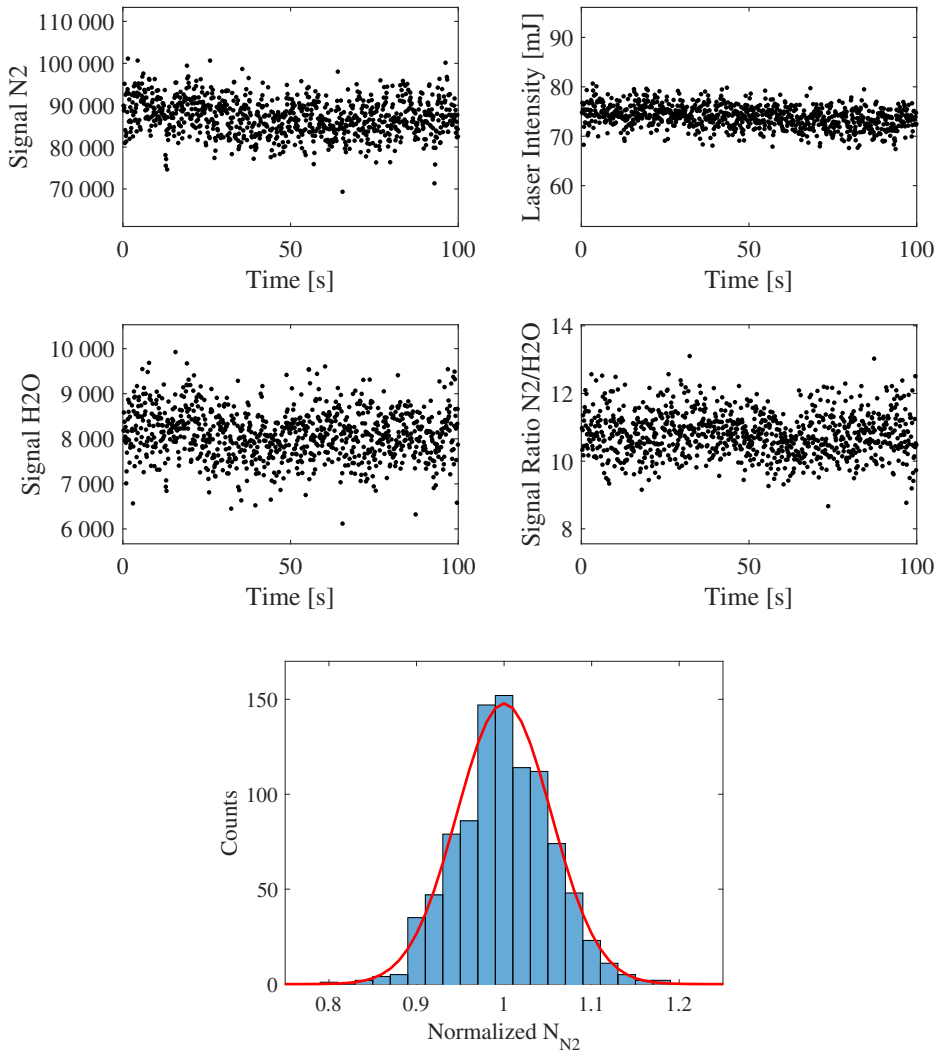

Figure 6.2.3: Example of measurement series number 17

is very limited in the present test case configuration, since the distance between the window and the focal point at the measurement location amounts to 12.5 mm only. The limitation in the applicable laser intensity also results in a low signal-to-noise ratio for the present test case.

- Usually, in Raman spectroscopy, the measurement-related errors are estimated by reference measurements under known benchmark conditions. But in the present test configuration, such a reference measurement cannot be provided for the water signal. Therefore, the measurement-related fluctuations must be estimated from theoretical considerations.

- Under engine operating conditions ($p = 15\,\mathrm{bar}$), large-scale pressure oscillation in the order of $\sigma_\mathrm{p} = 1.0\,\%$ were present in the test rig.
- Furthermore, the measurements are subject to photon statistics. Under the relevant conditions, a relative fluctuation of $\sigma_\mathrm{Ph,N2} = 2.3\,\%$ was estimated for the nitrogen signal and $\sigma_\mathrm{Ph,H2O} = 4.4\,\%$ for the water signal.

Table 6.4: Relative standard deviations of Raman measurements in the vicinity of the jet-crossflow interface ($Z = 0\,\mathrm{mm}$ and $p = 15\,\mathrm{bar}$ for all series)

Series Number	T [K]	X [mm]	Y [mm]	σ_{I_N2} [-]	σ_{I_H2O} [-]	$\sigma_{I_\mathrm{N2}/I_\mathrm{H2O}}$ [-]	$\sigma_{I_\mathrm{Laser}}$ [-]	$\sigma_{X_\mathrm{N2}/T}$ [-]	$\sigma_{X_\mathrm{N2}/X_\mathrm{H2O}}$ [-]
11	1174	-113	0	0.061	0.078	0.061	0.044	0.034	0.035
12	1176	-113	-4	0.053	0.071	0.062	0.036	0.030	0.037
13	1183	-113	4	0.062	0.083	0.061	0.052	0.023	0.035
14	1181	-83	0	0.073	0.093	0.068	0.061	0.031	0.046
15	1184	-63	0	0.050	0.067	0.060	0.032	0.029	0.033
16	1187	-63	-4	0.051	0.071	0.065	0.037	0.025	0.042
17	1186	-63	4	0.050	0.066	0.059	0.030	0.031	0.031
20	1183	-9	4	0.050	0.066	0.056	0.037	0.022	0.025

In table 6.4 the relative standard deviations are presented for the measurement series, which were conducted under baseline conditions ($p = 15\,\mathrm{bar}$) in the vicinity of the jet-crossflow interface ($X \geq$ -113 mm). The measured signals vary for nitrogen between $\sigma_{I_\mathrm{N2}} = 5.0$ and 7.3 % and for water between $\sigma_{I_\mathrm{H2O}} = 6.6$ and 9.3 %.

$$\sigma_{X_\mathrm{N2}/T} = \sqrt{\sigma_{I_\mathrm{N2}}^2 - \sigma_{I_\mathrm{Laser}}^2 - \sigma_\mathrm{Ph,N2}^2 - \sigma_p^2} \tag{6.2.2}$$

$$\sigma_{X_\mathrm{N2}/X_\mathrm{H2O}} = \sqrt{\sigma_{I_\mathrm{N2}/I_\mathrm{H2O}}^2 - \sigma_\mathrm{Ph,N2}^2 - \sigma_\mathrm{Ph,H2O}^2} \tag{6.2.3}$$

The nitrogen signal $\sigma_{X_\mathrm{N2}/T}$ is evaluated by the Gaussian error propagation rule. The measurement-related fluctuations from photon statistics $\sigma_\mathrm{Ph,N2}$, laser signal $\sigma_{I_\mathrm{Laser}}$ and pressure fluctuations σ_p are considered in this analysis (equation 6.2.2). Statistical independence is assumed. The average of the resulting relative standard deviation is $\sigma_{X_\mathrm{N2}/T} = 2.8\,\%$. In this range, the variation of the nitrogen concentration is negligible compared to the temperature change. If it is assumed that this variation originates from mixture inhomogeneities, the remaining variation is directly proportional to the temperature fluctuation ($\sigma_T \approx \sigma_{X_\mathrm{N2}/T}$).
To support this theoretically derived estimation, a second analysis method is applied: By evaluating the ratio of the nitrogen and water signal, the influence of temperature, pressure and laser fluctuations are canceled out. The signal ratio has a relative standard deviation

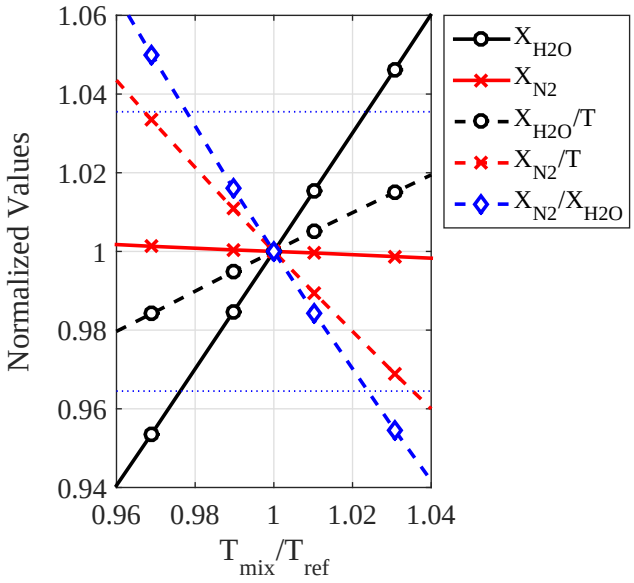

Figure 6.2.4: Calculated sensitivities

between $\sigma_{I_{N2}/I_{H2O}} = 5.6$ and 6.8 %. Only the photon statistics must be considered to get the purely mixture-related fluctuations (equation 6.2.3). The resulting average for the relative standard deviation is $\sigma_{X_{N2}/X_{H2O}} = 3.6$ % (table 6.4). Finally, it must be considered, that the water concentration is much more sensitive to mixture variations than to the temperature. The relative sensitivities of the relevant quantities were calculated with Cantera [62]. The average relative standard deviation of $\sigma_{X_{N2}/X_{H2O}} = 4.6$ % (table 6.4) can be related to a temperature variation of $\sigma_T = 2.4$ %. This result is quite similar to the previous estimation from the nitrogen signal.

The remaining standard deviation of $\sigma_T = 2.4$ - 2.8 % might originate from mixture inhomogeneities. However, due to the limited laser intensity, additional experimental uncertainty sources can not be fully excluded. Nevertheless, through this comprehensive measurement study, it can be verified that the relative standard deviation of the crossflow temperature is below 2.8 %.

6.2.1.2 System Response Quantities: Ignition Locations and Flame Anchoring

The experimental data by Fleck et al. [43, 46, 44, 45, 42] is reviewed in this section to identify appropriate system response quantities (chapter 4), which are suitable for a quantitative comparison with numerical results.

In the experiment, autoignition is monitored by broadband luminescence measurements within the mixing section. At a temperature of 1175 K and a hydrogen fuel content of $X_{H2} = 0.25$, two different ignition phenomena can be observed. Examples for both cases are

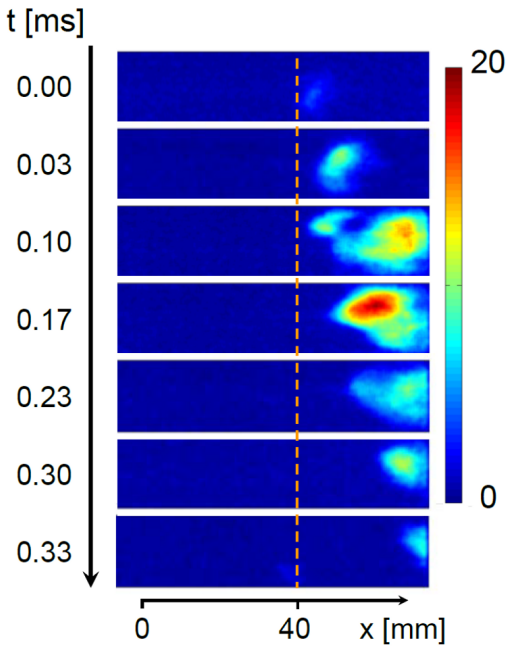

Figure 6.2.5: Non-stabilizing ignition kernel; broadband luminescence signal; first time detection at 40 mm [46]

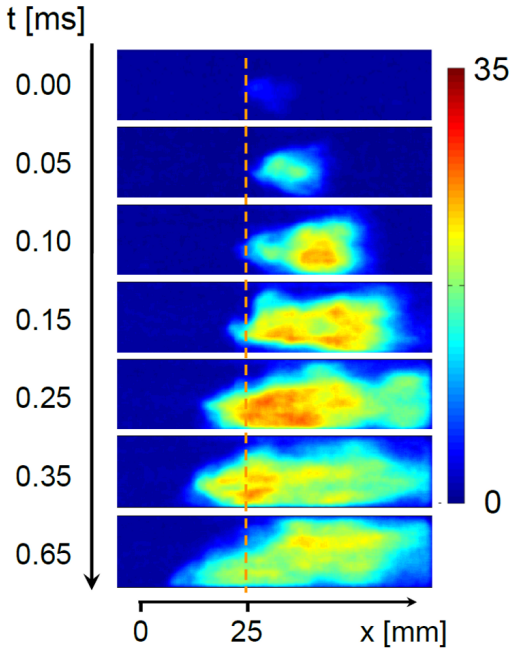

Figure 6.2.6: Stabilizing ignition kernel; broadband luminescence signal; first time detection at 25 mm [46]

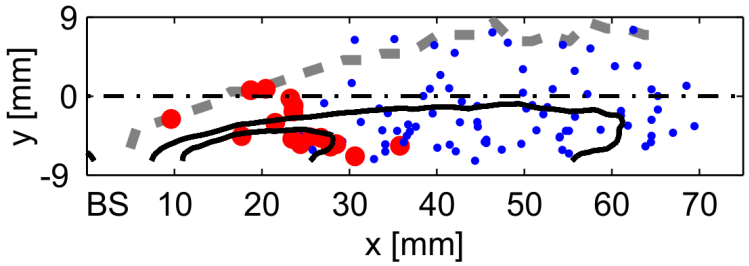

Figure 6.2.7: Position, where kernels were detected for the first time [42]; small blue dots: non-stabilizing kernels; big red dots: stabilizing ignition kernels; grey dashed line: trajectory of maximum velocity; black continuous lines: isolines for mean streamwise velocities at 100 and 150 m/s

shown in figures 6.2.5 and 6.2.6. As described in section 6.1.3, the mixing channel has a height of 25 mm of which only 18 mm are optically accessible. The near-wall region is not visible. The perpendicular fuel injection is located at the axis origin ($x = 0$ mm). In all test runs, ignition was initiated by self-accelerating chemical reactions. No external ignition source was applied. The sequence in figure 6.2.5 shows a non-stabilizing ignition event. The ignition kernel appears quite late at a streamwise location of $x = 40$ mm. While this kernel spreads and gains intensity with time, it is transported downstream by the flow until it leaves the mixing section. In figure 6.2.6, a kernel emerges further upstream at about $x = 25$ mm. This kernel is also transported downstream, but propagates also upstream towards the fuel injection. A steady stable flame establishes on the lee-ward side of the jet.

Under the respective test conditions ($T_{\mathrm{HG}} = 1175$ K and $X_{\mathrm{H2}} = 0.25$), a total of 18 independent test runs were conducted. For all kernels, which appeared during these runs, the locations of first time detection are mapped in figure 6.2.7. During a single test run, numerous ignition kernels can be observed. The ignition locations vary widely in horizontal and vertical direction. Kernels, which first appeared downstream of about $x \approx 25$ - 35 mm were transported out of the mixing section similar to the example in figure 6.2.5 (left sequence). These non-stabilizing ignition kernels are indicated by the small blue symbols in figure 6.2.7. Finally, when a kernel appeared close to the low velocity region upstream of $x = 25$ mm, it evolved in a similar manner as the kernel in figure 6.2.6 (right sequence). In contrast to the non-stabilizing kernels, the stabilizing kernels propagated upstream and led to a stable steady flame in the mixing section. Fleck et al. [46] presumed, that these stabilizing ignition kernels occurred in a region of low velocity (figure 6.1.7). Either, the flame speed exceeds the local flow velocity or the kernels are even transported upstream by reverse flow.

The distribution of ignition kernel locations for a specific set of test conditions provides valuable insight into the ignition and flame stabilization characteristics. However, due to the broad scatter of ignition locations, it is not suited for a quantitative validation.

In a subsequent study, the crossflow temperature in the mixing section was varied between 1130 K and 1240 K. The crossflow temperature was kept constant during a single test run, while the hydrogen concentration was increased stepwise until a stabilizing ignition event with subsequent flame anchoring occurred in the mixing section. The determined flame anchoring limits are presented in figure 6.2.8. These limits of critical hydrogen concentration vs. temperature are suitable for the quantitative validation with numerical results.

6.2.2 Numerical Simulation with SAS/LES and A-PDF Approach

The setup of the numerical grids, turbulence and mixing models as well as boundary conditions are almost identical to the non-reacting test case in section 6.1. Some parameters,

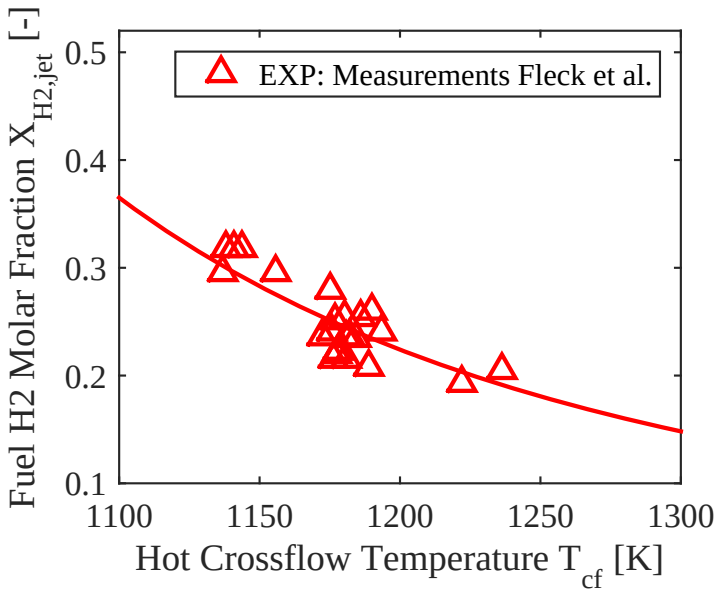

Figure 6.2.8: Flame anchoring limits [42]

Table 6.5: Flow conditions in the mixing section for numerical reference conditions ($J = 3.2$). The compositions are given in mole fraction.

	$\dot{m}$ [g/s]	T [K]	ρ [kg/m^3]	u [m/s]	Re [-]	X_{H2} [-]	X_{N2} [-]	X_{O2} [-]	X_{H2O} [-]	X_{CO2} [-]
Crossflow	555.8	1268	4.3	207	$5{\cdot}10^5$	0	0.769	0.150	0.054	0.027
Jet	63.2	313	11.2	230	$1{\cdot}10^6$	0.330	0.670	0	0	0

such as hot crossflow temperature and hydrogen content of the fuel jet were varied in accordance to the experimental test conditions. The majority of these parameter variations were conducted with the cost-efficient SAS setup (section 6.2.3 to 6.2.5.2). Only a small selection of simulations, which is presented in section 6.2.5.2 was performed with LES on the refined grid.

In addition to the setup of the non-reacting test case in section 6.1, supplemental models for chemical reaction and TCI are required. The chemical reaction is described by the detailed kinetic mechanism of Ó Conaire [135], considering 9 species and 21 reactions. The turbulence-chemistry interaction is modeled by assumed joint probability density functions (A-PDF) for temperature and species. Detailed model descriptions are provided in section 3.2.3.

Special attention must be paid on the accurate definition of chemical and thermal inflow conditions at the crossflow inlet. The hot gas composition is determined experimentally by an emission probe, which is located 180 mm upstream of the fuel injection (figure 6.1.2). The reference composition is given in table 6.5. The concentration of minor species such as hydroxyl and hydrogen radicals were not quantified experimentally. Although, the inflow

concentration of these intermediate species as well as variations in oxygen and water concentration might affect the autoignition process (section 2.4). However, a detailed sensitivity study by Prause et al. [151] showed, that the effect of composition variations is negligible. But it was found that small variations in the hot gas temperature have a significant effect on autoignition. Therefore, the impact of the temperature fluctuations is analyzed in detail in sections 6.2.3 to 6.2.5.2.

6.2.3 Analysis of Transient Ignition Process

In a first setup, a moderate temperature variation of $\pm 40\,\mathrm{K}$ is applied. The results are presented in figure 6.2.9. The corresponding temperature profile at the top image was monitored at the jet inflow location ($[x\ y\ z]$=[0 0 0], indicated for $t = 0.00\,\mathrm{ms}$ in figure 6.2.9). In accordance with the experiments (figures 6.2.5 and 6.2.6), the temporal origin ($t = 0\,\mathrm{ms}$) corresponds to the first detection of the ignition kernel. For comparison with the broadband luminosity, the hydroxyl mass fraction is integrated in z-direction. The ignition kernel can be detected for the first time at a location of about 40 mm. Similar to the non-stabilizing measurement example in figure 6.2.5, the kernel spreads and is transported downstream by the mean flow.

In a second setup, a higher temperature variation of $\pm 60\,\mathrm{K}$ is applied. In this example (figure 6.2.10), the kernel appears further upstream at about 20 mm. In contrast to the previous case, this ignition event leads to a stable steady flame within the mixing section. This example corresponds to the phenomena of the stabilizing ignition kernel in figure 6.2.6.

These two example show, that the ignition phenomena, which were observed in the experiments can be very good reproduced with numerical simulation. Furthermore it is demonstrated that the temperature fluctuations in the hot crossflow have a significant influence on the ignition location (see also figure 6.2.12) and subsequent flame characteristics.

The numerical simulation also provides additional insight into the ignition and flame stabilization process. In the sequence in figure 6.2.11, three different instantaneous quantities are plotted at the plane of symmetry ($z = 0\,\mathrm{mm}$): temperature, streamwise velocity and hydrogen radical concentration. When the ignition kernel is observed for the first time at $t = 0\,\mathrm{ms}$, only a very small temperature rise can be detected at the plane of symmetry $z = 0$ (left image in the first row). However, there is already a significant amount of hydrogen radicals (right image) at the interface between fuel jet and hot crossflow. Prior to thermal runaway, these precursor species are accumulated on the lean side of the mixing layer. The stoichiometric mixture fraction is indicated by the red dotted line.

When a significant temperature rise at $t = 0.03\,\mathrm{ms}$ leads to ignition through thermal runaway

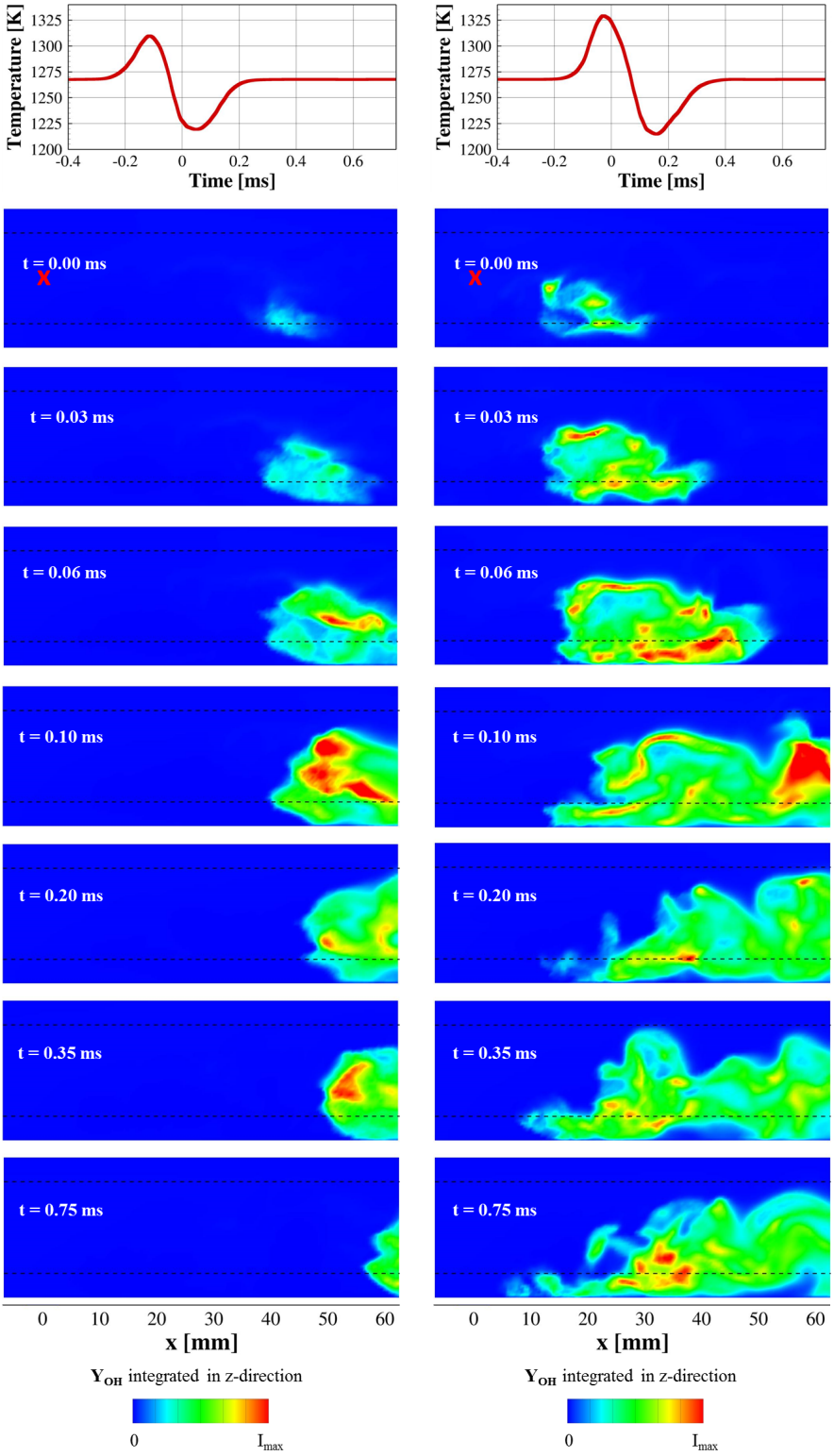

Figure 6.2.9: Non-stabilizing ignition kernel; temperature peak of $\pm 40\,\mathrm{K}$; temperature monitored at red x; first time detection of the kernel at 40 mm

Figure 6.2.10: Stabilizing ignition kernel; temperature peak of $\pm 60\,\mathrm{K}$; temperature monitored at red x; first time detection of the kernel at 20 mm

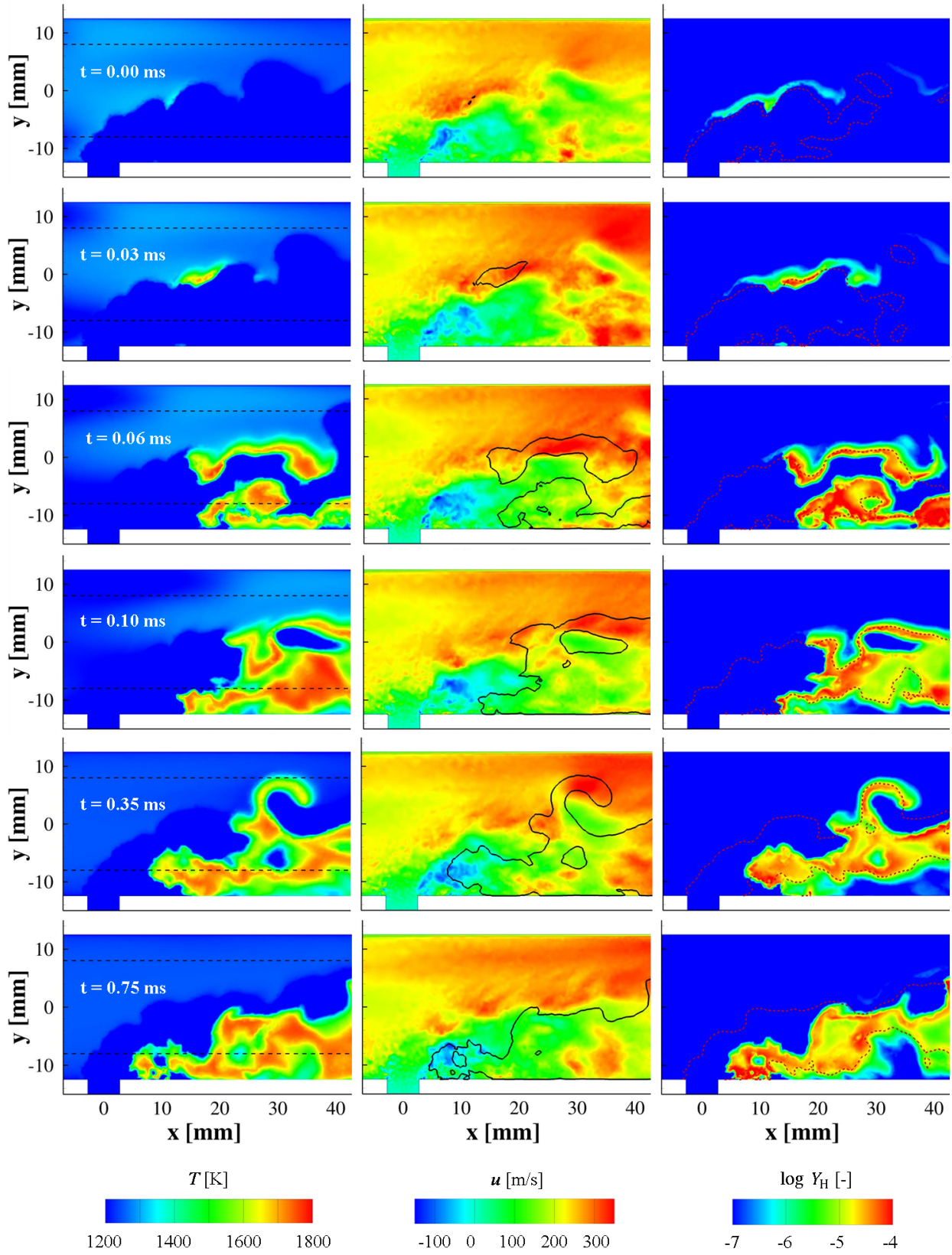

Figure 6.2.11: Flame anchoring process; left: instantaneous distributions for temperature; middle: streamwise velocity with temperature isoline at 1400 K (black line); right: mass fraction of hydrogen radical with stoichiometric isoline (red dotted line)

(section 2.1), the reaction zone is shifted from the lean (most-reactive) to the stoichiometric mixture fraction. This process correlates with the findings under simplified conditions for ignition in a straight turbulent jet. In section 5.3.3 the transition in the chemical reaction process from autoignition controlled reaction to flame propagation is analyzed in more detail. At $t = 0.06$ ms, the flame spreads along the stoichiometric line and forms a tube around the core of the fuel jet. At the bottom side of the fuel jet, the flame (indicated by the black isoline) is located in the region of lower velocity. Upstream of 20 mm, there are even regions with highly negative velocities (see also sections 5.2 and 6.1). When the local instantaneous streamwise velocity at the upstream flame front is very low or even negative, the flame spreads upstream into the recirculation region and can anchor there as stable steady flame.

6.2.4 Validation Metric

In the qualitative analysis, the spot-wise ignition and stabilization processes could be reproduced very well. The present section is focused on the quantitative evaluation of the modeling capabilities. As explained in section 6.2.1.2, the quantitative comparison must be based on the flame anchoring limits (figure 6.2.8). However, the flame stabilization process is an intermittent phenomenon. First, the autoignition location depends on the local hot gas temperature (section 6.2.3) and turbulence structure (cp. labscale JHC case in section 5.3). Only ignition kernels, which occur very far upstream ($x \leq 30$ mm) have the potential to stabilize in the recirculation region. Nevertheless, some of these upstream kernels (between 25 and 35 mm) do not lead to flame stabilization, when locally high streamwise velocities or unfavorable instantaneous mixture conditions are present (figure 6.2.7).
In a quantitative analysis of the flame anchoring limits it must be ensured that potential rare stabilization events are detected. In the experiment, long physical observation times ensure that sufficient statistical variations (esp. for temperature) are covered. However, in the numerical simulation, long physical computation times would be very cost-intensive. However, the statistical variation and therefore the numerical cost can be reduced significantly when constant crossflow temperatures are applied instead of the full temperature statistics.

Constant Inflow Temperature for Hot Crossflow The solutions in figure 6.2.12 were conducted with constant hot crossflow temperatures T_{cf}. Any temperature fluctuations are neglected. In contrast to the experimental observations and simulations with temperature fluctuation, where autoignition occurred in form of separated kernels, a steady lifted flame establishes in the numerical results with constant hot gas temperature. Even far downstream, steady lifted flames are visible at a constant distance from the jet orifice. This phenomenon also occurred in different autoignition experiments, such as in the jet-in-hot-coflow test case in section 5.3). In the study by Markides and Mastorakos [102, 101] this phenomenon is

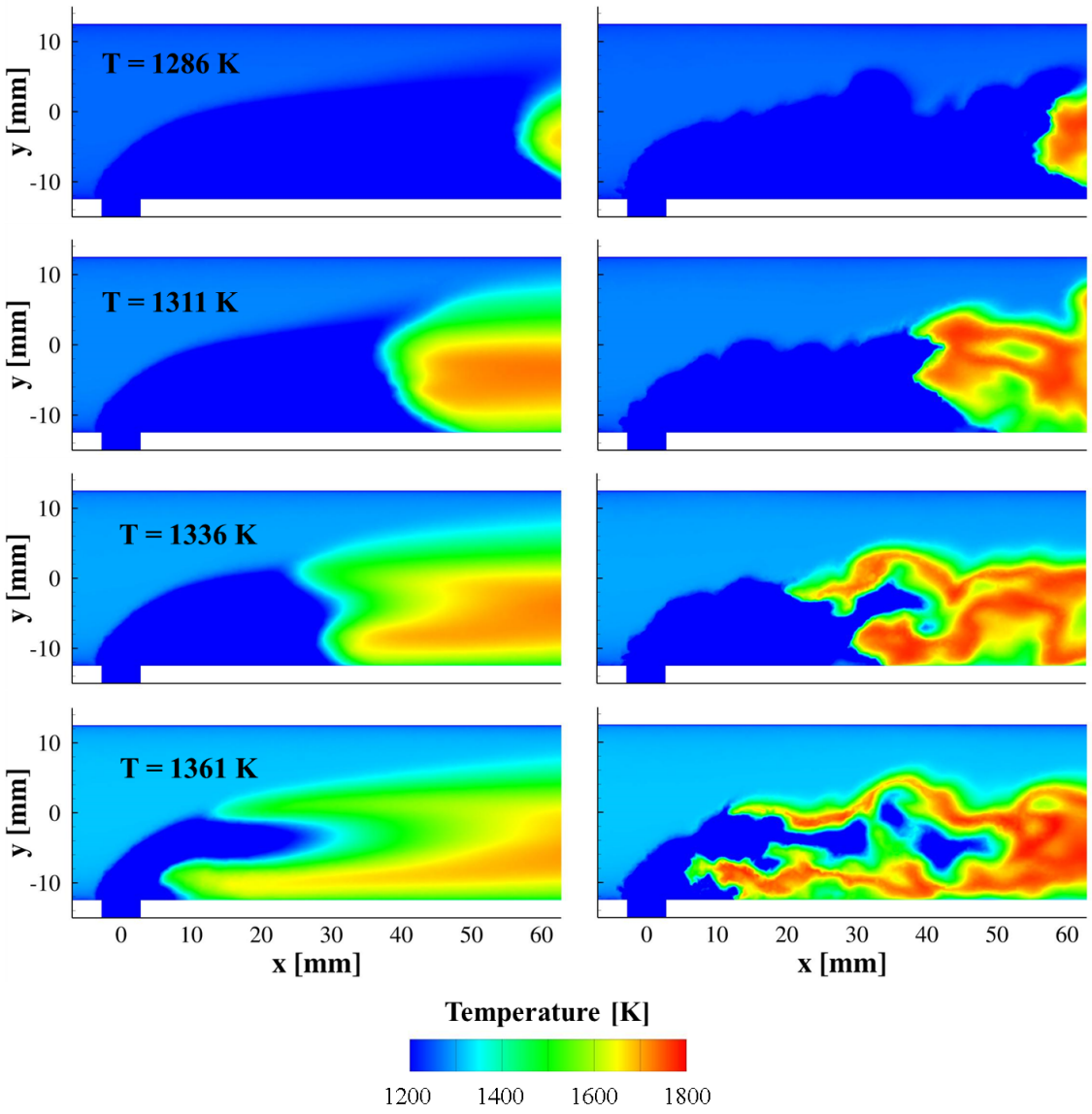

Figure 6.2.12: Lifted flame with constant temperature inflow with $X_{\mathrm{H2,fuel}} = 0.33$ (Coarse grid SAS)

called “lifted flame regime” (see also section 2.4).
The average ignition location (or lift-off height) depends significantly on the hot gas temperature (figure 6.2.12). A temperature increase of about 1 % results in an upstream shift of the averaged ignition front by about 8 mm (30 mm between $T = 1286\,\mathrm{K}$ and $T = 1336\,\mathrm{K}$). At the highest temperature $T_{\mathrm{cf}} = 1361\,\mathrm{K}$, the ignition front is located very far upstream in the low velocity region on the leeward side of the jet; similar to the stabilized flames in figures 6.2.6 and 6.2.10.

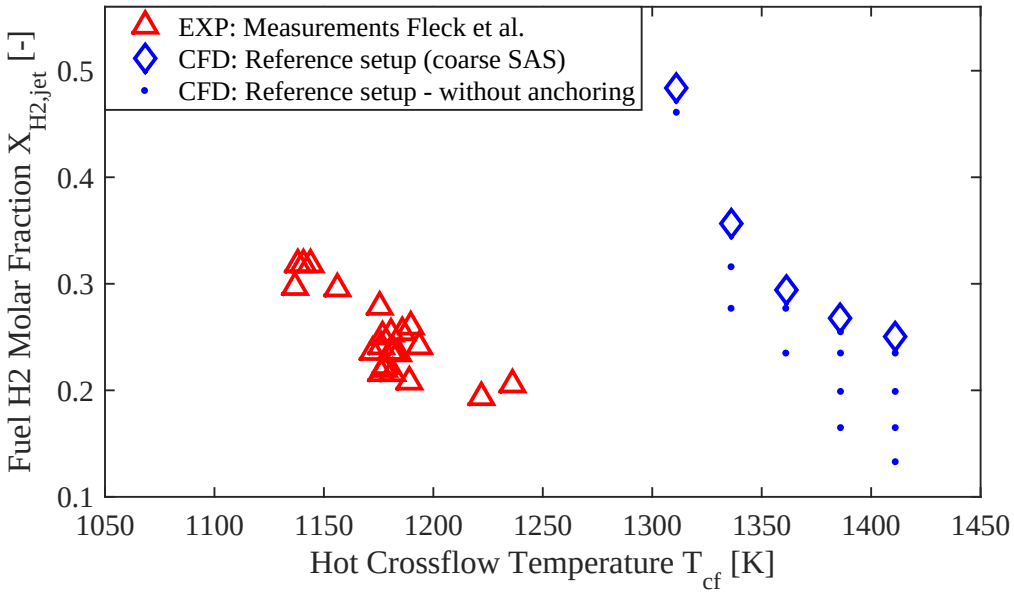

Figure 6.2.13: Deterministic validation metric for flame anchoring limits

Validation Metric The validation metric is presented in figure 6.2.13. The numerical approach for the identification of the flame anchoring limits is similar to the experimental procedure. The crossflow temperature is set to a specific value and the fuel hydrogen content is increased step-wise until the flame anchors in the low velocity region close to the jet orifice. The flame anchoring limits are assessed for 5 different hot gas temperatures ($T_{\mathrm{cf}} = 1311, 1336, 1361, 1386$ and $1411\,\mathrm{K}$).
An example for 1311 K is provided in figure 6.2.14. In contrast to figure 6.2.12 (constant fuel concentration, varying temperature), in figure 6.2.14 the fuel concentration is increased at constant temperature. The location of the ignition front is less sensitive on fuel concentration compared to the temperature. Up to a hydrogen concentration of ($X_{\mathrm{H2}} = 0.46$), an increase in fuel concentration of 1 % results in an upstream shift of the ignition front of only 0.5 mm (20 mm between $X_{\mathrm{H2}} = 0.33$ and $X_{\mathrm{H2}} = 0.46$). If the flame is close to the low velocity region, a small increase in hydrogen from $X_{\mathrm{H2}} = 0.46$ to 0.48 leads to a sudden jump and the flame

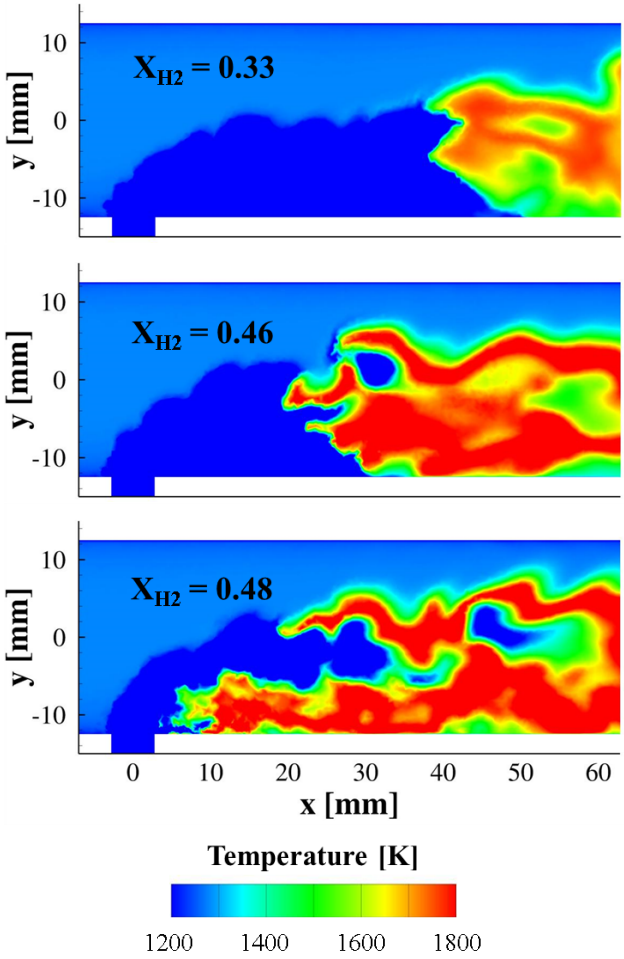

Figure 6.2.14: Lifted flame with constant temperature inflow at 1311 K (Coarse grid SAS)

front moves upstream by about 15 mm and anchors in the recirculation region very close to the jet orifice. This sudden significant increase is taken as indicator for flame anchoring for the construction of the validation metric in figure 6.2.13.

In figure 6.2.13 the blue dots indicate simulation runs with no flame anchoring (e.g. for 1311 K and $X_{H2} = 0.46$), while the diamonds indicate the critical hydrogen content at which flame anchoring occurs (1311 K and $X_{H2} = 0.48$). Although the qualitative characteristics of the ignition and flame anchoring mechanism can be reproduced satisfactorily by the simulation, there is a considerable quantitative discrepancy between experimental measurements and numerical results. A significant temperature increase of about 200 K is necessary to reproduce the flame anchoring at similar hydrogen concentrations. The uncertainty sources for this modeling deficiency are evaluated in the following paragraph.

6.2.5 Uncertainty Quantification

Due to the complexity of this test case, the source for the modeling uncertainty is not self-evident. Potential uncertainty sources can be related either to **"model input uncertainties"** [133], such as inaccurate definitions of boundary conditions and specific model parameters or to **"model form uncertainties"** [133], which occur due to inadequate or insufficient model simplifications. In addition, also **experimental uncertainties** in test conditions and **"system response quantities"** [133] must be taken into account (chapter 4).

To asses the impact of different uncertainty sources an uncertainty quantification is conducted. An exact analysis of uncertainties in the numerical prediction allows for a well-directed and efficient model optimization and an improvement of future experiments. At first, the most relevant uncertainty sources need to be identified. In a detailed sensitivity study for gas turbine conditions, Prause et al. [151] investigated a large range of potential uncertainty sources. These included model input parameters, such as variations in hot crossflow composition and temperature, inflow velocity profiles and wall heat transfer. Furthermore, model form uncertainties for the different submodels were analyzed, e.g. sensitivities to the application of different chemical kinetic models, specific diffusivities and grid resolution were assessed.

Finally, following major uncertainty sources were identified:

- Hot crossflow temperature (uncertainty in experimental measurements)
- Chemical reaction mechanisms (model input uncertainty (model parameters))
- Turbulence modeling (model form uncertainty)
- TCI modeling (model form uncertainty)

In the following sections, these uncertainty sources are analyzed in more detail.

6.2.5.1 Hot Crossflow Temperature Uncertainty

Experimental Uncertainty

During the test runs, the hot crossflow temperature was monitored by a shielded thermocouple probe, which has a temporal resolution of about 0.1 s. Since the residence time for mixing is just about 0.5 ms, temperature fluctuations can not be resolved. However, as shown in section 6.2.3 (Analysis of Transient Ignition Process), the autoignition process in the present

test case is very sensitive to moderate temperature variations. Therefore, additional laser-Raman measurements with high temporal resolution were conducted (section 6.2.1.1) and a standard deviation of $\sigma_T = 2.8\,\%$ has been assessed for the temperature fluctuations. Although it can not be fully determined, whether the standard deviation of $\sigma_T = 2.8\,\%$ is due to actual temperature fluctuations or is within experimental uncertainties, this value specifies the actual uncertainty range for the unresolved temperature fluctuations in either case.
Finally, it must be considered, that the flame anchoring events are initiated by the most upstream ignition kernels, which in turn occur only at exceptional high temperature peaks, so called "rare events" [35]. To quantify the impact of the temperature uncertainty on autoignition, the full range of possible temperature states (including high temperature peaks) must be considered. Since the temperature is normally distributed (figure 6.2.3), it can be assumed that 95 % of all temperature values lie within two standard deviations of the mean ($\pm\,2\,\sigma_T$). A limited range of 95 % is sufficient for this analysis, since the highest temperature peaks still need a sufficient spatial expansion to actually trigger an autoignition kernel.

$$\Delta T_{\mathrm{cf,unc}} \approx \pm\,(2\sigma_{T,\mathrm{Raman}} + 0.06)\,T_{\mathrm{probe}} \approx \pm 76\,\mathrm{K} \tag{6.2.4}$$

The resulting crossflow temperature uncertainty $\Delta T_{\mathrm{cf,unc}} \approx \pm\ 76\,\mathrm{K}$ is composed of the estimated temperature range and the measurement uncertainty of the thermocouple probe of $\pm\,6\,\%$ (section 6.2.1.1).

Impact of Temperature Uncertainty on the Accuracy of the Simulation

The quantitative impact of the uncertainties on the validation metric is visualized in figure 6.2.15. The temperature uncertainty of $\pm\,76\,\mathrm{K}$ (equation 6.2.4) is indicated by errorbars for selected experimental ignition limits. An exponential curve of the form $A \cdot \exp(\lambda/T)$ is fitted to the experimental results. The resulting curve (bold red line) is defined by $A = 0.000348$ and $\lambda = 7728.62\,\mathrm{K}$. The experimental limits ($X_{\mathrm{H2,jet}}$) are scattered up to $\pm\,14\,\%$ around the mean. The gray area in figure 6.2.15 comprises the total uncertainty range for the experimental results, including hot gas temperature fluctuations ($\pm\,76\,\mathrm{K}$) and variations in ignition limits ($\pm\,14\,\%$).
In chapter 5.1.1 the influence of temperature variations on ignition delay time has been investigated previously by detailed shock tube experiments at relevant operating conditions (similar compositions, high pressures and relevant temperatures). It was shown that there is a strong non-linear dependency and exceptional high sensitivity of autoignition time on temperature (figure 5.1.3). Applying equation 5.1.1 it can be assumed that a temperature increase of $+\,76\,\mathrm{K}$ leads to a shortening of the ignition delay time by a factor of 7, which is almost one order of magnitude. Due to this high sensitivity of ignition delay time on

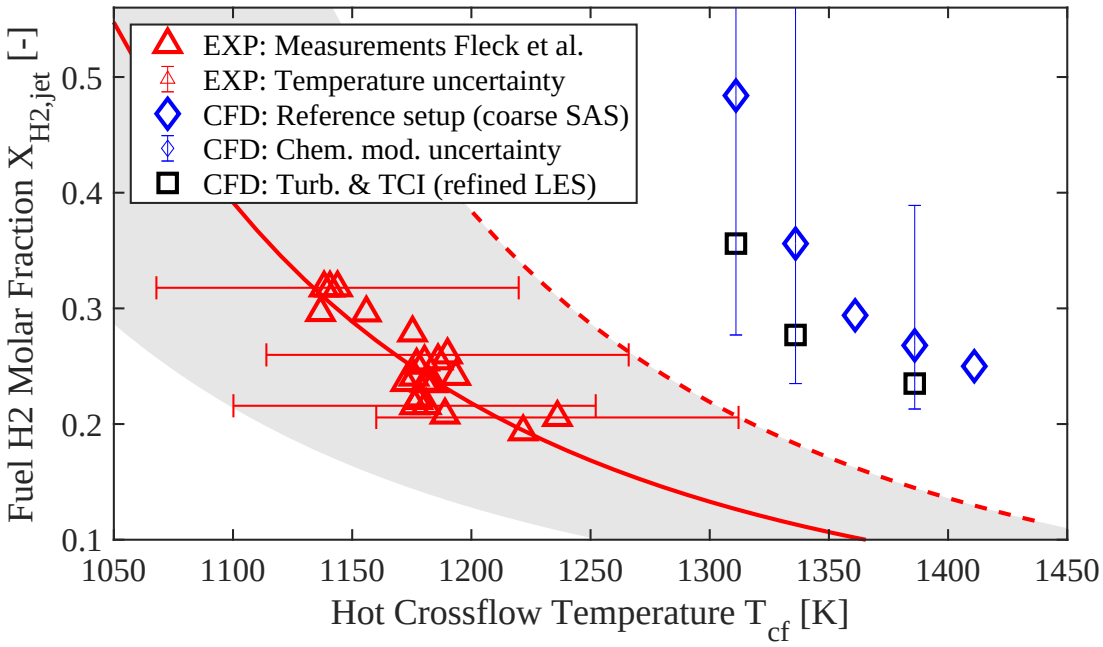

Figure 6.2.15: Non-deterministic validation metric for flame anchoring limits with uncertainty ranges for hot crossflow temperature (experimental) and modeling uncertainties for chemistry, turbulence and TCI; red bold line: temperature mean; red dashed line: temperature maximum

temperature variations, it must be assumed that ignition always occurs at the highest temperature peaks. In experimentally determined ignition limits due not depend on the mean temperature, but are rather function of the highest instantaneous temperature peaks. In figure 6.2.15 the potential ignition limit at probably highest (local and instantaneous) temperatures is visualized by the red dashed line.

As described previously in chapter 6.2.2, the temperature variation statistics of the hot gas cannot be resolved in time and space in the simulation due to excessive computing costs. For the numerical results in figure 6.2.15 (blue and black symbols), only constant gas temperatures are applied at the hot exhaust gas inflow boundary. To allow for comparability with the experimental results, the numerical results should be compared with the red dashed line, which indicated the experimental ignition limited at the estimated local and instantaneous temperature maximum.

Considering the uncertainties of hot gas temperature fluctuations in the experiment, the deviation between numerical and experimental results is significantly reduced. However, there is still a considerable difference between simulation and experiment. This suggests that additional uncertainty sources need to be considered.

6.2.5.2 Chemistry Modeling Uncertainty

The general accuracy of the chemical reaction mechanism under relevant engine operating conditions has been investigated in section 5.1 (Autoignition in a Homogeneous System). It was found that the ignition reaction path lies between two competing ignition pathways: for high temperatures, ignition proceeds mainly through the fast build-up of H-radicals; whereas at lower temperatures, ignition through H-atom build-up is inhibited and a second path through the slow build-up of HO_2 and H_2O_2 leads to ignition. Under the present test conditions, the crossover temperature lies at $T_{co} = 1270\,K$ (figure 5.1.3). Furthermore, the Ó Conaire mechanism [135] was validated on the basis of an appropriate shock tube experiment. It was found that around the crossover, the ignition calculations deviate by a factor of 3 from experimental ignition measurements.

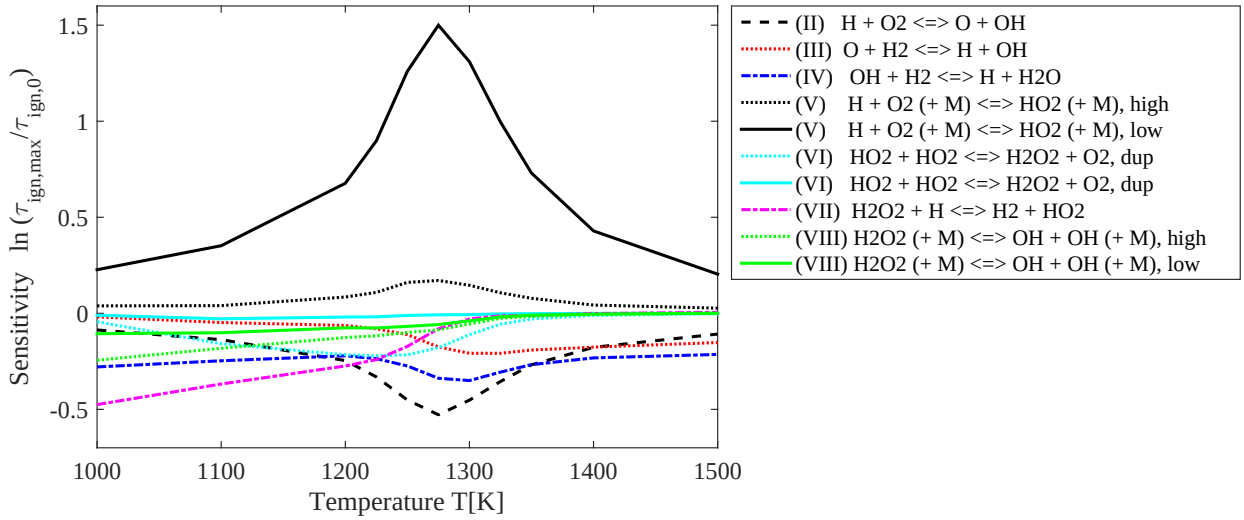

Figure 6.2.16: Sensitivities of the Ó Conaire mechanism [135] with respect to the ignition delay time

With relation to the present jet-in-hot-crossflow test case, the objective is to assess the impact of kinetic model uncertainty on the prediction of the flame anchoring limits. In the present simulation, the detailed chemical reaction mechanism by Ó Conaire [135] is applied. It can be assumed that the deficiency in the kinetic model is related to uncertainties in the model parameters (Arrhenius equation 2.1.7). An established approach to quantify the impact of parametric uncertainties is the propagation of the uncertainties through the model. Sophisticated approaches for the propagation of kinetic parametric uncertainties were published recently by Najm et al. [126] and Le Maître et al. [100].
In the present work, due to the complexity of the system, only the impact of the most critical

parameter is analyzed. The most sensitive reaction is identified by the linear transformation tool "linTM" [119, 118], which was developed by Torsten Methling [117]. The pre-exponential constant A is varied separetely for each reaction in the range of their respective uncertainties [14] under gas turbine operating conditions ($p = 15\,\text{bar}$ and $X_{\text{H2,local}} = 0.02$). The resulting variation in ignition delay time is presented in figure 6.2.16 for the most sensitive reactions. It is found, that the most relevant reaction is reaction V. The sensitivity of the ignition delay time τ_{ign} is especially high at the crossover temperature $T_{\text{co}} = 1270\,\text{K}$ between the two competing ignition pathways. For these conditions the maximum ignition delay time has an uncertainty $\tau_{\text{ign,max}} = 4.5 \cdot \tau_{\text{ign,0}}$ (equation 6.2.5). This is in the range of the uncertainties, which were found for the shock tube experiment in section 5.1.

$$\frac{\tau_{\text{ign,max}}}{\tau_{\text{ign,0}}} = e^{1.5} = 4.5 \tag{6.2.5}$$

$$\frac{A_{\text{V,max}}}{A_{\text{V,0}}} = 10^{0.2} = 1.58 \tag{6.2.6}$$

The parametric uncertainty of the pre-exponential constant A of reaction V is taken from Baulch et al. [14] (eq. 6.2.6). The respective minimum and maximum values ($A_{\text{V,0}} \,/\, 1.58$ and $A_{\text{V,0}} \cdot 1.58$) are propagated through the full CFD simulation for three crossflow temperatures ($T_{\text{cf}} = 1311, 1336$ and $1386\,\text{K}$). The resulting impact of this parameter uncertainty on the flame anchoring limits is visualized in figure 6.2.15. The critical fuel concentrations are affected significantly by this parameter variation. The flame anchoring limits vary up to a factor of 2. However, these error bars only provide a rough estimate, since only one parameter has been varied independently, although the kinetic parameters of the various reactions are closely coupled. Unfortunately, due to its complexity, a comprehensive analysis for all parameters and their dependencies is beyond the scope of this work.

6.2.5.3 Turbulence Modeling Uncertainty

The SAS and LES turbulence models are both scale-resolving approaches. Large turbulent scales are directly resolved and modeling is only applied to the small sub-grid scales. Therefore, the impact of these turbulence models can be investigated by a grid refinement study. On refined grids, smaller turbulent scales are directly resolved and the impact of the turbulence model is reduced. In the previous paragraphs the comprehensive parameter variations were all conducted with the "Coarse Grid" setup (table 6.2) with a grid resolution of $\Delta x = 0.8\,\text{mm}$. These results are now compared with LES simulations on a refined grid ($\Delta x = 0.1\,\text{mm}$). Additional flame anchoring limits are assessed with the high-resolved, but costly setup for three temperatures. The respective results are indicated as black squares in

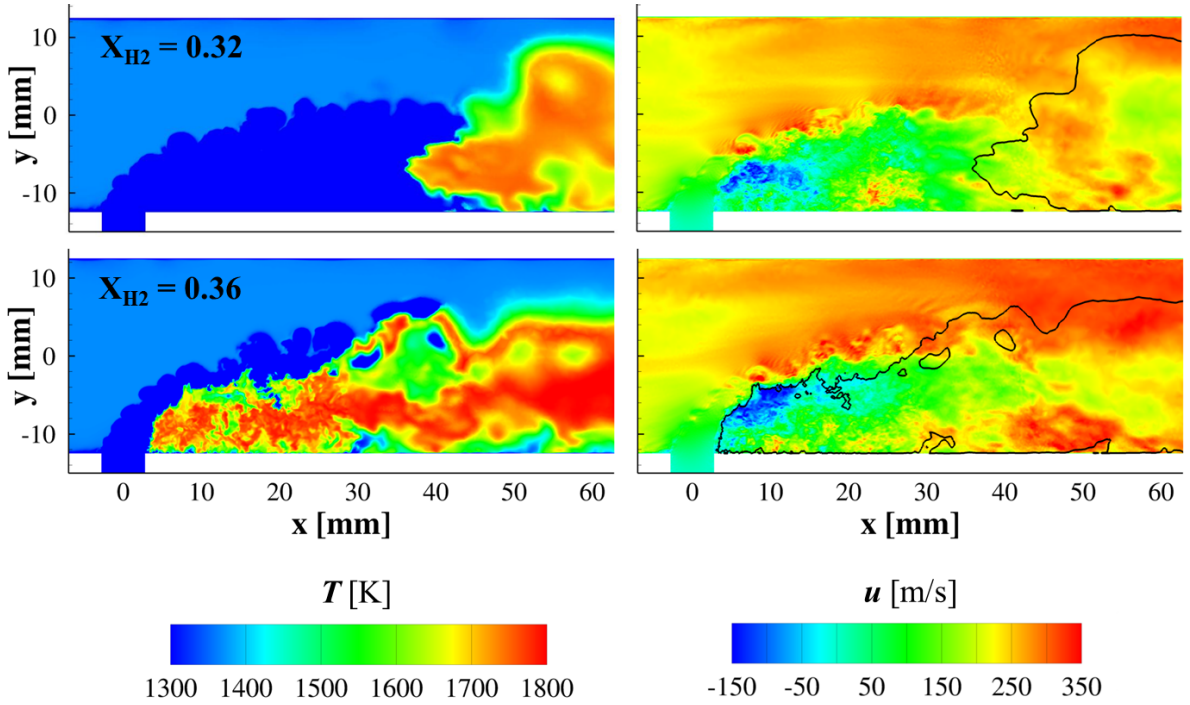

Figure 6.2.17: Lifted flame with constant temperature inflow at 1311 K (Fine grid LES); instantaneous snapshots for two fuel concentrations $X_{H2} = 0.32$ (top) and $X_{H2} = 0.36$ (bottom); left: instantaneous distributions for temperature; right: streamwise velocity with temperature isoline at 1400 K (black line)

figure 6.2.15 anchoring limits are reduced significantly and the numerical results are closer to the experimental values. To analyze the sources for this improvement, snapshots of temperature distributions for a hot gas temperature of 1311 K are presented in figure 6.2.17 and can be compared with the results on the coarse grid in figure 6.2.14. At low hydrogen molar fraction $X_{H2} = 0.32$, the location of the lifted ignition front at $x \approx 35$ mm is very similar for both setups on the coarse and the fine grid. However, on the fine grid, the upstream flame propagation and flame anchoring in the recirculation zone occurs at much lower hydrogen concentrations ($X_{H2} = 0.36$) compared to the coarse grid computations ($X_{H2} = 0.48$). For conditions just prior to flame anchoring on the coarse grid ($X_{H2} = 0.46$ in figure 6.2.14), the average ignition locations are upstream of 30 mm, but in contrast to the experiment (figure 6.2.7), the flame does not propagate upstream.

The delayed upstream flame propagation in the coarse grid simulation is related to two different modeling deficiencies: The modeling of the turbulent stresses (turbulence modeling) and insufficient resolution of turbulent structures. The second cause, which is related to TCI modeling is described in the next section (section 6.2.5.4). In the present section, the uncertainties due to turbulence modeling are explained in more detail.

The comparison of the velocity results for the non-reacting flow in section 6.1 provides a good insight into the turbulence modeling capabilities for the present test case. Of special interest is the low velocity region at x between 25 and 35 mm and y between -5 and -10 mm (figure 6.1.7) where upstream flame propagation initiates the flame anchoring process (figures 6.2.7, 6.2.9 and 6.2.10). In this region, the average streamwise velocities are smaller in the fine grid computation (LES setup) compared to the coarse grid (SAS setup). Due to smaller streamwise velocities, the upstream flame propagation can proceed at lower fuel concentrations in the LES. A significant part of the discrepancies in flame anchoring limits can therefore be related to deficiencies in turbulence modeling in the region around $x = 30$ mm. As described in section 3.2.2.1, the modeling of the turbulent stress tensor by the eddy viscosity approach is based on the assumption that the turbulence viscosity is isotropic. But for anisotropic structures, as they are present in the recirculation region of jets-in-crossflow, large uncertainties must be accepted with this approach [23, 75, 97].

Although, the impact of turbulence modeling has been reduced in the higher-resolved LES, the model impact is still significant (table 6.2: $(\nu_t/\nu)_{\mathrm{LES,max}} \approx 50$). Due to the high Reynolds number, a large range of turbulent scales is still not resolved and the comparison of the two setups can only give an indication of the model accuracy. Since higher resolutions are too costly for the application under gas turbine operating conditions, additional information about the actual model accuracy for comparable coarse LES has been gained in the study of the generic jet-in-crossflow at reduced Reynolds numbers in section 5.2. There, much higher turbulence resolution could be achieved and was compared with coarser grid setups (figure 5.2.6). In the critical region between 4 and 6 diameters downstream of the jet injection (equivalent to a location between 22 and 33 mm in the present test case), the streamwise velocity is further reduced with finer resolution. It can be assumed, that also in the present test case under gas turbine conditions, a higher grid resolution would reduce the flame anchoring limits even further.

6.2.5.4 TCI Modeling Uncertainty

As described in chapter 3 (Numerical Methods), the TCI model takes account for the influence of unresolved fluctuations of temperature and composition on the cell-averaged chemical source term. In the present work, the APDF approach has been applied. The temperature distribution is approximated with a uni-modal Gaussian shape and the species are represented by a multi-variate β-PDF.

Grid Resolution Since the TCI model is applied to the unresolved subgrid scales only, the impact of the model is also directly related to the grid resolution. Therefore, the uncertainty range, which was determined by the grid refinement in the previous section (section 6.2.5.3),

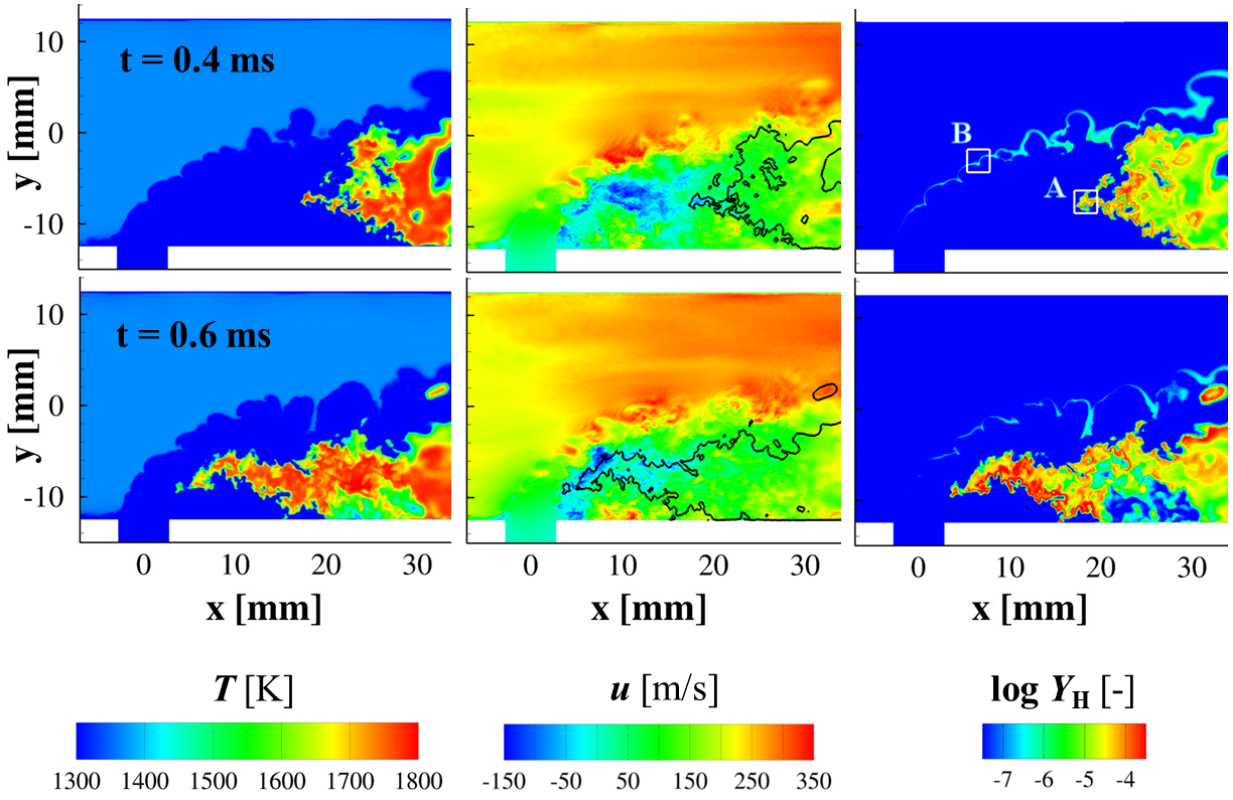

Figure 6.2.18: Transient flame anchoring process during the increase of the hydrogen fuel content from $X_{H2} = 0.32$ to $X_{H2} = 0.36$; snapshots at $t = 0.4$ ms (top) and $t = 0.6$ ms (bottom)

also covers the impact of subgrid TCI modeling. Due to the close interference between turbulence and TCI modeling, it is not possible to quantify their individual impact separately. Nevertheless, the grid refinement study provides additional information about the turbulence-chemistry interaction.

Flame Anchoring In figure 6.2.18, the transient process of the upstream flame propagation and the subsequent flame anchoring is presented for the fine grid LES computation. The hydrogen concentration was increased transiently at the pipe inflow from $X_{H2} = 0.32$ to $X_{H2} = 0.36$. The time $t = 0$ is set to the moment, when the higher fuel concentration reaches the jet inlet. Instantaneous distributions for temperature, streamwise velocity and hydrogen radical concentration are presented for two snapshots at $t = 0.4$ ms and $t = 0.6$ ms.
The transient flame anchoring process has already been described in section 6.2.3 for the SAS results. Similar characteristics are revealed by the LES results, but these are even more distinct. The propagating flame front at $t = 0.4$ ms is highlighted in figure 6.2.18 by the white frame A. It is presented in figure 6.2.19 in a magnified view. The local distributions of velocity and mixture fraction reveal, that the thin flame front spreads upstream at this spe-

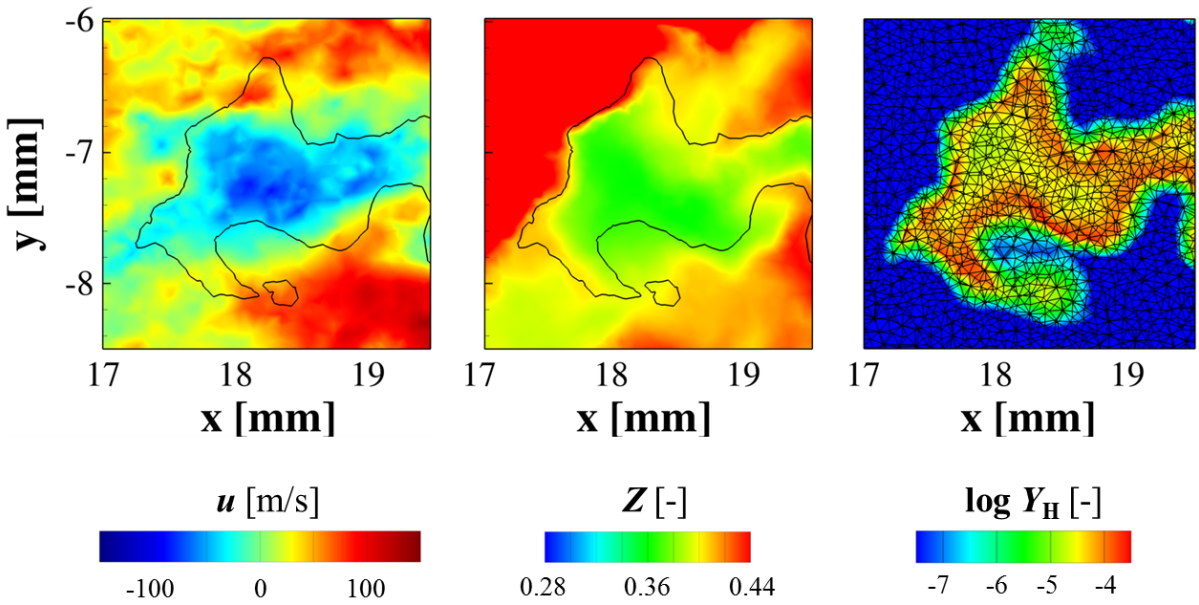

Figure 6.2.19: Enlarged view of frame A from figure 6.2.18: Streamwise velocity, mixture fraction ($Z_{st} = 0.36$) and mass fraction of hydrogen radical for the propagating flame front at textitt = 0.4 ms

cific location, only because negative velocity (dark-blue) and stoichiometric mixture (green: $Z_{st} = 0.36$) are present simultaneously in this region. Similar properties can be found for the flame at $t = 0.6$ ms, where the flame is distributed over the entire range of negative velocity up to the jet inlet.

This example shows again, that the subsequent flame anchoring is an intermittent process, which depends significantly on local turbulent structures. An ignition kernel, which evolves between 25 and 35 mm might or might not lead to flame anchoring. The upstream flame propagation process can only proceed if locally suitable conditions for velocity, mixture and chemical state are present simultaneously.

Furthermore, it is obvious, that much finer flame structures are resolved with the finer LES compared to the coarser SAS setup (figure 6.2.11). The reaction zone of the pre-ignition radical build-up is visualized by the instantaneous hydrogen radical concentration (third column in figure 6.2.19). A magnified view of the pre-ignition zone (frame B) is presented in figure 6.2.20. It reveals, that even in the refined LES (with 17 million grid points), the reaction zone is actually captured by only 1 - 2 grid cells. Thus, it can be assumed that the actual flame structures are even finer. Potentially, with a higher resolution of the turbulent scales the local patches of negative velocity would reach further downstream, extending the critical distance of stabilizing ignition kernels.

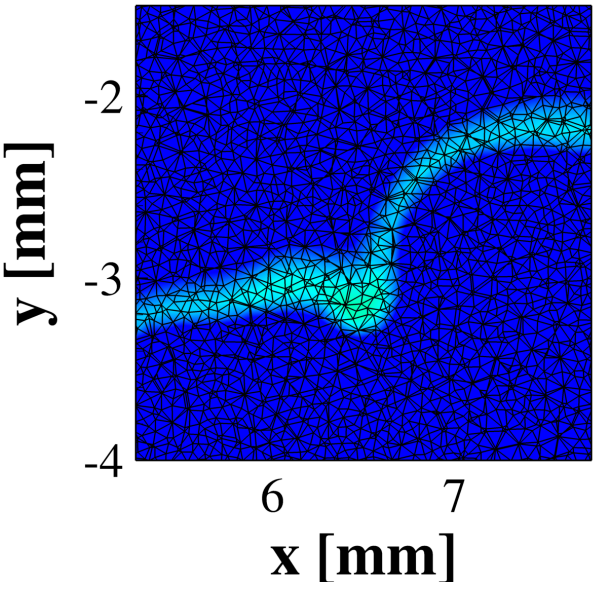

Figure 6.2.20: Enlarged view of frame B from figure 6.2.18: Pre-ignition radical build-up at $t = 0.4\,\mathrm{ms}$ visualized by the hydrogen radical mass fraction Y_{H} with computational mesh

Autoignition Finally, in addition to the random character of the flame anchoring process, the initial autoignition and kernel evolution process also depends significantly on local turbulent structures. In section 5.3 (Turbulent Autoignition in a Jet-in-Hot-Coflow), the capability of the APDF-TCI model was analyzed for transient autoignition events at reduced Reynolds number. In the respective study, the high-resolved LES computation revealed, that the spatial variation of the ignition location (especially the most-upstream kernels) can only be reproduced, when the large turbulent shear layer vortices are resolved. However, in the present jet-in-crossflow configuration, the characteristics of the large-scale shear layer vortices are probably dominated by periodic instabilities of the hovering vortex [84] at the jet inlet (section 5.2). However, these periodic vortex instabilities are produced in the vicinity of the pipe wall and can not be resolved in the present study under gas turbine operating conditions. Thus, the total range of potential ignition locations in the shear layer vortices can not be fully captured.

Furthermore, it was shown in section 5.3, that the assumption of a uni-modal temperature distribution is only valid, if the reaction zone is sufficiently resolved by the numerical grid. For coarse spatial resolutions, the temperature distribution within the cell actually exhibits a bi-modal shape (figure 5.3.10 to figure 5.3.12). The relation between the two peaks provides an ignition probability. In figure 6.2.20 the pre-ignition radical pool is presented in higher detail. It is obvious that the pre-ignition radical build-up is resolved by 1 - 2 grid cells only.

Thus, despite the higher grid resolution in the LES, a high impact of TCI modeling must still be accepted due to the high Reynolds number. A convenient alternative for the uni-modal APDF-TCI approach, might be TCI models which consider higher moments, such as T-PDF [41] or DQMoM methods [40].

Conclusions

The experimentally observed spot-wise ignition and stabilization processes are well reproduced by the numerical simulation. It was demonstrated, that temperature fluctuations in the hot crossflow have a significant influence on the variation of the ignition location. However, quantitatively, considerable deviations are present between experiments and numerical simulation. To identify and evaluate the sources of the modeling uncertainty, a detailed uncertainty quantification has been conducted.

7 Conclusions

The design process of novel combustion systems increasingly relies on numerical simulations. A good knowledge of the capabilities and accuracy of the computational models is required to evaluate numerical predictions and to deduce reliable decisions for the further development process. With respect to turbulent autoignition modeling, numerous validation studies have been published recently for generic straight lifted jet flames at atmospheric pressure. However, it is questionable to what extent the findings obtained under simplified laboratory conditions (simple flow geometry, atmospheric pressure and low turbulence) can be applied to real gas turbine conditions (complex flow geometry, increased pressure and high turbulence). Until now, however, no detailed validation studies have been conducted for autoignition simulations under real gas turbine operating conditions.

The present thesis closes this research gap. The predictive capability of prevailing computational models has been assessed for autoignition and subsequent flame stabilization under gas turbine conditions. The validation study focuses on the fuel premix section of a staged gas turbine at a pressure of 15 bar. Hydrogen-rich fuel is injected transversely to the hot oxidizer at temperatures above 1000 K and Reynolds numbers up to 10^6. The validation study reveals that qualitative trends and general combustion phenomena, such as ignition and flame stabilization can be reliably reproduced. In the quantitative comparison, however, there are significant differences between experimental and numerical results, which can be attributed mainly to the high pressure and complex flow geometry. This shows that the transference of validation results from atmospheric lab-scale test cases to numerical predictions under high-pressure engine conditions must be handled very carefully. High pressure conditions place higher demands on measurement and simulation technology.

Higher measurement uncertainties must be accepted. With respect to simulations at high turbulent Reynolds numbers, lower turbulence resolution can be achieved by scale-resolving turbulence models and several closely coupled submodels are required to model various physio-chemical processes such as turbulence, chemical reaction and turbulence-chemistry interaction (TCI). Due to the high number of interrelated uncertainty sources, rating the importance of specific uncertainty sources and identifying the relevant modeling optimization potential under realistic gas turbine conditions is difficult.

In the present work, the validation hierarchy approach proposed by Oberkampf is applied to identify the most relevant uncertainty sources and modeling optimization potential. In addition to the application-oriented high-pressure experiment, selected subsystems with reduced complexity were defined and investigated. By combining the advantages of complete system experiments under engine-relevant conditions and specifically selected lab-scale experiments, more detailed insight into the modeling capabilities has been gained. It was found that the quantitative difference between experimental and numerical results cannot be explained by one single parameter alone, but is related to a combination of three major sources.

1. **Inflow boundary conditions for hot gas temperature**
   The ignition delay time is extremely sensitive to temperature. Under the operating conditions examined in this thesis, small temperature fluctuations with a standard deviation of 2.8 % lead to a variance of 130 % in ignition delay times. Thus, small uncertainties in the boundary definition of the hot gas inflow temperature have a large effect on the accuracy of the simulation results.

2. **Chemical reaction mechanisms**
   The chemical reaction mechanism for hydrogen combustion is well understood under low pressure and high temperature conditions. However, under gas turbine relevant conditions (high pressure, intermediate temperature) the ignition process proceeds along a different reaction pathway. Under these conditions, only few research studies exist and many questions remain to be solved, resulting also in a much higher modeling uncertainty. In the pressure and temperature range examined for this work, the modeling uncertainty for the ignition delay time is more than 100 %.

3. **Turbulence-chemistry interaction modeling**
   In turbulent flows, ignition kernels are often distributed over a large spatial and temporal range. In the validation studies for straight lifted jet flames, this variation of ignition location had been of minor importance. In straight flows, the averaged flame stabilization heights are similar to the averaged ignition heights. In many gas turbine combustion systems, however, the fuel is injected transversely, in a jet-in-crossflow configuration. In this configuration very early ignition events, which occur far upstream in the vicinity of the jet recirculation zone, can initiate flame anchoring in the reverse flow region. Therefore, the modeling of the entire spectrum of potential ignition locations is crucial to correctly reproduce the flame stabilization. Thus, this range can only be reproduced if large-scale turbulent structures are resolved.

In design processes of novel combustion concepts, usually no experimental reference data exists with which the simulations can be compared. For these numerical predictions, a

reliable knowledge of the quantitative modeling accuracy is of great importance. Based on the findings of this thesis, it is possible to provide best-practice guidelines for the industrial and scientific application of autoignition simulation under relevant gas turbine conditions:

1. Since small temperature variations can have a significant impact on the ignition delay time, it is of high importance to define the inflow temperature of the hot gas as accurately as possible. If the inlet temperatures cannot be assessed with sufficient accuracy, quantifying the measurement uncertainty of the temperature is recommended. Thus, the resulting modeling accuracy can be estimated quantitatively.

2. The accuracy of the chemical reaction mechanism can be determined by comparing homogeneous reactor simulations (0D) with appropriate shock tube experiments under engine relevant conditions. A detailed assessment of the quantitative uncertainty ranges is of special relevance if no experimental reference data can be provided for the relevant combustion system.

3. To reproduce the full range of potential ignition locations, the use of scale-resolving turbulence models is recommended. Nevertheless, gas turbine operating conditions are characterized by high Reynolds numbers. Therefore, a high impact of TCI subgrid modeling must be accepted. Often, mono-modal Gaussian temperature distributions are assumed for TCI modeling. The present work, however, showed that turbulent autoignition processes exhibit bi-modal temperature distributions in the ignition region. Therefore, the consideration of higher moments of temperature in TCI modeling is recommended.

In order to improve the credibility of the numerical prediction of autoignition, further research is needed in experimental as well as numerical research fields. To increase the accuracy of the inflow boundary definition of the hot gas inflow temperature, new experimental methods for high-speed temperature measurements would be of a high advantage. With respect to numerical modeling, the most promising optimization potential lies in chemical reaction modeling under relevant gas turbine conditions and the development of efficient TCI models that take higher moments of temperature into account.

Bibliography

[1] A. Abdilghanie, C. E. Frouzakis, and P. Fischer. Direct numerical simulation of autoiginition of a hydrogen jet in a preheated cross flow. *8th US Combustion Meeting*, 2013.

[2] AIAA. *Guide for Verification and Validation of Computational Fluid Dynamics Simulations*, 1998.

[3] The American Society of Mechanical Engineers (ASME), Three Park Avenue, New York, NY 10016-5990. *Standard for Verification and Validation of Computational Fluid Dynamics and Heat Transfer*, 2009.

[4] J. Andreopoulos. Heat transfer measurements in a heated jet-pipe flow issuing into a cold cross stream. *Phys. Fluids*, 26(11):3201–3210, 1983.

[5] J. Andreopoulos and W. Rodi. Experimental investigation of jets in a crossflow. *J. Fluid Mech.*, 138:93–127, 1984.

[6] C. M. Arndt. *Entwicklung und Anwendung von Hochgeschwindigkeits-Lasermesstechnik für die Untersuchung von Selbstzündung*. PhD thesis, Universität Stuttgart, 2017.

[7] C. M. Arndt, J. D. Gounder, W. Meier, and M. Aigner. Auto-ignition and flame stabilzation of pulsed methane jets in a hot vitiated coflow studied with high-speed laser and imaging techniques. *Appl. Phys. B*, 108:407–417, 2012.

[8] C. M. Arndt, M. J. Papageorge, F. Fuest, J. A. Sutton, W. Meier, and M. Aigner. The role of temperature, mixture fraction, and scalar dissipation rate on transient methane injection and auto-ignition in a jet in hot coflow burner. *Combust. Flame*, 167:60–71, 2016.

[9] C. M. Arndt, R. Schiessl, J. D. Gounder, W. Meier, and M. Aigner. Flame stabilization and auto-ignition of pulsed methane jets in hot coflow: Influence of temperature. *Proc. Combust. Inst.*, 34:1483–1490, 2013.

[10] C. M. Arndt, A. M. Steinberg, I. G. Boxx, W. Meier, and M. Aigner. Influence of heat release on swirl flow dynamics from high speed laser measurements in a gas turbine model combustor. *23rd ICDERS, July 24-29, 2011, Irvine*, 2011.

[11] H. Ax. Reheat Raman Messungen Schlussbericht. Technical report, Deutsches Zentrum für Luft- und Raumfahrt, Institut für Verbrennumgstechnik, 2017.

[12] S. Bagheri, P. Schlatter, P. J. Schmid, and D. S. Henningson. Global stability of a jet in crossflow. *J. Fluid Mech.*, 624:33–44, 2009.

[13] H.-J. Bauer. New low emission strategies and combustor designs for civil aeroengine applications. *Prog. Comput. Fluid Dyn.*, 4:130–142, 2004.

[14] D. L. Baulch, C. T. Bowman, C. J. Cobos, R. A. Cox, T. Just, J. A. Kerr, M. J. Pilling, D. Stocker, J. Troe, W. Tsang, R. W. Walker, and J. Warnatz. Evaluated kinetic data for combustion modeling: Supplement ii. *J. Phys. Chem. Ref. Data*, 34(3):757–1397, 2005.

[15] H. A. Becker and T. A. Massaro. Vortex evolution in a round jet. *J. Fluid Mech.*, 31:435–448, 1968.

[16] N. Branley and W. P. Jones. Large eddy simulation of a turbulent non-premixed flame. *Combust. Flame*, 127(1-2):1914–1934, 2001.

[17] M. P. Burke, M. Chaos, Y. Ju, F. L. Dryer, and S. J. Klippenstein. Comprehensive H2/O2 kinetic model for high-pressure combustion. *Int. J. Chem. Kinet.*, 44:444–474, 2012.

[18] R. Cabra, J. Y. Chen, R. W. Dibble, N. Karpetis, and R. S. Barlow. Lifted methane-air jet flames in a vitiated coflow. *Combust. Flame*, 143:491–506, 2005.

[19] R. Cabra, T. Myhrvold, J. Y. Chen, R. W. Dibble, N. Karpetis, and R. S. Barlow. Simultaneous laser raman-rayleigh-lif measurements and numerical modeling results of a lifted turbulent H2/N2 jet flame in a vitiated coflow. *Proc. Combust. Inst.*, 29:1881–1888, 2002.

[20] M. Cano Wolff. *Selbstzündung von brennstoffarmen Zweiphasenströmungen in Gasturbinen-Brennkammern.* PhD thesis, Karlsruher Institut für Technologie, 2007.

[21] M. Cano Wolff, J. Meisl, R. Koch, and S. Wittig. The influence of evaporation on the autoignition-delay of n-heptane air mixtures under gas turbine conditions. 27:2025–2031, 1998.

[22] R. R. Cao, S. B. Pope, and A. R. Masri. Turbulent lifted flames in a vitiated coflow investigated using joint PDF calculations. *Combust. Flame*, 142(4):438–453, 2005.

[23] M. Casey and T. Wintergerste. In *ERCOFTAC Special Interest Group on Quality and Trust in Industrial CFD*. 2000.

[24] A. Cavaliere and M. de Joannon. MILD combustion. *Prog. Energ. Combust.*, 30(4):329–366, 2004.

[25] D. R. Chapman. Computational aerodynamics development and outlook. *AIAA Journal*, 17(12):1293–313, 1979.

[26] P. Chassaing, R. A. Antonia, F. Anselmet, L. Joly, and S. Sarkar. *Variable Density Fluid Turbulence*. Springer Netherlands, 2002.

[27] H. Choi and P. Moin. Grid-point requirements for large eddy simulation: Chapman's estimates revisited. *Phys. Fluids*, 24(1):011702, 2012.

[28] B. B. Dally, A. N. Karpetis, and R. S. Barlow. Structure of turbulent non-premixed jet flames in a diluted hot coflow. *Proc. Combust. Inst.*, 29:1147–1154, 2002.

[29] L. Davidson. Lage eddy simulation: how to evaluate resolution. *Int. J. of Heat and Fluid Flow*, 30:1016–1025, 2009.

[30] M. Di Domenico. *Numerical Simulations of Soot Formation in Turbulent Flows*. PhD thesis, Universität Stuttgart, 2007.

[31] P. Domingo, L. Vervisch, and D. Veynante. Large-eddy simulation of a lifted methane jet flame in a vitiated coflow. *Combust. Flame*, 152:415–432, 2008.

[32] F. Ducros, F. Nicoud, and T. Poinsot. Wall-adapting local eddy-viscosity models for simulations in complex geometries. In *In 6th ICFD Conference on numerical methods for fluid dynamics*, pages 293–299, 1998.

[33] B. M. Duda, F. R. Menter, S. Deck, H. Bézard, T. Hansen, and M.-J. Estève. Application of the scale-adaptive simulation to a hot jet in cross flow. *AIAA Journal*, 51(3):674–685, 2013.

[34] B. M. Duda, F. R. Menter, T. Hansen, and M.-J. Esteve. Scale-adaptive simulation of a hot jet in cross flow. *J. Phys.: Conf. Ser.*, 318(4):042050, 2011.

[35] R. B. Duffey. Predicting rare events: Risk exposure, uncertainty and unknown unknowns. In *AR2TS 19th Symposium, Stratford, England*, 2010.

[36] K. M. Düsing, A. Ciani, and A. Eroglu. Effect of mixing quality on NOx emissions in reheat combustion of GT24 & GT26 engines. In *ASME Turbo Expo 2011*, number GT2011-45676, 2011.

[37] C. Duwig and L. Fuchs. Large eddy simulation of a H2/N2 lifted flame in a vitiated co-flow. *Combust. Sci. Technol.*, 180:453–480, 2008.

[38] T. Echekki and J. H. Chen. Direct numerical simulation of autoignition in nonhomogeneous hydrogen-air mixtures. *Combust. Flame*, 134:169–191, 2003.

[39] Y. Egorov, F. R. Menter, R. Lechner, and D. Cokljat. The scale-adaptive simulation method for unsteady turbulent flow predictions. part 2: Application to complex flows. *Flow Turbul. Combust.*, 85(1):139–165, 2010.

[40] Y. Emmi, A. Fiolitakis, M. Aigner, F. Genin, and K. Syed. A new model approach for convective wall heat losses in DQMoM-IEM simulations for turbulent reactive flows. In *ASME Turbo Expo 2018*, number GT2018-76811, 2018.

[41] A. Fiolitakis. *Numerische Berechnung von Stickoxiden in turbulenten Flammen mit Transportgleichungs-PDF-Verfahren*. PhD thesis, Universität Stuttgart, 2013.

[42] J. M. Fleck. *Experimentelle Untersuchung der Selbstzündung wasserstoffreicher Brennstoffe unter Reheat-Bedingungen*. PhD thesis, Universität Stuttgart, 2015.

[43] J. M. Fleck, P. Griebel, A. Steinberg, M. Stöhr, M. Aigner, and M. Ciani. Experimental investigation of a generic, fuel flexible reheat combustor at gas turbine relevant operating conditions. In *ASME Turbo Expo 2010*, number GT2010-22722, 2010.

[44] J. M. Fleck, P. Griebel, A. M. Steinberg, C. M. Arndt, and M. Aigner. Autoignition of and subsequent flame stabilization of hydrogen / natural gas / nitrogen-jets in a vitiated air cross-flow at elevated pressure. *Int. J. Hydrogen Energy*, 38:16441–16452, 2013.

[45] J. M. Fleck, P. Griebel, A. M. Steinberg, C. M. Arndt, C. Naumann, and M. Aigner. Autoignition of hydrogen/nitrogen jets in vitiated air crossflows at different pressures. *Proc. Combust. Inst.*, 34(2):3185–3192, 2013.

[46] J. M. Fleck, P. Griebel, A. M. Steinberg, M. Stöhr, M. Aigner, and M. Ciani. Autoignition limits of hydrogen at relevant reheat combustor operating conditions. *J. Eng. Gas Turbines Power*, 134(041502), 2012.

[47] C. G. Fotache, T. G. Kreutz, D. L. Zhu, and C. K. Law. An experimental study of ignition in nonpremixed counterflowing hydrogen versus heated air. *Combust. Sci. Technol.*, 109:373–393, 1995.

[48] M. Frenklach, H. Wang, M. Goldenberg, G. Smith, D. Golden, C. Bowman, R. Hanson, W. Gardiner, and V. Lissianski. GRI-mech—an optimized detailed chemical reaction mechanism for methane combustion. Technical Report GRI-95/0058, Gas Research Institute, 1995.

[49] M. Frenklach, H. Wang, C.-L. Yu, M. Goldenberg, C. Bowman, R. Hanson, D. Davidson, E. Chang, G. Smith, D. Golden, W. Gardiner, and V. Lissianski. GRI-mech, 1995.

[50] T. F. Fric and A. Roshko. Vortical structure in the wake of a transverse jet. *J. Fluid Mech.*, 279:1–47, 1994.

[51] J. Fröhlich. *Large Eddy Simulation Turbulenter Strömungen*, volume 1. Springer, 2006.

[52] J. Fröhlich, J. Denev, and H. Bockhorn. Large eddy simulation of a jet in crossflow. *Proc. of 4th ECCOMAS Conference*, 2004.

[53] J. Fröhlich and D. von Terzi. Hybrid LES/RANS methods for the simulation of turbulent flows. *Progress in Aerospace Sciences*, 44(5):349–377, 2008.

[54] F. C. C. Galeazzo, C. Prathap, M. Kern, P. Habisreuther, and N. Zarzalis. Investigation of a flame anchored in crossflow stream of vitiated air at elevated pressures. In *ASME Turbo Expo 2012*, number GT2012-69632, 2012.

[55] N. J. Georgiadis, D. P. Rizzetta, and C. Fureby. Large-eddy simulation: Current capabilities, recommended practices, and future research. Technical Report NASA Technical Memorandum NASA/TM - 2009-215616, Glenn Research Center, Cleveland Ohio, 2009.

[56] P. Gerlinger. Investigation of an assumed PDF approach for finite-rate chemistry. *Combust. Sci. Technol.*, 175:841–872, 2003.

[57] P. Gerlinger. *Numerische Verbrennungssimulation*. Springer, 2005.

[58] P. Gerlinger, H. Möbus, and D. Brüggemann. An implicit multigrid method for turbulent combustion. *J. Comput. Phys.*, 167:247–276, 2001.

[59] F. Ghirelli and B. Leckner. Transport equation for the local residence time of a fluid. *Chemical Engineering Science*, 59(3):513–523, 2004.

[60] S. S. Girimaji. Assumed β-pdf model for turbulent mixing: Validation and extension to multiple scalar mixing. volume 78, pages 177–196, 1991.

[61] K. Gkagkas and R. P. Lindstedt. Transported PDF modelling with detailed chemistry of pre- and auto-ignition in CH4/air mixtures. *Proc. Combust. Inst.*, 31(1):1559–1566, 2007.

[62] D. G. Goodwin, H. K. Moffat, and R. L. Speth. Cantera: An object-oriented software toolkit for chemical kinetics, thermodynamics, and transport processes. Version 1.8.0, 2009.

[63] R. L. Gordon, A. R. Masri, S. B. Pope, and G. M. Goldin. A numerical study of auto-ignition in turbulent lifted flames issuing into a vitiated co-flow. *Combust. Theor. Model*, 11:351–376, 2007.

[64] R. L. Gordon, A. R. Masri, S. B. Pope, and G. M. Goldin. Transport budgets in turbulent lifted flames of methane autoigniting in a vitiated co-flow. *Combust. Flame*, 151:495–511, 2007.

[65] R. W. Grout, A. G. b, C. S. Yoo, and J. H. Chen. Direct numerical simulation of flame stabilization downstream of a transverse fuel jet in cross-flow. *Proc. Combust. Inst.*, 33:1629–1637, 2011.

[66] R. W. Grout, A. Gruber, H. Kolla, P.-T. Bremer, J. C. Bennett, A. Gyulassy, and J. H. Chen. A direct numerical simulation study of turbulence and flame structure in transverse jets analysed in jet-trajectory based coordinates. *J. Fluid Mech.*, 706:351–383, 2012.

[67] F. Güthe, J. Hellat, and P. Flohr. The reheat concept: The proven pathway to ultralow emissions and high efficiency and flexibility. *J. Eng. Gas Turbines Power*, 131, 2009.

[68] O. Heeg. *Laseroptische Untersuchung der Selbstzündungcharakteristik von mageren Zweiphasenströmungen in Gasturbinen-Vormischstrecken.* PhD thesis, Karlsruher Institut für Technologie, 2013.

[69] J. Herzler and C. Naumann. Shock-tube study of the ignition of methane/ethane/hydrogen mixtures with hydrogen contents from 0% to 100% at different pressures. *Proc. Combust. Inst.*, 32:213–220, 2009.

[70] R. Hilbert and D. Thevenin. Autoignition of turbulent non-premixed flames investigated using direct numerical simulations. *Combust. Flame*, 128:22–37, 2002.

[71] O. Hinkeldey, R. Koch, H.-J. Bauer, M. Cano-Wolff, and P. Schober. Laser based study of spray auto-ignition in a generic mixing duct. In *ASME Turbo Expo 2008*, number GT2008-50143, 2008.

[72] M. Ihme and Y. C. See. Large-eddy simulation of a turbulent lifted flame in a vitiated co-flow. 2009.

[73] M. Ihme and Y. C. See. Prediction of autoignition in a lifted methane/air flame using an unsteady flamelet/progress variable model. *Combust. Flame*, 157:1850–1862, 2010.

[74] H. G. Im, J. H. Chen, and C. K. Law. Ignition of hydrogen-air mixing layer in turbulent flows. *Symposium (International) on Combustion/The Combustion Institute*, 27:1047–1056, 1998.

[75] E. Ivanova. *Numerical Simulations of Turbulent Mixing in Complex Flows*. PhD thesis, Universität Stuttgart, 2012.

[76] E. Ivanova, M. D. Domenico, B. Noll, and M. Aigner. Unsteady simulations of flow field and scalar mixing in transverse jets. In *Volume 2: Combustion, Fuels and Emissions*. ASME, 2009.

[77] E. Ivanova, B. Noll, M. Aigner, and K. Syed. Numerical simulations of turbulent mixing and autoignition of hydrogen fuel at reheat combustor operating conditions. *J. Eng. Gas Turbines Power*, 134(041504), 2012.

[78] W. P. Jones and B. E. Launder. The prediction of laminarization with a two-equation model of turbulence. *Int. J. Heat Mass Transfer*, 15:301–314, 1972.

[79] W. P. Jones, S. Navarro-Martinez, and O. Röhl. Large eddy simulation of hydrogen auto-ignition with a probability density function method. *Proc. Combust. Inst.*, 31:1765–1771, 2007.

[80] F. Joos, P. Brunner, B. Schulte-Werning, K. Syed, and A. Ergolu. Development of the sequential combustion system for the ABB GT24/GT26 gas turbine family. In *International Gas Turbine and Aeroengine Congress and Exhibition*, number 96-GT-315, 1996.

[81] A. R. Karagozian. Transverse jets and their control. *Prog. Energ. Combust.*, 36:531–553, 2010.

[82] T. Kathrotia, U. Riedel, A. Seipel, K. Moshammer, and A. Brockhinke. Experimental and numerical study of chemiluminescent species in low-pressure flames. *Appl. Phys. B*, 107:571–584, 2012.

[83] A. Kazakov and M. Frenklach. Reduced reaction sets based on GRI-mech 1.2, 1994.

[84] R. M. Kelso, T. T. Lim, and A. E. Perry. An experimental study of round jets in cross-flow. *J. Fluid Mech.*, 306:111–144, 1996.

[85] S. G. Kerkemeier, C. N. Markides, C. E. Frouzakis, and K. Boulouchos. Direct numerical simulation of the autoignition of a hydrogen plume in a turbulent coflow of hot air. *J. Fluid Mech.*, 720:424–456, 2013.

[86] A. Kéromnès, W. K. Metcalfe, K. A. Heufer, N. Donohoe, A. K. Das, C.-J. Sung, J. Herzler, C. Naumann, P. Griebel, O. Mathieu, M. C. Krejci, E. L. Petersen, W. J. Pitz, and H. J. Curran. An experimental and detailed chemical kinetic modeling study of hydrogen and syngas mixture oxidation at elevated pressures. *Combust. Flame*, 160(6):995–1011, 2013.

[87] M. Kolb, D. Ahrens, C. Hirsch, and T. Sattelmayer. A model for predicting the lift-off height of premixed jets in vitiated cross flow. *J. Eng. Gas Turbines Power*, (GTP-15-1560), 2015.

[88] H. Kolla, R. W. Grout, A. Gruber, and J. H. Chen. Mechanisms of flame stabilization and blowout in a reacting turbulent hydrogen jet in cross-flow. *Combust. Flame*, 159(8):2755–2766, 2012.

[89] A. A. Konnov. Remaining uncertainties in the kinetic mechanism of hydrogen combustion. *Combust. Flame*, 152:507–528, 2008.

[90] H.-J. Kretzschmar and I. Kraft. *Kleine Formelsammlung Technische Thermodynamik*. Carl Hanser Verlag Muñchen, 2008.

[91] T. G. Kreutz and C. K. Law. Ignition in nonpremixed counterflowing hydrogen versus heated air: Computational study with detailed chemistry. *Combust. Flame*, 104:157–175, 1996.

[92] K. K. Kuo. *Principles of combustion*. John Wiley, 2005.

[93] A. H. Lefebvre and D. R. Ballal. *Gas Turbine Combustion: Alternative Fuels and Emissions*. CRC Press, Taylor and Francis Group, Boca Raton, 3 edition, 2003.

[94] M. Lenze and R. Carroni. Public summary report of ENCAP deliverable d2.3.3. Project report, European Commission 6th Framework Project, 2009.

[95] B. Lewis and G. von Elbe. *Combustion, Flames and Explosions of Gases.* Academic Press Inc., New York and London, 2nd edition, 1961.

[96] J. Li, Z. Zhao, A. Kazakov, and F. L. Dryer. An updated comprehensive kinetic model of hydrogen combustion. *Int. J. Chem. Kinet.*, 36:566–75, 2004.

[97] T. Lischer. *Modifikation von statistischen Turbulenzmodellen zur verbesserten Beschreibung des turbulenten Geschwindigkeits- und Mischungsfeldes bei der Querstrahleinmischung.* PhD thesis, Karlsruher Institut für Technologie, 2009.

[98] E. J. List. Turbulent jets and plumes. *Ann. Rev. Fluid Mech.*, 14:189–212, 1982.

[99] T. F. Lu, C. S. Yoo, J. H. Chen, and C. K. Law. Three-dimensional direct numerical simulation of a turbulent lifted hydrogen jet flame in heated coflow: a chemical explosive mode analysis. *J. Fluid Mech.*, 652:45–64, 2010.

[100] O. P. L. Maître, H. N. Najm, P. P. Pébay, R. G. Ghanem, and O. M. Knio. Multi-resolution-analysis scheme for uncertainty quantification in chemical systems. *SIAM Journal on Scientific Computing*, 29(2):864–889, 2007.

[101] C. N. Markides. *Autoignition in Turbulent Flows.* PhD thesis, University of Cambridge, 2005.

[102] C. N. Markides and E. Mastorakos. An experimental study of hydrogen autoignition in a turbulent co-flow of heated air. *Proc. Combust. Inst.*, 30:883–891, 2005.

[103] C. N. Markides and E. Mastorakos. Experimental investigation of the effects of turbulence and mixing on autoignition chemistry. *Flow Turbul. Combust.*, 86:585–608, 2011.

[104] A. R. Masri, R. Cao, S. B. Pope, and G. M. Goldin. PDF calculations of turbulent lifted flames of H2/N2 fuel issuing into a vitiated co-flow. *Combust. Theor. Model*, 8(1):1–22, 2004.

[105] E. Mastorakos, T. A. Baritaud, and T. J. Poinsot. Numerical simulation of autoignition in turbulent mixing flows. *Combust. Flame*, 109:198–223, 1997.

[106] E. Mastorakos, C. N. Markides, and Y. M. Wright. Hydrogen autoignition in a turbulent duct flow: experiments and modelling. In *The 12th International Conference on Fluid Flow Technologies, Budapest, Hungary*, 2003.

[107] J. McBride, S. Gordon, and M. A. Reno. Coeffcients for calculating thermodynamic and transport properties of individual species. Technical Report NASA Technical Memorandum 4513, Lewis Research Center, Cleveland Ohio, 1993.

[108] P. R. Medwell and B. B. Dally. Effect of fuel composition on jet flames in a heated and diluted oxidant stream. *Combust. Flame*, 159:3138–3145, 2012.

[109] P. R. Medwell, P. A. M. Kalt, and B. B. Dally. Imaging of diluted turbulent ethylene flames stabilized on a jet in hot coflow (JHC) burner. *Combust. Flame*, 152:100–113, 2008.

[110] W. Meier. Laser diagnostics for high-pressure gas turbine combustion. In *Workshop on Techniques for High-Pressure Combustion*, 2011.

[111] W. Meier, I. Boxx, C. Arndt, M. Gamba, and N. Clemens. Investigation of auto-ignition of a pulsed methane jet in vitiated air using high-speed imaging techniques. *J. Eng. Gas Turbines Power*, 133, 2011.

[112] L. D. A. Mendez, M. J. Tummers, and D. J. E. M. Roekaerts. Effect of hydrogen on the stabilization mechanism of natural gas jet-in-hot-coflow flames. 2013.

[113] F. Menter, M. Kuntz, and R. Langtry. Ten years of industrial experience with the SST turbulence model. In *Turbulence, Heat and Mass Transfer 4*. Bergell House, Inc., 2003.

[114] F. R. Menter. Two-equation eddy-viscosity turbulence models for engineering applications. *AIAA Journal*, 32(8):1598–1605, 1994.

[115] F. R. Menter. *Best Practice: Scale-Resolving Simulation in ANSYS CFD*, 2012.

[116] F. R. Menter and Y. Egorov. A scale-adaptive simulation model using two-equation models. In *Proceedings of the 43rd AIAA Aerospace Sciences Meeting and Exhibit*, number 1095, 2005.

[117] T. Methling. internal communication, 2016.

[118] T. Methling. *Entwicklung des linearen Transformationsmodells für die Analyse und Optimierung chemisch-kinetischer Prozesse*. PhD thesis, Universität Stuttgart, 2017.

[119] T. Methling, M. Braun-Unkhoff, and U. Riedel. A novel linear transformation model for the analysis and optimisation of chemical kinetics. *Combust. Theor. Model*, pages 1–26, 2016.

[120] D. J. Micka and J. F. Driscoll. Stratified jet flames in a heated (1390K) air cross-flow with autoignition. *Combust. Flame*, 159(3):1205–1214, 2012.

[121] Y. Minamoto, H. Kolla, R. W. Grout, A. Gruber, and J. H. Chen. Effect of fuel composition and differential diffusion on flame stabilization in reacting syngas jets in turbulent cross-flow. *Combust. Flame*, 162(10):3569–3579, 2015.

[122] S. Muppidi and K. Mahesh. Study of trajectories of jets in crossflow using direct numerical simulations. *J. Fluid Mech.*, 530:81–100, 2005.

[123] T. Myhrvold, I. S. Ertesvag, I. R. Gran, R. Cabra, and J.-Y. Chen. A numerical investigation of a lifted H2/N2 turbulent jet flame in a vitiated coflow. *Combustion Science and Technology*, 178:1001–1030, 2006.

[124] S. M. Najafizadeh, M. Sadeghi, and R. Sotudeh-Gharebagh. Analysis of autoignition of a turbulent lifted H2/N2 jet flame issuing into a vitiated coflow. *International Journal of Hydrogen Energy*, 38:2510–2522, 2013.

[125] H. N. Najm. Uncertainty quantification in fluid flow. In T. Echekki and E. Mastorakos, editors, *Turbulent Combustion Modeling*, volume 95 of *Fluid Mechanics and Its Applications*, Chapter 16. Springer, 2011.

[126] H. N. Najm, B. J. Debusschere, Y. M. Marzouk, S. Widmer, and O. P. Le Maître. Uncertainty quantification in chemical systems. *International Journal for Numerical Methods in Engineering*, 80(6-7):789–814, 2009.

[127] U. Nations. Adoption of the paris agreement. In *Framework Convention on Climate Change*. 2015.

[128] S. Navarro-Martinez and A. Kronenburg. Large eddy simulations of CH4 lifted flame using conditional moment closure. *Proc. 3rd Europ. Combust. Meeting*, 2007.

[129] S. Navarro-Martinez and A. Kronenburg. LES-CMC simulations of a lifted methane flame. *Proc. Combust. Inst.*, 32:1509–1516, 2009.

[130] S. Navarro-Martinez and A. Kronenburg. Flame stabilization mechanisms in lifted flames. *Flow Turbul. Combust*, 87:377–406, 2011.

[131] F. Nicoud and F. Ducros. Subgrid-scale stress modelling based on the square of the velocity gradient tensor. *Flow Turbul. Combust.*, 62(3):183–200, 1999.

[132] B. Noll. *Numerische Strömungsmechanik*. Springer Berlin Heidelberg, 1993.

[133] W. L. Oberkampf and C. J. Roy. *Verification and Validation in Scientific Computing*. Cambridge University Press, 2010.

[134] W. L. Oberkampf and T. G. Trucano. *Verification and Validation in Computational Fluid Dynamics*. Number SAND2002-0529 in Sandia National Laboratories. 2002.

[135] M. Ó Conaire, H. J. Curran, J. M. Simmie, W. J. Pitz, and C. K. Westbrook. A comprehensive modelling study of hydrogen oxidation. *Int. J. Chem. Kinet.*, 36(11):603–622, 2004.

[136] E. Oldenhof, M. J. Tummers, E. H. van Veen, and D. J. E. M. Roekaerts. Ignition kernel formation and lift-off behaviour of jet-in-hot-coflow flames. *Combust. Flame*, 157:1167–1178, 2010.

[137] E. Oldenhof, M. J. Tummers, E. H. van Veen, and D. J. E. M. Roekaerts. Role of entrainment in the stabilisation of jet-in-hot-coflow flames. *Combust. Flame*, 158:1553–1563, 2011.

[138] M. J. Papageorge, C. M. Arndt, F. Fuest, W. Meier, and J. A. Sutton. High-speed mixture fraction and temperature imaging of pulsed, turbulent fuel jets auto-igniting in high-temperature, vitiated co-flows. 2014.

[139] M. J. Pilling. Comprehensive chemical kinetics. In G. H. R.G. Compton, editor, *Low-Temperature Combustion and Autoignition*, volume 35. Elsevier BV, 1997.

[140] U. Piomelli. Wall-layer models for large-eddy simulations. *Progress in Aerospace Sciences*, 44(6):437–446, 2008.

[141] T. Poinsot and D. Veynante. *Theoretical and numerical combustion*. RT Edwards, Inc., 2005.

[142] S. B. Pope. *Turbulent Flows*. Cambridge University Press, 2000.

[143] M. Poyyapakkam, J. Wood, S. Mayers, A. Ciani, F. Güthe, and K. Syed. Hydrogen combustion within a gas turbine reheat combustor. In *ASME Turbo Expo 2012*, number GT2012-69165, 2012.

[144] C. Prathap, F. C. C. Galeazzo, P. Kasabov, P. Habisreuther, and N. Zarzalis. Analysis of NOx formation in an axially staged combustion system at elevated pressure conditions. In *ASME Turbo Expo 2011*, number GT2011-45239, 2011.

[145] J. Prause, C. M. Arndt, B. Noll, and M. Aigner. Large-eddy-simulation of auto-ignition in a turbulent jet in hot coflow. In *36th International Symposium on Combustion, Seoul, Korea*, number WIP Poster 4P101, 2016.

[146] J. Prause, Y. Emmi, B. Noll, and M. Aigner. LES/RANS modeling of turbulent mixing in a jet in crossflow at low momentum ratios. In *Proceedings of the 54th AIAA Aerospace Sciences Meeting*, number AIAA 2016-0609, 2016.

[147] J. Prause, E. Ivanova, B. Noll, M. Aigner, and K. Syed. Parameterstudie zur numerischen simulation der selbstzündung von wasserstoff bei gasturbinen-spezifischen bedingungen. In *VDI-Berichte, 26. Deutscher Flammentag*, number 2161, pages 423–432, 2013.

[148] J. Prause, E. Ivanova, B. Noll, M. Aigner, and K. Syed. Uncertainty evaluation of hybrid LES/RANS autoignition simulation at gas turbine operating conditions. In *ERCOFTAC Workshop on Uncertainty Quantification in Computational Fluid Dynamics*, 2013.

[149] J. Prause, B. Noll, M. Aigner, and K. Syed. Conceptual approach for uncertainty quantification in the prediction of autoignition at gas turbine operating conditions. In *ERCOFTAC Workshop on Uncertainty Quantification in Computational Fluid Dynamics*, 2014.

[150] J. Prause, B. Noll, M. Aigner, and K. Syed. Sensitivity analysis of auto-ignition simulation at gas turbine operating conditions. In *ASME Turbo Expo 2014*, number 25503, 2014.

[151] J. Prause, B. Noll, M. Aigner, and K. Syed. Sensitivity analysis of auto-ignition simulation at gas turbine operating conditions. *J. Eng. Gas Turbines Power*, 137(10)(GTP-14-1646):102601, 2015.

[152] D. B. Rusch. *Turbulence model validation for fire simulation by CFD and experimental investigation of a hot jet in crossflow.* PhD thesis, Eidgenössische Technische Hochschule ETH Zürich, 2006.

[153] R. Sadanandan, J. Fleck, W. Meier, P. Griebel, and C. Naumann. 2D mixture fraction measurements in a high pressure and high temperature combustion system using NO tracer-LIF. *Appl. Phys. B*, 106:185–196, 2012.

[154] J. U. Schlüter and T. Schönfeld. LES of jets in cross flow and its application to a gas turbine burner. *Flow Turbul. Combust.*, 2000.

[155] P. E. M. Schneider. Sekundärwirbelbildung bei Ringwirbeln und in Freistrahlen. *Z. Flugwiss. Weltraumforsch.*, 4(5):307–317, 1980.

[156] A. J. G. Schoofs and J. J. M. Rijpkema. *Chapter 4: Response Surface Approximation for Engineering Optimization.* Springer-Verlag Wien GmbH, 2001.

[157] N. N. Semenov. Thermal theory of combustion and explosion. *NACA Technical Memorandum*, (1024), 1942.

[158] M. Severin, O. Lammel, H. Ax, R. Lückerath, W. Meier, M. Aigner, and J. Heinze. High momentum jet flames at elevated pressure, b: Detailed investigation of flame stabilization with simultaneous PIV and OH-LIF. In *ASME Turbo Expo 2017*, number GT2017-64556, 2017.

[159] J. Sidey and E. Mastorakos. Visualization of MILD combustion from jets in cross-flow. *Proc. Combust. Inst.*, 35:3537–3545, 2015.

[160] S. A. Skeen, J. Manin, and L. M. Picket. Advanced diagnostics for high pressure spray combustion, 2014.

[161] T. S. Snyder, T. J. Rosfjord, J. B. McVey, and L. M. Chiappetta. Dependence of NOx on flame temperature for liquid and gaseous fuels. In *ASME Turbo Expo 1994*, number 94-GT-283. ASME International, 1994.

[162] S. Sreedhara and K. N. Lakshmisha. Autoignition in a non-premixed medium: DNS studies on the effects of three-dimensional turbulence. *Proc. Combust. Inst.*, 29:2051–2059, 2002.

[163] I. Stanković, E. Mastorakos, and B. Merci. LES-CMC simulations of different autoignition regimes of hydrogen in a hot turbulent air co-flow. *Flow Turbul. Combust.*, 90(3):583–604, 2013.

[164] A. M. Steinberg, R. Sadanandan, C. Dem, P. Kutne, and W. Meier. Structure and stabilization of hydrogen jet flames in cross-flows. *Proc. Combust. Inst.*, 34:1499–1507, 2013.

[165] R. Sullivan, B. Wilde, D. R. Noble, J. M. Seitzman, and T. C. Lieuwen. Time-averaged characteristics of a reacting fuel jet in vitiated cross-flow. *Combust. Flame*, 161:1792–1803, 2014.

[166] J. H. van't Hoff. *Studies in Chemical Dynamics*. 1884.

[167] D. Veynante and L. Vervisch. Turbulent combustion modeling. *Prog. Energ. Combust.*, 28:193–266, 2002.

[168] F. Wald, L. Kwasniewski, L. G., and M. Kurejková. Validation and verification procedures for connection design in steel structures. In *12th International Conference on Steel, Space and Composite Structures*, 2014.

[169] J. Warnatz, U. Maas, and R. W. Dibble. *Verbrennung*. Springer Science Business Media, 2001.

[170] D. C. Wilcox. *Turbulence Modeling for CFD*. DCW Industries, Inc., 1998.

[171] Y. M. Wright, O.-N. Margari, K. Boulouchos, G. de Paola, and E. Mastorakos. Experiments and simulation of n-heptane spray auto-ignition in a closed combustion chamber at diesel engine conditions. *Flow Turbul. Combust.*, 84:49–78, 2019.

[172] Z. Wu, A. R. Masri, and R. W. Bilger. An experimental investigation of the turbulence structure of a lifted H2/N2 jet flame in a vitiated co-flow. *Flow Turbul. Combust.*, 76:61–81, 2006.

[173] J. Wünning and J. Wünning. Flameless oxidation to reduce thermal no-formation. *Prog. Energ. Combust.*, 23:81–94, 1997.

[174] R. A. Yetter, F. L. Dryer, and D. M. Golden. *Pressure Effects on the Kinetics of High Speed Chemically Reacting Flows*, pages 309–338. Springer New York, 1992.

[175] C. S. Yoo, E. S. Richardson, R. Sankaran, and J. H. Chen. A DNS study on the stabilization mechanism of a turbulent lifted ethylene jet flame in highly-heated coflow. *Proc. Combust. Inst.*, 33:1619–1627, 2011.

[176] C. S. Yoo, R. Sankaran, and J. H. Chen. Three-dimensional direct numerical simulation of a turbulent lifted hydrogen jet flame in heated coflow: flame stabilization and structure. *J. Fluid Mech.*, 640:453–481, 2009.

[177] L. L. Yuan, R. L. Street, and J. H. Ferziger. Large-eddy simulations of a round jet in crossflow. *J. Fluid Mech.*, 379:71–104, 1999.

[178] A. J. Yule. Large-scale structure in the mixing layer of a round jet. *J. Fluid Mech.*, 89(03):413, 1978.